UNIVERSITY OF OKLAHOMA

GRADUATE COLLEGE

MEASUREMENT OF THE INCLUSIVE ISOLATED PROMPT PHOTON PRODUCTION AT $\sqrt{s} = 7$ TeV WITH THE ATLAS DETECTOR FOR THE 2011 DATASET

A DISSERTATION

SUBMITTED TO THE GRADUATE FACULTY

in partial fulfillment of the requirements for the

Degree of

DOCTOR OF PHILOSOPHY

By

SCARLET NORBERG
Norman, Oklahoma
2014

MEASUREMENT OF THE
INCLUSIVE ISOLATED PROMPT PHOTON PRODUCTION
AT $\sqrt{s} = 7$ TeV WITH THE ATLAS DETECTOR
FOR THE 2011 DATASET

A DISSERTATION APPROVED FOR THE
HOMER L. DODGE DEPARTMENT OF PHYSICS AND ASTRONOMY

BY

Dr. Braden Abbott, Chair

Dr. Phillip Gutierrez

Dr. Howard Baer

Dr. Sheena Murphy

Dr. JoAnn Palmeri

Acknowledgments

In the course of my study there are many people I would like to thank and it would be impossible to thank everyone here, I would like to thank a few people.

I would like to first and for most thank my family, especially my mom. Without her support and encouragement I know that I would not have taken this long journey.

I am also very grateful that I had the opportunity to experience a fellowship at Argonne. The group there is amazingly supportive and knowledgeable. I would specifically like to thank Sergei Chekanov who helped me with both this photon study and the authorship project that I worked on. I would also like to thank Jimmy Proudfoot for teaching me about how the tile calorimeter was built and helping with my authorship project.

I would also like to thank the members of the standard model analysis group at CERN who helped to make sure that my analysis was correct.

To all my friends that I have met over my years as a graduate student thank you for letting me blow off steam. Also specifically to the high energy experimental group thank you for fostering an open environment where help was welcome and useful. Specifically I would like to thank Amanda Kruse for helping me when I had coding questions.

I have been fortunate enough to work for a great department at the University of Oklahoma. I would to thank all of the professors for helping to encourage and further my physics knowledge. I would like to thank Chris Walker for helping with coding questions. I would like to thank Brad Abbott for forcing me to think of the WHY? I was doing what I was doing. I would also like to thank Brad for helping me to take what I want to say and put it in a coherent form on paper.

Table of Contents

Acknowledgments **iv**

Abstract **xiii**

1 Introduction **1**

2 Theoretical Motivation **4**
2.1 The Standard Model 4
2.1.1 Fermions 4
2.1.2 Bosons 5
2.1.3 Group Theory 6
2.2 Direct Photon Production in Hadron Collisions 7
2.3 Higher Order Corrections 8
2.4 Parton Model 11

3 The LHC and ATLAS Detector **14**
3.1 Large Hadron Collider 14
3.2 A Toridal LHC AppartuS 17
3.3 Inner Detector 19
3.3.1 Pixel Silicon Detector 20
3.3.2 Silicon Micro-strip Detector 20
3.3.3 Transition Radiation Tracker 20
3.4 Calorimeter 21
3.4.1 Electromagnetic Calorimeter 21
3.4.2 Hadronic Calorimeter 29
3.4.3 Muon Detector 29
3.5 Data Samples 29
3.5.1 Collision Data 30
3.5.2 Trigger System and Requirements 30
3.5.3 Level-1 and Level-2 30
3.5.4 High-Level Triggers 31

4 Simulated events **33**
4.1 Leading Order Monte Carlo 34
4.2 JETPHOX 37

5 Photon Reconstruction **40**
5.1 Reconstruction Algorithms 40
5.1.1 Sliding window algorithm 41
5.1.2 Topological Clusters 42
5.2 Converted Photons 43
5.3 Photon identification 44
5.4 Photon preselection 48
5.5 Photon isolation energy 49

6 Background Estimation and Signal Extraction **55**
6.1 Background Estimation 55
6.2 Signal Extraction 60
6.3 Previous Results 68

7 Efficiency and Systematic Uncertainty **70**
7.1 Introduction 70
7.2 Efficiency 70
7.3 Cross Section 74
7.4 Systematic Uncertainties 76
7.5 `JETPHOX` Uncertainties 84

8 Results of the Measurement of the Isolated Cross Section and Comparison with Predictions **90**
8.0.1 Pileup Comparison 94
8.1 Conclusion 98

REFERENCES **102**

List of Tables

2.1 SM leptons, where $|e|$ is defined as $1.60217657 \times 10^{-19}$ Coulombs. 4
2.2 SM quarks, where $|e|$ is defined as $1.60217657 \times 10^{-19}$ coulombs. 5
2.3 SM Force carriers. 6

4.1 Monte Carlo datasets used in the inclusive photon analysis. All samples contain all relevant signal processes, unless otherwise indicated. The QCD samples contain both prompt photon production events and the most significant sources of background as summarized in Table **4.2**. . . 35
4.2 Elementary QCD processes that are enabled in the QCD `PYTHIA` samples ($q = u, d, s, c, b$, $Q = t$). 37

5.1 A list of the variables that separate "tight" and "loose" selections. Where E is defined as the energy, $max1$ is defined as the maximum value, $max2$ is defined as the next maximum value, min is defined as the minimum, $S1$ is the first strip layer, $S2$ is the second layer of the ECAL, the subscript $x \times x$ is the window size that is used. 47

7.1 Relative systematic uncertainty on the E_T^γ differential cross section for photons in the barrel. Each column shows a systematic check, while each row shows the bin index. The luminosity uncertainty (1.8%) is not listed in the table, but included into the final cross sections. 82
7.2 Relative systematic uncertainty on the E_T^γ differential cross section for photons in the endcap. Each column shows a systematic check, while each row shows the bin index. 83
7.3 Relative systematic uncertainty on the $|\eta^\gamma|$ differential cross section. Each column shows a systematic check, while each row shows the bin index. 83

8.1 Measured inclusive prompt photon production cross section in the pseudorapidity range $|\eta^\gamma| < 1.37$ as a function of E_{T}^γ with statistical and systematic uncertainties. The bin ranges are defined as $[xmin, xmax)$. 95
8.2 Measured inclusive prompt photon production cross section in the pseudorapidity range $1.52 \leq |\eta^\gamma| < 2.37$ as a function of E_{T}^γ with statistical and systematic uncertainties. The bin ranges are defined as $[xmin, xmax)$. 98
8.3 Measured inclusive prompt photon production cross section for $E_{\mathrm{T}}^\gamma > 100$ GeV as a function of $|\eta^\gamma|$ with statistical and systematic uncertainties. The bin ranges are defined as $[xmin, xmax)$. 99
8.4 The NLO CT10 inclusive prompt photon production cross section in the pseudorapidity range $|\eta^\gamma| < 1.37$ as a function of E_{T}^γ with statistical and systematic uncertainties. Small differences in the upper and lower uncertainties were symmeterized. The bin ranges are defined as $[xmin, xmax)$. 100
8.5 The NLO CT10 inclusive prompt photon production cross section in the pseudorapidity range $1.52 \leq |\eta^\gamma| < 2.37$ as a function of E_{T}^γ with statistical and systematic uncertainties. Small differences in the upper and lower uncertainties were symmetrized. 101

8.6 The NLO CT10 inclusive prompt photon production cross section for $E_{\mathrm{T}}^{\gamma} > 100$ GeV as a function of $|\eta^{\gamma}|$ with statistical and systematic uncertainties. Small differences in the upper and lower uncertainties were symmetrized. 101

List of Figures

1.1 The region of PDF probed by past experiments compared to the region the LHC will probe. Overlaid on this plot is the region probed in this thesis (higher blue shape). As well as what was probed by both the previous CMS and ATLAS measurements (lower black shape)[1]. 2

2.1 Direct photon LO diagrams at hadron colliders. The Compton diagram is the most dominate process at the LHC at high E_T^{γ}. 10
2.2 NLO diagrams for prompt photons at hadron colliders. The direct diagram comes primarily from corrections to the LO diagrams. Diagram (A) is for a real gluon emission, diagram (b) is for a virtual gluon emission. 10
2.3 The momentum distribution of partons within a proton is called a Parton Density Functions (PDFs). This PDF shows the partons within a proton with a momentum transfer (Q^2) of $(10\text{GeV})^2$ at different fractional momentum x and PDF functions f. CTEQ6L refers to the Coordinated Theoretical-Experimental project on QCD, with 6 being the version and L referring to LO diagrams. 12

3.1 The LHC ring with locations for the detectors positioned around the ring. 16
3.2 The ATLAS detector and the coordinate system chosen by ATLAS. . . 18
3.3 Schematic of the inner detectors. The red line indicates the trajectory of a charged particle passing through the inner detectors. 19
3.4 The calorimeter portion of ATLAS. 22
3.5 The ECAL portion of the detector. 24
3.6 Schematic of the ECAL including a description of a cell. 27
3.7 An example of a detector pulse, as well as the shaped and sampled signal. This shaped signal is shaped by the front end boards (FEB). 28
3.8 Efficiencies of g60_loose and g80_loose triggers with respect to offline tight photons. Uncertainties are statistical only.[2] 32

4.1 The number of primary vertices (nPV) for events with at least one (loose or tight) photon with $E_T^{\gamma} > 100$ GeV compared to the Monte Carlo simulations. 38
4.2 Fig. shows a comparison of a variable used in the selection process for both data and MC [3]. 38
4.3 The invariant mass of $Z \rightarrow e^- e^+$ for both data (after full calibration) and MC. (a) Events with both electrons in $|\eta| < 1.37$ (b) Events with at least an electron in $1.52 < |\eta| < 1.37$ [4]. 39

5.1 The signal and background for the inclusive photon analysis using 2010 ATLAS data. The same cuts were used for both the 2010 and 2011 analysis for the variables listed in this section. 45

5.2 Fig.(a) shows a clean signature for a photon candidate where in the strips there is one maximum in the strips and a narrow shower width in the second layer and is considered "tight". Fig.(b) is the signature for a π^0 where there are two maximum in the strip layer and a broader shape in layer two of the ECAL and is considered "loose" or "non-tight". 46
5.3 The isolation energy in the calorimeter. All of the calorimeter energy is summed in an annulus around the photon, where the central core is removed. This summed energy is defined as the isolation energy. 52
5.4 The distributions for the calorimetric isolation variable $E_{\mathrm{T}}^{(R<0.4)}$ in the central η region, after the leakage and density corrections, for tight (solid dots) and loose (shaded gray region) candidates. The latter is normalized to the former for $E_{\mathrm{T}}^{(R<0.4)} > 15$ GeV ("non-isolated region"). The excess of tight candidates over the normalized non-tight candidates for $E_{\mathrm{T}}^{(R<0.4)} < 15$ GeV ("isolated region") shows a clear peak for signal prompt photons. 53
5.5 The distributions for the topocluster isolation variable $E_{\mathrm{T}}^{(R<0.4)}$ versus the standard (cluster) isolation, after the leakage and density corrections, for tight and non-tight candidates. The latter is normalized to the former for $E_{\mathrm{T}}^{(R<0.4)} > 15$ GeV ("non-isolated region"). The red color is used to show the topocluster isolation, while black shows the standard (cluster) isolation. Despite the differences seen the amount of data under the curves is similar. 54

6.1 ϕ distributions for photon candidates before efficiency corrections for both the barrel (a) and endcap (b) regions. The uncorrected data are compared to the signal MC in the signal region. 56
6.2 ϕ distribution for $500 < E_T^{\gamma} < 600$ GeV for photon candidates before data corrections. The uncorrected data are compared to the signal MC in the signal region. 57
6.3 (a) The efficiency and (b) the purity as a function of the photon p_T for all of the isolation energies studied. 59
6.4 The prompt photon ("signal") purity as a function of E_{T}^{γ} and $|\eta(\gamma)|$ determined from the data using the the two-dimensional sidebands method (which also includes a correction from the MC). The uncertainties on the $|\eta(\gamma)|$ plot (b) are too small to be seen because of the large statistics. . 61
6.5 An illustration of the 2D-sideband method. The isolation is defined on the horizontal axis. The "tightness" is defined on the vertical axis. Where the signal region is in region A and is the isolated tight region. 62
6.6 The distributions for the calorimetric isolation variable $E_{\mathrm{T}}^{(R<0.4)}$, for tight (solid dots) and non-tight (shaded region) candidates. The latter is normalized to the former for $E_{\mathrm{T}}^{(R<0.4)} > 15$ GeV ("non-isolated region"). The vertical line indicates the final selection cut (7 GeV) used for the final cross sections. The excess of tight candidates over the normalized non-tight candidates for $E_{\mathrm{T}}^{(R<0.4)} < 7$ GeV ("isolated region") proves the evidence of a signal. 63

6.7 $E_{\mathrm{T}}^{(R<0.4)}$ distributions of tight photons in the forward region, after subtracting the normalized non-tight distribution, for two different E_{T}^{γ} bins. 64
6.8 E_{T}^{γ} event distributions for signal MC and background MC before the detector corrections are applied. Figure (a) is for the signal like region, region A. Figure (b) is for the background region, region D. 64
6.9 E_{T}^{γ} event distributions for data before the detector correction applied. The uncorrected data are compared to the signal MC in the region A for (a), (b) compares the same data as (a) but the MC combines signal+background MC. 65
6.10 The comparisons of the signal purities using several subtraction methods as a function of p_T: the uncorrelated method divided by the correlated method, and the modified correlated method divided by the correlated method. The purities where calculated using data and the sideband subtraction method. 67
6.11 The signal purity for the barrel and endcap η^{γ} regions estimated from the data using the two-dimensional side band approach shown in Eq. (**6.3**). The shaded bands indicate statistical uncertainty. 67

7.1 The efficiency from the PYTHIA MC signal sample and the HERWIG MC signal sample for different $\eta(\gamma)$ regions (left: barrel; right: end-cap). 73
7.2 The correction factors as a function of E_T^{γ} used in this analysis. The shaded bands indicate the systematic uncertainties discussed in Sect. 7.4. 74
7.3 The correction factors for $E_{\mathrm{T}}^{\gamma} > 100$ GeV as a function of $|\eta^{\gamma}|$. The shaded area shows the statistical and systematic uncertainties. The low-efficiency region $1.37 < |\eta^{\gamma}| < 1.52$ is excluded from the measurement. . 75
7.4 Resolution for $E_T^{\gamma} > 100$ GeV (a) and 500 GeV (b) 75
7.5 Bin-by-bin correction factors in $|\eta(\gamma)| < 1.37$, together with systematic uncertainties. Figure (a) is the correction factor as a function of E_T^{γ} for $|\eta(\gamma)| < 1.37$. Figure (b) is a function of $\eta(\gamma)$ for $|\eta(\gamma)| < 1.37$ for an $E_T^{\gamma} > 100$ GeV. 79
7.6 Bin-by-bin correction factors in the endcap ($1.52 < |\eta(\gamma)| < 2.37$) together with systematic uncertainties. Figure (a) is the correction factor as a function of E_T^{γ} for $1.52 < |\eta(\gamma)| < 2.37$. Figure (b) is a function of $\eta(\gamma)$ for $1.52 < |\eta(\gamma)| < 2.37$ for an $E_T^{\gamma} > 100$ GeV. 80
7.7 Bin-by-bin correction factors for as a function of $|\eta(\gamma)|$ $E_T^{\gamma} > 600$ GeV. The statistical uncertainties in the endcap are too large to reliably calculate the correction factors. 80
7.8 A ratio of E_T^{γ} for various configurations of the isolation with partons and hadrons. This shows that the effect of hadronization is on the order of a few percent at low E_T^{γ}. 85
7.9 E_T^{γ} at the parton level with (PartonIso40_UE) and without (PartonIso40) pileup and the UE included, divided by the standard isolation at the particle level used for the efficiency calculations. Where the left plot is `PYTHIA MC11` and the right plot is `HERWIG` DP. The contribution from UE is on the order of less than 2%. 86

7.10 The ratio of the E_T^γ using different UE tunes to PYTHIA8. The difference is small, on the order of a few percent. 87

8.1 Measured vs expected inclusive prompt photon production cross section, for photons with transverse energies above 100 GeV and in the pseudo-rapidity range $|\eta(\gamma)| < 1.37$ (a) and $1.52 \leq |\eta(\gamma)| < 2.37$ (b). The inner error bars show statistical uncertainties, while the full error bars show statistical and systematic uncertainties added in quadrature. The CT10 and MSTW2008NL PDFs are used in the theoretical computation. The experimental values are placed at the center of each bin. The width of the horizontal bars indicates the size of the bin. 92

8.2 Measured vs predicted inclusive prompt photon production cross section as a function of $|\eta(\gamma)|$ for photons with transverse energies above 100 GeV. The inner error bars show statistical uncertainties, while the full error bars show statistical and systematic uncertainties added in quadrature. For this cross section, statistical uncertainties are negligible. The CT10 and MSTW2008NL PDFs are used in the theoretical computation. The experimental values are placed at the center of each energy bin. The width of the horizontal bars indicates the size of the bin. 93

8.3 Same data and NLO as in Fig. **8.1** and **8.2**, but the MC generators were used for direct photons from the hard process. 93

8.4 Same LO MC as in Fig. **8.1** and **8.2** compared with the MC generators that were used for direct photons from the hard process seen in Fig. **8.3**. 94

8.5 $E_{\mathrm{T}}^{(R<0.4)}$ distributions of tight photons after subtracting the normalized non-tight distribution for low-pileup runs before the run 184328. 96

8.6 Measured vs expected inclusive prompt photon production cross section, for photons with transverse energies above 100 GeV and in the pseudo-rapidity range $|\eta(\gamma)| < 1.37$ (a) and $1.52 \leq |\eta(\gamma)| < 2.37$ (b) for low pileup runs before the run 184328. The inner error bars show statistical uncertainties, while the full error bars show statistical and systematic uncertainties added in quadrature. The CT10 and MSTW2008NL PDFs are used in the theoretical computation. The experimental values are placed at the center of each bin. The width of the horizontal bars indicates the size of the bin. 96

8.7 Measured vs predicted inclusive prompt photon production cross section as a function of $|\eta(\gamma)|$ for photons with transverse energies above 100 GeV for low pileup runs before the run 184328. The inner error bars show statistical uncertainties, while the full error bars show statistical and systematic uncertainties added in quadrature. For this cross section, statistical uncertainties are negligible. The CT10 and MSTW2008NL PDFs are used in the theoretical computation. The experimental values are placed at the center of each energy bin. The width of the horizontal bars indicates the size of the bin. 97

8 105

Abstract

A measurement of the cross section for the inclusive production of isolated prompt photons in pp collisions at a center-of-mass energy $\sqrt{s} = 7$ TeV is presented. The measurement covers the pseudorapidity ranges $|\eta^{\gamma}| < 1.37$ and $1.52 \leq |\eta^{\gamma}| < 2.37$, in the transverse energy range $100 \leq E_{\mathrm{T}}^{\gamma} < 1000$ GeV. The results are based on an integrated luminosity of 4.6 fb^{-1} collected with the ATLAS detector at the LHC. The results are compared with next-to-leading order perturbative QCD calculations with CT10 and MSTW2008NLO PDFs, as well as two leading order Monte Carlo `PYTHIA` and `HERWIG`.

Chapter 1

Introduction

This dissertation describes the extraction of isolated prompt photons with transverse energies above 100 GeV using 4.6 fb^{-1} of data collected by ATLAS between March and October 2011. The isolated prompt-photon production cross section in pp collisions at $\sqrt{s} = 7$ TeV is measured in two pseudorapidity ranges $|\eta(\gamma)| < 1.37$, and $1.52 \leq |\eta(\gamma)| < 2.37$.

All photons produced in proton-proton collisions not coming from hadron decays are considered as "prompt". They include both "direct" photons, which take part in the hard subprocess (the photons originating from all the Feynman diagrams with a photon emission), and "fragmentation" photons, which are the result of the fragmentation of a colored high p_{T} parton [5, 6]. Photons are considered isolated, from a theoretical perspective, if the amount of hadronic isolated transverse energy ($E_{\mathrm{T}}^{\mathrm{iso}}$) carried by all the colored partons within an annulus, centered around the photon direction in the pseudorapidity (η) and azimuthal angle (ϕ) plane, is smaller than some chosen value:

$$\text{for} \quad (\eta - \eta^{\gamma})^2 + (\phi - \phi^{\gamma})^2 \leq R^2, \qquad E_{\mathrm{T}}^{\mathrm{iso}} \leq E_{\mathrm{T}}^{\mathrm{cut}}. \tag{1.1}$$

The isolation criterion used in this dissertation to define isolated photons is $E_{\mathrm{T}}^{\mathrm{iso}} <$ 7 GeV in a annulus of radius $R = 0.4$.

This is the first inclusive direct photon analysis that extends the cross section in E_T out to 1 TeV. Also a comparison between two leading order (LO) Monte Carlos (MCs) and a next to leading order (NLO) calculation is presented. Extending the cross section to 1 TeV reveals that this analysis could be used to constrain parton

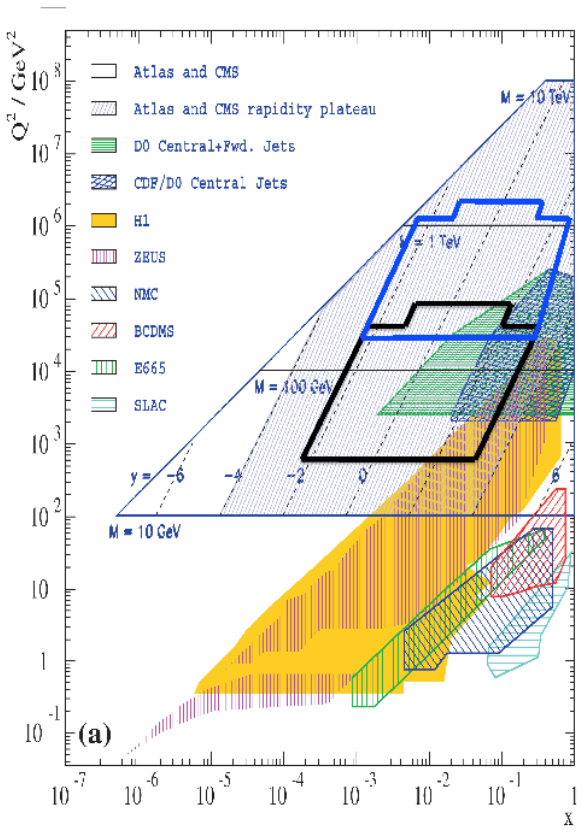

Figure 1.1: The region of PDF probed by past experiments compared to the region the LHC will probe. Overlaid on this plot is the region probed in this thesis (higher blue shape). As well as what was probed by both the previous CMS and ATLAS measurements (lower black shape)[1].

distribution functions (PDFs). For example Fig. **1.1** shows the reach for the PDFs probed for this dissertation compared to the previous and potential future results. The differential cross sections (σ) $\frac{d\sigma}{dE_T^\gamma}$ and $\frac{d\sigma}{d\eta^\gamma}$ are both presented in this dissertation.

This dissertation is organized into eight chapters, starting with Chapter 2 which is a brief discussion on the theory behind this analysis. Chapter 3 has a brief description of the LHC and ATLAS with a focus on the relevant detector regions. Chapter 4 summarizes the data and simulated samples used for this

analysis. Chapter 5 describes how the photons are reconstructed and the selection criteria applied to the initial data sample collected with the inclusive photon trigger. The *in situ* measurement of the background contamination in the selected photon sample is described in Chapter 6. The estimation of the overall photon reconstruction efficiency is presented in Chapter 7, along with the extraction of the prompt-photon production cross section from the observed signal transverse-energy distribution, estimation of the photon efficiency and the calculation of the detector unfolding. Also in Chapter 7, the corresponding systematic uncertainties on the cross section measurement are summarized, as well as a brief description of the evaluation of the theoretical predictions. The comparison between the LO MC and the NLO calculations to the experimental cross sections is given in Chapter 8.

Chapter 2

Theoretical Motivation

2.1 The Standard Model

The standard model (SM) is a well developed theory that describes the constituents of matter and anti matter and how they interact. In the SM there are two different classifications of particles: fermions and bosons.

2.1.1 Fermions

Fermions are half integer spin particles that include leptons as well as quarks. Leptons come in three generations and have integer charge. They are the electron, electron neutrino, muon, muon neutrino, tau, and tau neutrino and are listed in Table **2.1**. In addition there are also anti leptons. These particles have the same mass and spin as their matter counterparts but have the opposite charge. For example, the electron's corresponding anti particle is the positron, which has a positive charge instead of a negative charge.

generation name	symbol	spin	charge[$\|e\|$]	mass[MeV]
first electron neutrino	ν_e	1/2	0	$< 2 \times 10^{-6}$
first electron	e	1/2	-1	0.511
second muon neutrino	ν_μ	1/2	0	< 0.17
second muon	μ	1/2	-1	105.66
third tau neutrino	ν_τ	1/2	0	< 15.5
third tau	τ	1/2	-1	1776.82

Table 2.1: SM leptons, where $|e|$ is defined as $1.60217657 \times 10^{-19}$ Coulombs.

There are six flavors of quarks that are arranged in three generations: up, down, strange, charmed, top and bottom, see Table **2.2**. In addition to spin and charge, quarks have an additional quantum number called color. There are also

anti quarks which have the opposite charge and carry anti color. All quarks come in three different colors called red, blue, and green. All known hadrons are formed in colorless combinations. All known composite particles that consist of quarks are classified as either a baryon or a meson. Baryons contain three quarks each of a different color or three anti quarks each with a different anti color. Combining all three colors together or all three anti colors result in a colorless combination. The mesons contain a quark and an anti quark, where color and anti color combine to form a colorless combination. Both baryons and mesons are classified as hadrons.

generation	name	symbol	spin	charge[$\|e\|$]	mass[GeV]
first	up	u	1/2	$\frac{2}{3}$	2.3×10^{-3}
first	down	d	1/2	$-\frac{1}{3}$	4.8×10^{-3}
second	charm	c	1/2	$\frac{2}{3}$	1.275
second	strange	s	1/2	$-\frac{1}{3}$	95×10^{-3}
third	top	t	1/2	$\frac{2}{3}$	173.5
third	bottom	b	1/2	$-\frac{1}{3}$	4.18

Table 2.2: SM quarks, where $|e|$ is defined as $1.60217657 \times 10^{-19}$ coulombs.

2.1.2 Bosons

In the SM, particles interact via integer spin bosonic force carriers listed in Table **2.3**. There are three forces in the SM: the weak force, the strong force, and the electromagnetic force. The $W^{\pm}$ and Z boson are the force carriers for the weak force. The gluon is the force carrier for the strong force. The photon is the force carrier for the electromagnetic force. Gravity is a small force and is not included in the SM. The force carrier for gravity is the graviton and has yet to be discovered.

name	symbol	spin	charge[$\|e\|$]	mass[GeV]
photon	γ	1	0	0
W-boson	$W^{\pm}$	1	± 1	80.4
Z-boson	Z	1	0	91.2
gluons	g_a	1	0	0

Table 2.3: SM Force carriers.

2.1.3 Group Theory

The electromagnetic force is based upon a local $U(1)_{QED}$ gauge group theory to describe the interactions that occur. The weak force is described by the local $SU(2)_L$ gauge group. At high energies QED and the weak force unify and become the electroweak theory. The electroweak theory is based upon the $(SU(2)_L \times U(1)_Y)$ gauge group, where the subscript Y is defined as weak hyper charge, and the subscript L describes weak isospin. The strong force is described by the $SU(3)_C$ gauge group theory. The SM is described by the $SU(2)_L \times U(1)_Y \times SU(3)_C$ gauge theory. Which will break down to $U(1)_Y \times SU(3)_C$ via the Higgs mechanism. The Higgs mechanism deals with the Higgs field interacting with matter giving the quarks, charged leptons and the W and Z bosons mass. The Higgs particle is the manifestation of vibrations in the field and was observed at the LHC.

High energy particle physicists attempt to understand the fundamental building blocks and forces of nature. Experimentalists often accelerate particles, such as protons, to high energies to probe the SM and beyond the SM. When these high energy particles collide, they can cause the production of heavier particles as well as additional particles to be produced. Detectors are placed around these collisions to measure the properties of these produced particles. By studying these collisions, physicists hope to better understand nature, and to search for deviations from the SM predictions. In this analysis which is searching for direct photons, the relevant theories that are involved are QED and QCD.

2.2 Direct Photon Production in Hadron Collisions

QED describes the interaction of charged particles with an electromagnetic field whose quanta are photons. The strength of this interaction is defined as α, and is sometimes called the fine structure constant. It is proportional to charge squared and is approximately 1/137. The fine structure constant α is defined as:

$$\alpha = \frac{e^2}{4\pi}, \tag{2.1}$$

where e as the electromagnetic coupling and is given in units of energy. Electrons interact via the electromagnetic force where the photon is the force carrier. The electron carries charge but the photon does not. Therefore photons can not couple to other photons. The force of this interaction is proportional to one over the distance squared.

The Lagrangian that describes the QED process is:

$$\mathcal{L} = \bar{\psi}(i\gamma^\mu \partial_\mu - m)\psi + e\bar{\psi}\gamma^\mu A_\mu \psi - \frac{1}{4}F_{\mu\nu}F^{\mu\nu} \tag{2.2}$$

where ψ represents the fermion field, γ^μ are the Dirac matrices, m is the mass of the fermion, e is the fermions electric charge, A_μ represents the photon field, $F_{\mu\nu}$ equals $\partial_\mu A_\nu - \partial_\nu A_\mu$.

QCD is the mathematical description of how quarks and gluons interact via the strong nuclear force. Quarks and gluons both interact via the strong force and both particles contain color. Gluons can couple to themselves as well as to quarks. This leads to an effect called asymptotic freedom. Asymptotic freedom describes the effect where the interaction strength decreases as energy increases. When

hadrons collide, because of asymptotic freedom in QCD the dominant effect is described by, only one component, or parton of each hadron will typically collide.

At larger distance scales, single partons are not observed and this is due to confinement. Confinement describes the effect where quarks and gluons are always seen as bound in colorless hadrons. The strength of this interaction is related to α_s. Where α_s is defined as:

$$\alpha_s = \frac{g_s^2}{4\pi}, \tag{2.3}$$

where g_s is the strong coupling.

The QCD Lagrangian is given as:

$$\mathcal{L} = \bar{q}(i\gamma^\mu \partial_\mu - m)q + g_s(\bar{q}\gamma^\mu T^a q)G_\mu^a - \frac{1}{4}G_{\mu\nu}^a G^{\mu\nu a} \tag{2.4}$$

where m is the quark mass, g is the strong coupling constant, and T_a represents the generators of the $SU(3)_c$ group. G_μ^a is defined as the strong gauge field or gluon fields (where there are eight $a = 1 - 8$), where in the Lagrangian it is related as $G_{\mu\nu}^a = \partial_\mu G_\nu^a - \partial_\nu G_\mu^a - g f^{abc} G_\mu^b G_\nu^c$. Here, f_{abc} labels the group structure constants for the $SU(3)_c$ group.

Theorists use Feynman diagrams as pictorial representations of the mathematical interactions of the forces. The cross section can be calculated by using the Feynman rules of the Feynman diagrams. There are different orders that come from these calculations an example of leading order Feynman diagrams and next to leading order Feynman diagrams in Fig. **2.1**.

2.3 Higher Order Corrections

To predict physics with higher precision, we need to consider both leading order and higher order effects. When QCD calculations are performed divergences

(ultraviolet, infrared and collinear) can arise from these higher order effects and need to be canceled out. Ultraviolet divergences come from very short distances and very high energies. Some divergences cancel one with another while others are absorbed into Lagrangian parameters (renormalization). Infrared singularities come from gluon radiation with energy approaching zero. For the infrared divergences, a Feynman diagram that has a virtual particle can be combined with a real emission. The divergences cancel so that the calculation is infrared safe. Collinear divergences arise when a gluon is emitted in the same direction as one of the initial quarks. When infinities arise from the collinear divergences, the PDF needs to be modified. When renormalization is performed a renormalization scale, μ_R, is introduced. At this energy scale, the remaining UV divergences can be absorbed in to known quantities. Since μ_R is nonphysical, rescaling should not depend on the choice of μ_R. The μ_R scale is usually set to the momentum transfer Q^2.

Since QCD is difficult to calculate, a perturbation series expansion is applied and called perturbative QCD (PQCD). Theoretically the cross section is expanded in orders of the coupling constant α_s. Now that the infinities are renormalized at μ_R, the PDFs can be included but, in order to do this, the hard scattering needs to be separated into the PQCD part and the non PQCD part. Essentially the small distance scales (PQCD) need to be separated from the large distance scales (non PQCD). This can be done through the introduction of the factorization scale, μ_F. The factorization scale is a scale that is also typically set to the momentum transfer Q^2.

The results of PQCD calculations should not depend on the choice of the μ_R and μ_F scales. Any variation in the results of PQCD when changing the renormalization and factorization scales is an uncertainty in the theoretical calculations.

At LO, the varying of these scales typically gives large variations in the theoretical calculations. At NLO, the variations due to changing the scales is reduced and provides a much smaller theoretical uncertainty.

Confinement begins to take place when the partons get further away from each other. This process leads to fragmentation. Fragmentation (or hadronization) occurs when the quarks and gluons start to form colorless hadrons. The probability that a parton will fragment into a particular hadron with a portion of the momentum is called a fragmentation function. The reason that fragmentation functions are important is because they incorporate the non-PQCD effects. The fragmentation functions are fitted from experimental data, are universal and do not depend on the hard scatter.

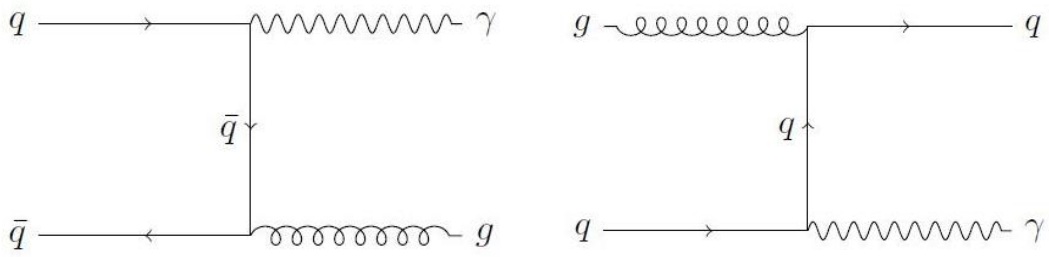

(a) Annihilation (b) Compton scattering

Figure 2.1: Direct photon LO diagrams at hadron colliders. The Compton diagram is the most dominate process at the LHC at high E_T^{γ}.

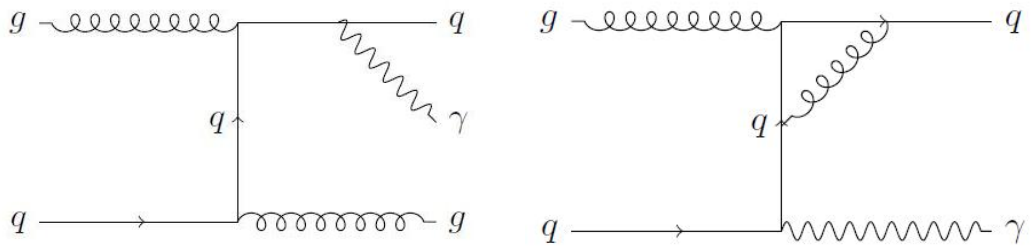

(a) Fragmentation (b) NLO direct

Figure 2.2: NLO diagrams for prompt photons at hadron colliders. The direct diagram comes primarily from corrections to the LO diagrams. Diagram (A) is for a real gluon emission, diagram (b) is for a virtual gluon emission.

2.4 Parton Model

In this analysis prompt photons are of interest. Prompt photons come from two sources in the collision; they can come directly from hard scattering or from fragmenting partons. Prompt photon production at hadron colliders provides a handle for testing PQCD predictions [7]. This is done by calculating the photon cross section (σ). The cross section is measured in units of area, and describes how probable a given interaction will occur.

The first nonzero contribution to the series expansion (expanding in powers of α_s) discussed earlier is called the leading order term (LO). The next-to-leading order (NLO) term is the next term in the expansion. Higher order terms can be neglected, making PQCD easier to calculate. Figures **2.1** and **2.2** are the LO and NLO diagrams for prompt photon production at hadron colliders. One complication in calculating PQCD is that the momentum of the colliding partons must be known. The energy of the colliding hadron is known but the energy of constituent partons is not. In PQCD, parton distributions functions (PDFs) must be implemented. PDFs describes the momentum distribution of the partons within the proton. The PDFs are not universal since they depend on the momentum transfer Q^2. An example of one PDF is shown in Figure **2.3**.

The hadronic cross section is calculated for $A + B \rightarrow C + X$ as:

$$\sigma_{a_i b_i} = \int f_{a_i/A}(x_{a_i}, a^2) f_{b_i/B}(x_{b_i}, a^2) dx_a dx_b dz_c D_{c_k}(z_c, \mu_f^2) \sigma_{a_i b_j \rightarrow c_k + X}(\mu_F^2, \mu_R^2) \tag{2.5}$$

where A is a hadron that is composed of a_i partons, B is a hadron composed of b_j partons. C is a hadron and contains c_k partons and D_{c_k} is the fragmentation function and the momentum fraction is z_c of the parton.

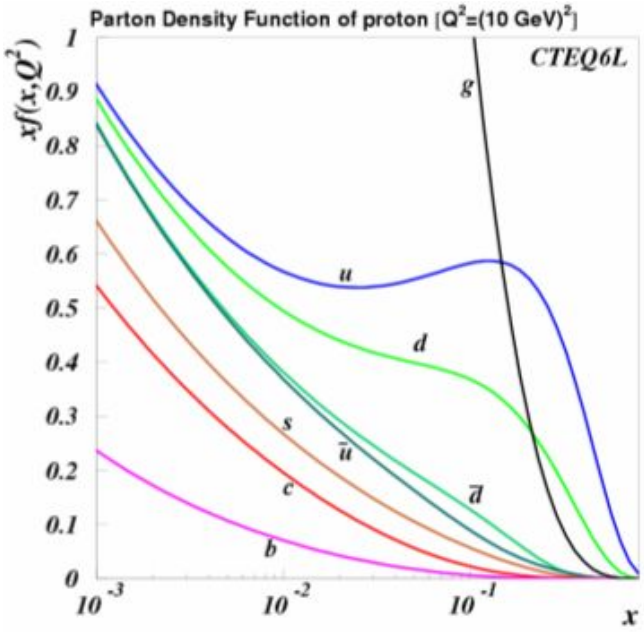

Figure 2.3: The momentum distribution of partons within a proton is called a Parton Density Functions (PDFs). This PDF shows the partons within a proton with a momentum transfer (Q^2) of $(10\text{GeV})^2$ at different fractional momentum x and PDF functions f. CTEQ6L refers to the Coordinated Theoretical-Experimental project on QCD, with 6 being the version and L referring to LO diagrams.

The photon cross section is calculated for $A + B \rightarrow \gamma + X$ as:

$$\sigma_{a_i b_i} = \int f_{a_i/A}(x_{a_i}, a^2) f_{b_i/B}(x_{b_i}, a^2) dx_a dx_b dz_c \sigma_{a_i b_j \rightarrow \gamma_k + X}(\mu_F^2, \mu_R^2) \qquad (\mathbf{2.6})$$

When calculating the photon cross section, the fragmentation function D_{c_k} are equal to one, because photons do not fragment into hadrons.

Directly produced photons are colorless probes of the hard scattering process which are directly sensitive to the gluon content of the proton (through the $qg \rightarrow q\gamma$ process). Thus they can be used to constrain PDFs (see, for examples, [8, 9]). Furthermore, photon identification is important for many physics signatures, including searches for Higgs boson decays to photon pairs, decays of excited fermions, and decays of pairs of supersymmetric particles characterized by the production of two energetic photons and large missing transverse energy.

This analysis measures the photon cross section for inclusive prompt photons. This cross section can be used to constrain PDFs. To measure the cross section, a detector is needed to detect the colliding particles. The detector and the accelerator are discussed in the next chapter.

Chapter 3

The LHC and ATLAS Detector

3.1 Large Hadron Collider

The Large Hadron Collider (LHC) is a 27 kilometer ring that uses superconducting magnets to steer protons and radio frequency (RF) cavities to accelerate protons to high energy. A depiction of the LHC ring and the detectors, is given in Fig. **3.1**. There are four major detectors at the LHC: the Compact Muon System (CMS), A Toridal LHC ApparatuS (ATLAS), A Large Ion Collider Experiment (ALICE), and the Large Hadron Collider B hadrons (LHCb). The CMS and ATLAS detectors are both general purpose, while ALICE is a heavy ion detector, and LHCb is used to study b hadrons.

Figure **3.1** shows not only the LHC ring and the detectors, but also the components used to produce and accelerate the protons. To produce protons, the LINAC2 is used to ionize hydrogen by sending it through an electric field and removing the electron, leaving only bare protons. Then the protons are injected into the booster, which is a linear accelerator used to accelerate the protons further. The protons move to the proton synchrotron booster (PSB) where they are accelerated further. The proton synchrotron (PS) is the next step, in the process. The photons are further accelerated and are "grouped" together forming bunches in the super proton synchrotron (SPS). After leaving the SPS, the protons have an energy of 450 GeV. The 450 GeV protons are then injected into the LHC ring and accelerated to their final collision energy.

The LHC has a design luminosity of $10^{34}\,\mathrm{cm}^{-2}\,\mathrm{s}^{-1}$, with a design center-of-mass energy of $\sqrt{s} = 14$ TeV for proton proton interactions. For heavy ion collisions

the design energy is 5.5 TeV per nuclear pair with a design peak luminosity of $10^{27}\,\mathrm{cm}^{-2}\,\mathrm{s}^{-1}$. The center-of-mass energy is defined as the total energy at an interaction point in the lab frame.

The amount of interactions at the LHC that occur per second is defined as a rate (r):

$$r = La \tag{3.1}$$

Where L is the instantaneous luminosity and a is the cross sectional area of the beam at the interaction point. The cross sectional area of the beam interaction a is defined as:

$$a = \frac{4\pi\epsilon_n\beta^*}{\gamma_r F}, \tag{3.2}$$

where ϵ_n is the normalized transverse beam emittance, β^* is a measure of the beam width (or beta function, representing the beam factorization), γ_r is the relativistic Lorentz gamma factor defined as the energy divided by the proton mass, and F is a factor that accounts for the fact that the two protons cross at a small angle rather than hitting head on. The instantaneous luminosity is defined as:

$$L = \frac{N_p^2 k_p f_{rev}\gamma_r}{4\pi\beta^*\epsilon_n}. \tag{3.3}$$

Where N_p is the number of protons per bunch, k_p is the number of bunches per beam, and f_{rev} is the frequency of revolutions. In a beam crossing there can be multiple interactions due to the large number of protons in the beam. If more than one interaction occurs during a beam crossing, it is called pileup. Pileup can either be defined as in time or out of time. The higher the number of protons in a bunch, the more in time pileup will contribute. In time pileup is caused by additional soft interactions that accompany a hard interaction. Where hard interactions are defined as very energetic collisions between the partons within the

protons and soft interactions are defined by glancing collisions from the protons in the bunch. Out of time pileup is due to the small bunch spacing at the LHC.

A Toridal LHC Apparatus (ATLAS), a detector on the LHC, measures the instantaneous luminosity by performing Van der Meer (vdM) scans. This is done by scanning the beam transversely and by measuring the collision rate as a function of the transverse beam separation [10].

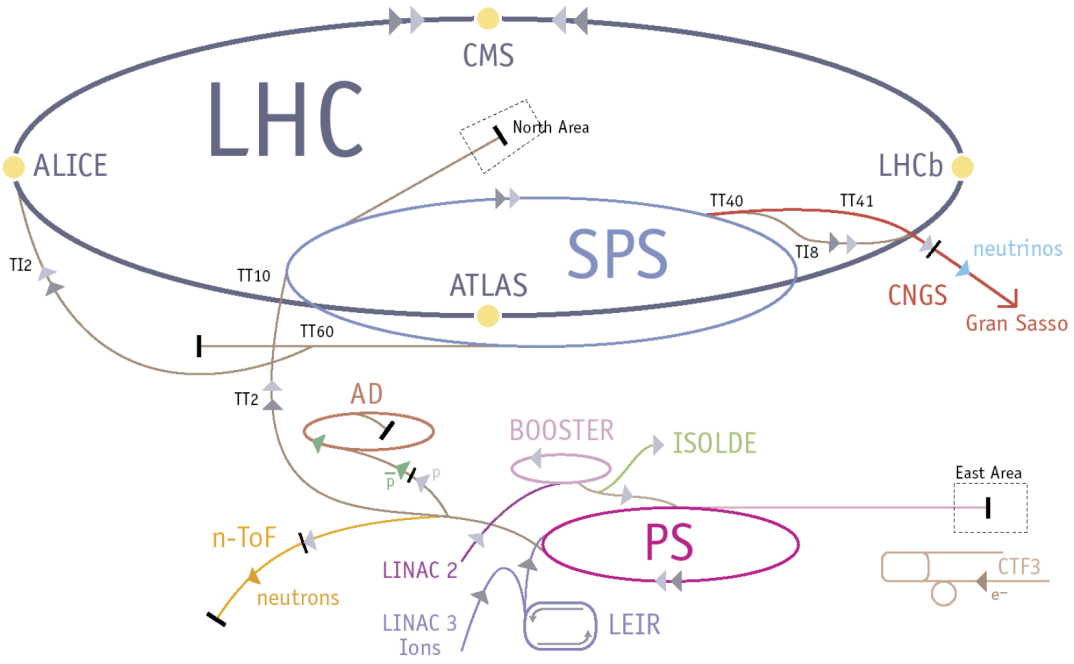

Figure 3.1: The LHC ring with locations for the detectors positioned around the ring.

The amount of data available for analysis is called the luminosity, which is an integral over time of the instantaneous luminosity ($\mathcal{L} = \int L dt$). Large luminosities are preferred to reduce the statistical uncertainty in rare physics processes. High interaction rates are required to obtain high luminosities in a reasonable time. Unfortunately due to these high interaction rates, multiple interactions occur causing high pileup.

3.2 A Toridal LHC AppartuS

Detectors are placed around the collision regions to measure the decay products of the proton collisions. This is done to measure the properties of the decay products of the colliding protons such as their energy, momentum, etc.

The ATLAS detector consist of six separate detector layers and two magnets. Figure **3.2** shows ATLAS which is segmented into three regions: inner detector, calorimeter, and muon detector. The two magnets are the solenoid, located outside of the inner detector and the barrel toroid, located outside of the muon detector. Magnets are used to bend the charged particles trajectories to allow a measurement of the particles momentum. The inner detector contains three layers: the pixel tracker, the silicon micro-strip tracker (SCT), and the transition radiation tracker (TRT). The calorimeter region contains two layers: the electromagnetic calorimeter (ECAL), and the hadronic calorimeter (HCAL). The muon region consists of only a single muon detector.

ATLAS has chosen a coordinate system where the z-axis lies along the beam pipe of the detector as shown in Fig. **3.2**. The x-axis points into the center of the LHC ring, and the y-axis points away from the earth. The nominal interaction point is at $x = y = z = 0$. ATLAS is nominally symmetric in the x-y plane. The azimuthal angle, ϕ, is measured around the z-axis and the polar angle θ is measured from the z-axis. In the z direction the protons energy is known, but not the fraction of momentum the colliding partons carry. Since the colliding partons can have different energies, they are often in a boosted system.

The rapidity y is a Lorentz invariant and is defined as:

$$y = \frac{1}{2} ln(\frac{E + p_z}{E - p_z}). \tag{3.4}$$

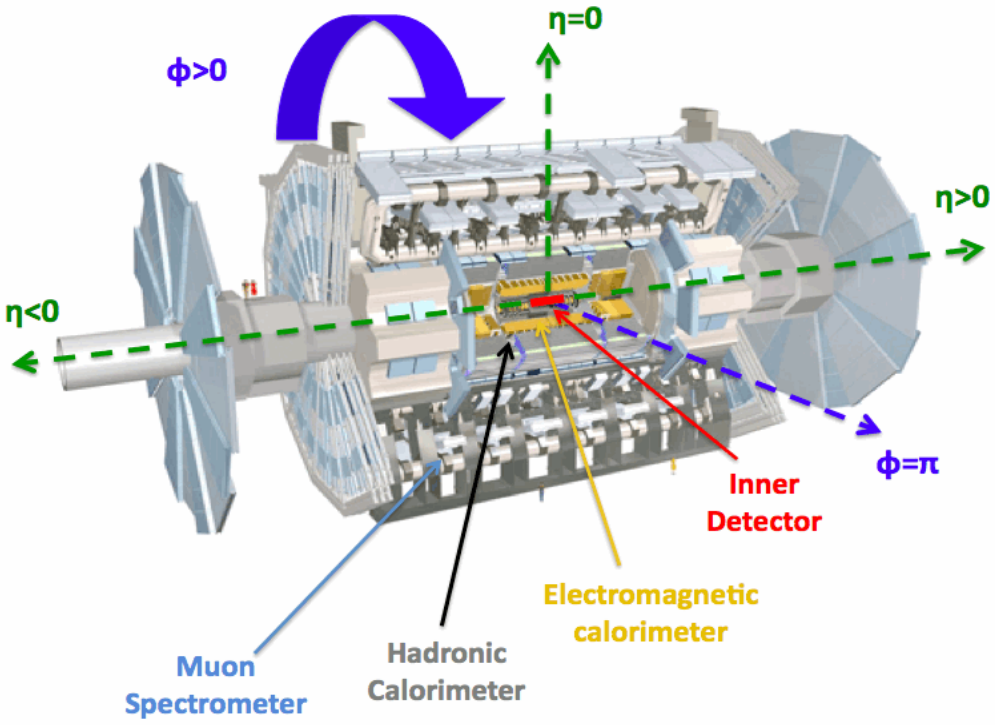

Figure 3.2: The ATLAS detector and the coordinate system chosen by ATLAS.

Since the energy of the particles is so high, their mass can often be neglected. In the approximation where the mass is set to zero, the rapidity becomes the pseudorapidity. The pseudorapidity is defined as:

$$\eta = ln(\texttt{tan}\frac{\theta}{2}). \tag{3.5}$$

The initial energy of the collision in the transverse direction is approximately zero, therefore any significant transverse energy indicates a hard scatter. The variables used in this analysis to describe an event are $E_T(= E\texttt{sin}(\theta))$, $p_T(= p\texttt{sin}(\theta))$, ϕ, and η. In this analysis the massless approximation is used and E_T and p_T are identical.

3.3 Inner Detector

The inner detector allows an accurate reconstruction of charged tracks from the primary proton-proton collision point (primary vertex). It can also identify charged tracks away from the primary vertex, permitting an efficient reconstruction of photon conversions and charged particles in the inner detector up to a radius of $\approx$ 80 cm. These tracks can then be used to identify three types of vertices: primary, secondary and soft vertices. The primary vertex occurs at the primary proton-proton collision point or the initial interaction point. Secondary decays occur away from the primary interaction for longer lived particles such as the B hadron or a K_s. There are also multiple vertices which come from extra interactions in the interaction region called soft vertices. The inner detector lies inside a 2 T axial magnetic field produced by a superconducting solenoid that has full coverage in ϕ. The inner detector is comprised of three subsystems: Pixel, SCT, and TRT, see Fig. **3.3**.

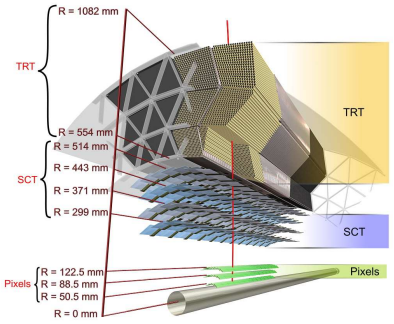

Figure 3.3: Schematic of the inner detectors. The red line indicates the trajectory of a charged particle passing through the inner detectors.

3.3.1 Pixel Silicon Detector

The pixel detector resides at small radial distances R_{rad}, where $R_{rad} = \sqrt{(}\delta x^2 + \delta y^2)$, from the beam axis ($50.5 < R_{rad} < 122.5$ mm). The pixel silicon detectors are arranged in three barrel cylindrical layers and in three end-cap disks on each side. The pixel detector covers the pseudorapidity range $|\eta| < 2.5$. The pixel detector is primarily used to find the primary, soft and any secondary vertices in an event and to detect long lived particles such as b hadrons. Radiation hard silicon is used in the pixel detector to deal with the high radiation environment found near the beam pipe. The pixel detector contains 140 million detector elements housed in 1,744 modules.

3.3.2 Silicon Micro-strip Detector

The SCT lies at intermediate radii of $299 < R < 554$ mm and has double layers of single-sided silicon micro-strip detectors. It is organized in four barrel cylindrical layers and nine end-cap disks. The micro-strip subsystems cover the pseudorapidity range $|\eta| < 2.5$. The SCT primary function is to help find the primary, secondary and soft vertices.

3.3.3 Transition Radiation Tracker

The TRT works on the principle of transition radiation (TR). TR occurs when a relativistic charged particle passes between different media. The TRT uses straw detectors that consist of a wire surrounded by gas consisting of 70% X_2, 27%CO_2 and 3% O_2. The wire acts as an anode and the cylinder acts as a cathode. The TRT is divided into one barrel section (with 73 layers of straws parallel to the beam line) and two end-caps (with 160 layers each of straws radial to the beam line). The transition radiation tracker acceptance is limited to the range of $|\eta| < 2.0$.

The TRT's primary objective is to provide the momentum of charged particles and it can also aid in particle ID.

3.4 Calorimeter

The calorimeter portion of the detector measures the energy left by particles as they are absorbed by the calorimeter. The electromagnetic (EM) calorimeter (ECAL) is designed to contain all of the energy from electrons and photons and the hadronic calorimeter (HCAL) is designed to contain the energy of particles that make it through the EM calorimeter (except muons and neutrinos). The ECAL and HCAL are shown in Fig. **3.4**. Both calorimeters are sampling calorimeters which use both a sampling material and an absorbing material. Sampling calorimeters are designed to only measure a portion of the energy that strikes the calorimeter. The energy that is read out is then calibrated to match how much energy is actually lost in the detector.

3.4.1 Electromagnetic Calorimeter

In the ECAL shown in Fig. **3.5**, a particle's position and energy can be measured with very high resolution. Lead acts as the absorbing material and liquid argon as the sampling material. The EM portion is at least 22 radiation lengths thick (A radiation length is the distance in which an electron loses 1/e of its energy). Electrons and photons tend to shower in the calorimeter in a very uniform manner, so having fine granularity in the ECAL helps dramatically in identifying and measuring photons and electrons. The ECAL is a lead-liquid Argon (Pb-LAr) sampling calorimeter with an accordion geometry. The reason for the accordion geometry is not only to prevent particles from not interacting in the gap region, but also to lessen the amount of time required to read out a signal. It is divided

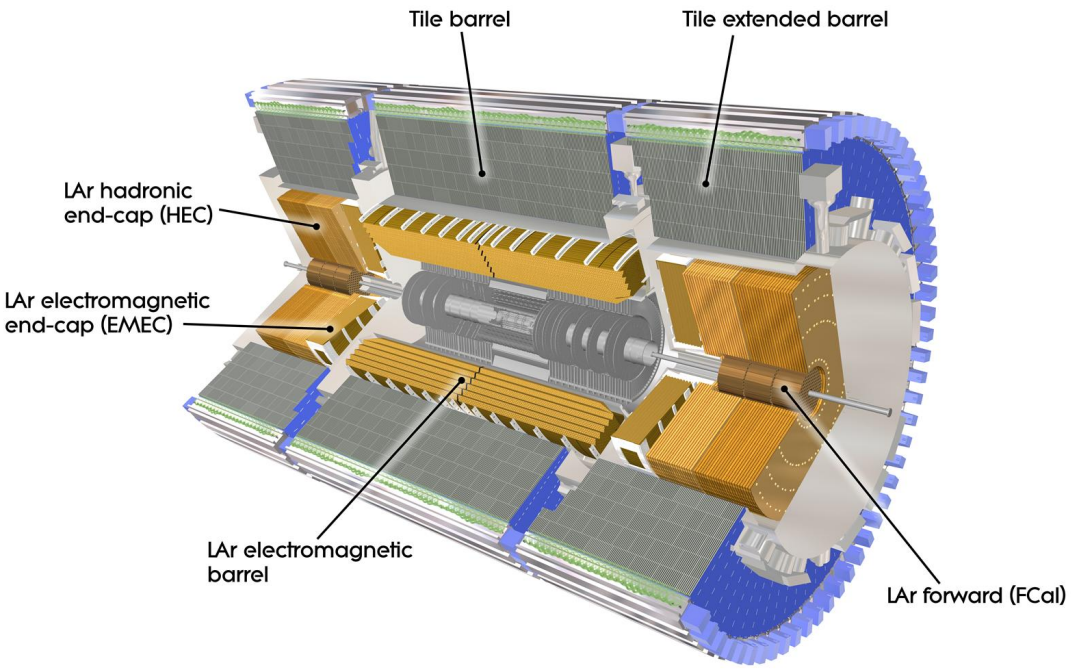

Figure 3.4: The calorimeter portion of ATLAS.

into a barrel section covering the pseudorapidity region $|\eta| < 1.47$ and two end-cap sections covering the pseudorapidity regions $1.37 < |\eta| < 3.2$. It consists of three separate longitudinal layers. The first layer, with a thickness between 3 and 5 radiation lengths, has a very high granularity along the η direction (between 0.003 and 0.006 in $\eta \times \phi$ depending on η). This is sufficient enough to provide event-by-event discrimination between single photon showers and showers coming from π^0 decays. The second layer of the electromagnetic calorimeter, which collects about two-thirds of the energy deposited in the calorimeter by the photon, has a thickness of approximately 17 radiation lengths and a granularity of 0.025×0.025 in $\eta \times \phi$. The third layer, with thickness varying between 4 and 15 radiation lengths, is used to capture the remaining energy. If there is leakage beyond the electromagnetic calorimeter the energy of the third layer is corrected. It is important to know the true energy of particles, so the leakage needs to be accounted for. This is done by taking the information from the first HCAL layer, in a window of $\Delta\eta \times \Delta\phi = 0.2 \times 0.2$, to the transverse energy reconstructed in the ECAL portion. If this ratio is above some designated threshold, then leakage has occurred. This is done based on each particle instead of applying a universal correction to reduce the dependence on resolution.

Before the accordion shaped calorimeter, a thin presampling layer covering the pseudorapidity interval $|\eta| < 1.8$ is used to correct for the energy lost in front of the calorimeter. A proper description of the material is important for accurate modeling of the calorimeter response including the detailed shape of electromagnetic showers.

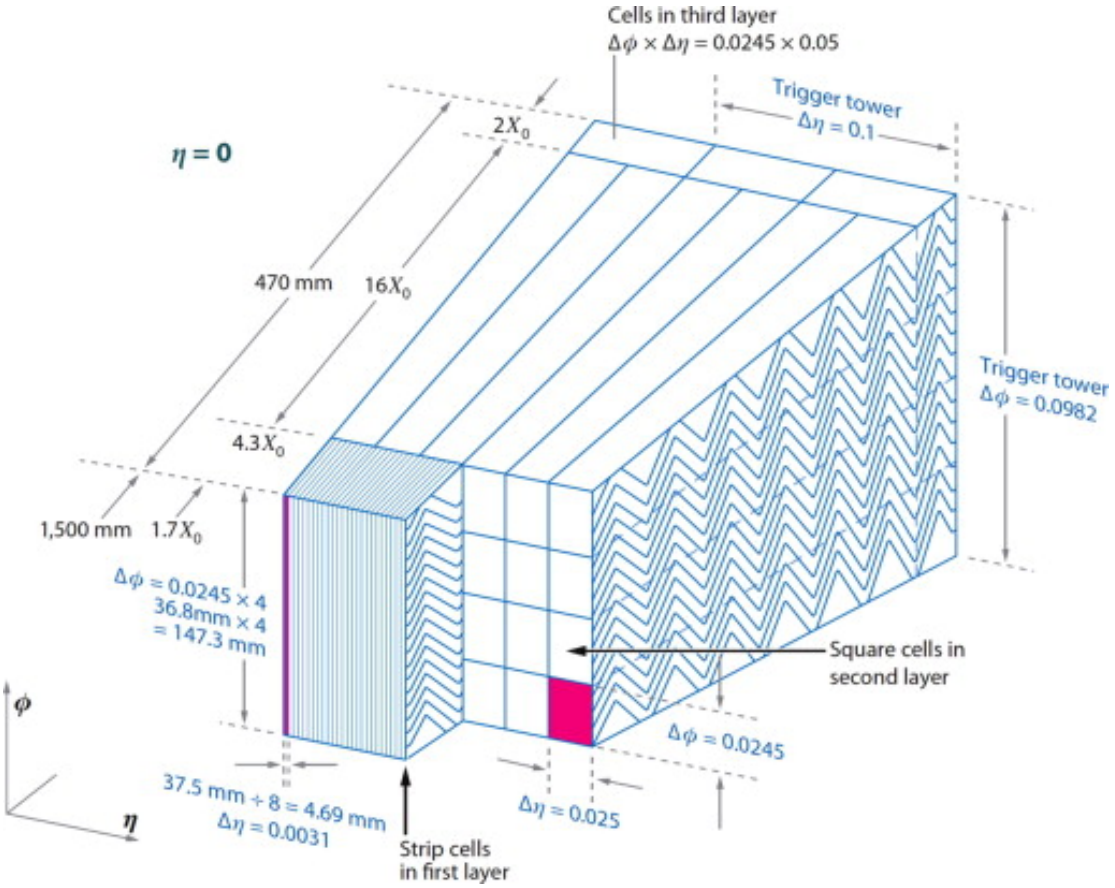

Figure 3.5: The ECAL portion of the detector.

Radiation Lengths

A radiation length x_0 is the amount of energy lost from a particle in a particular material. It is defined as:

$$x_0(\frac{g}{m^2}) = \frac{716.4(gcm^{-2})A}{z(z+1)ln(287/\sqrt{z})}. \quad (\mathbf{3.6})$$

Where z is the atomic number, and A is the atomic weight of the material. Higher z materials have shorter radiation lengths. Electrons and photons will lose some energy interacting with the inner detector material, so it is desirable to have a small amount of material before the calorimeter. The amount of the particle's energy that is lost in the material is defined by the linear absorption coefficient.

The linear absorption coefficient is defined as the fraction of a particles energy that is absorbed per thickness of a material.

Photon Energy Loss

When photons and electrons interact through matter, there are multiple ways for them to lose energy or interact with matter. At low energy, the KeV to MeV scale, photons and electrons lose energy primarily through the photoelectric effect and the Compton effect. The photoelectric effect is the process where by when photons strike a metal surface, electrons are emitted. The Compton effect is when an electron will interact with material causing a photon to be emitted. In ATLAS the main energy of the photons that are studied are in the GeV range (1-1000 GeV). For this particular analysis, photons are required to be above 100 GeV. These high energy photons lose energy primarily through Bremsstrahlung and pair production.

Bremsstrahlung is the radiation produced by the deceleration of a charged particle when it is deflected by another charged particle. In Bremsstrahlung, photons lose energy through the radiation of additional photons. This is described by:

$$E(x) = E_0 e^{\frac{-x}{x_0}}, \tag{3.7}$$

where x_0 is the radiation length and x is the material thickness.

Pair production is when a photon transverses close to a nucleus and the resultant energy causes an electron positron pair to be created. This is described by:

$$I(x) = I_0 e^{\frac{-7x}{9x_0}}. \tag{3.8}$$

The energy lost is similar to Bremsstrahlung but has a linear absorption coefficient of 7/9.

ECAL Resolution

The ECAL resolution is defined by:

$$\frac{\Delta E}{E} = \frac{a}{\sqrt{E}} \otimes \frac{b}{E} \otimes c. \tag{3.9}$$

Where a is the stochastic term (sampling term), b is the noise term, c is the constant term, and $\otimes$ represents a quadratic sum. The stochastic term deals with the statistical fluctuations in shower development. The noise term deals with the readout electronics chain as well as pileup. The constant term deals with non energy dependent effects such as: the material non-uniformity, temperature, radiation, and leakage. The sampling term a of the photon energy resolution ($\Delta/E \approx a/\sqrt{E\ (\mathrm{GeV})}$) varies between 10% and 17% as a function of $|\eta|$ [11], and is the largest contribution to the resolution up to about 200 GeV, after which the global constant c term (0.7%) starts to dominate [12].

Readout Electronics Chain

The particles in the ECAL portion ionize in the liquid argonne (LAr) and in order to readout this ionization energy, high voltage (HV) plates are inserted in the LAr portion, see Fig. **3.6**. The HV plate is made of copper kapton layers and is independently charged. This design was chosen because in an instance of a loss of power on one side, half the signal can be still readout. The analog signal that comes from the ionization energy is triangular in shape and is seen in Fig. **3.7**. This signal is read into Front End Boards (FEB) which shapes and samples the signal. This analog signal is then converted to a digital signal using an analog to digital converter or ADC. The ADCs are calibrated by using particles of known energy and measuring the digital output.

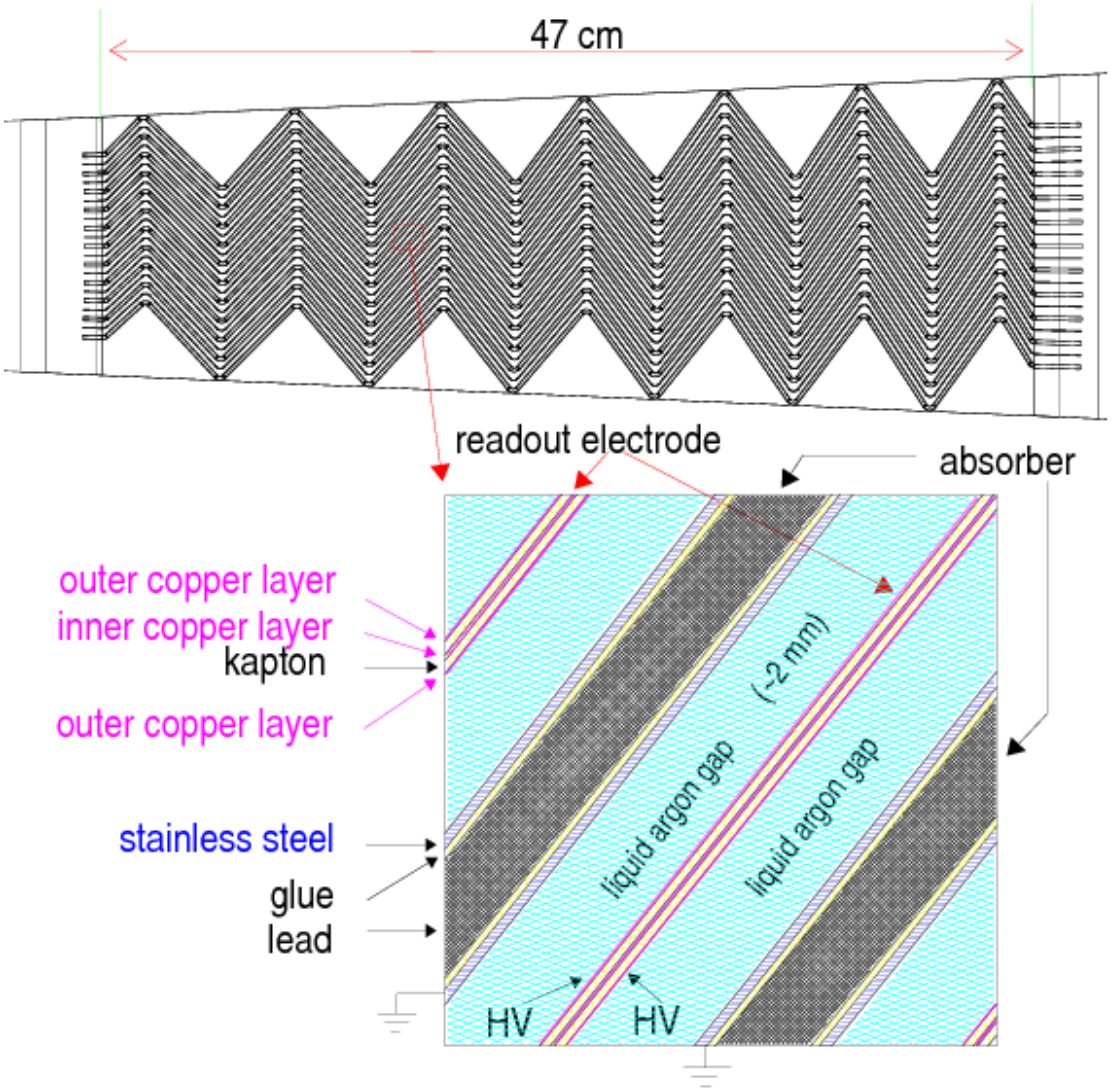

Figure 3.6: Schematic of the ECAL including a description of a cell.

Energy Calibration

Energy calibration for the ECAL portion of the detector is performed in three steps. The first step is to send a voltage pulse to the resistors in the ECAL detector. The raw electronic ECAL signals from this pulse are converted to an energy value. The next step is to apply a correction factor due to energy loss. This correction factor is based on Monte Carlo simulations of the detector. The final step is to reconstruct the $Z \rightarrow e^+e^-$ mass in data and compare it to the MC

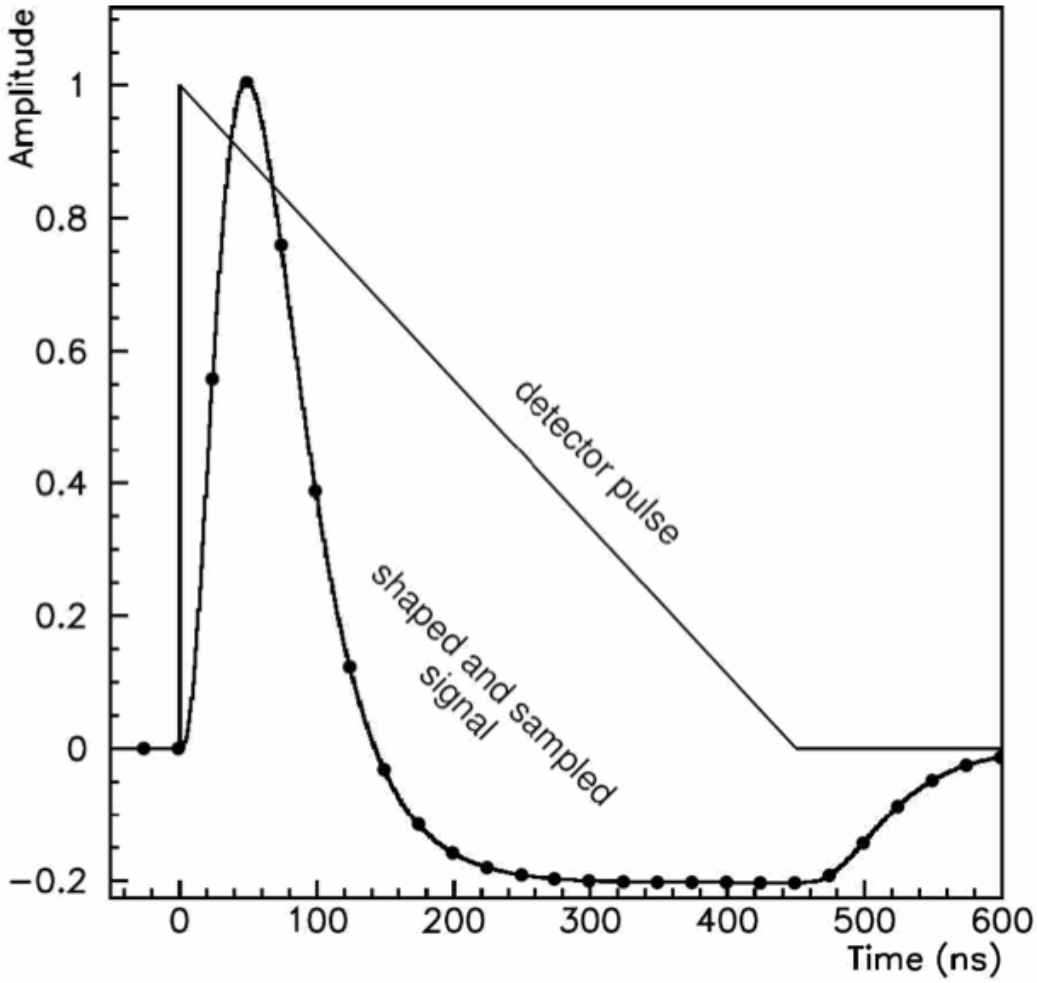

Figure 3.7: An example of a detector pulse, as well as the shaped and sampled signal. This shaped signal is shaped by the front end boards (FEB).

simulations. Since the mass of the Z is well known, any miscalibration energy can be calculated. The true energy E_{true}, is found from the measured energy E_{meas}, using $E_{meas} = E_{true}(1 + \alpha_J)$, where α_j, is found in 26 different η regions. Other decays can be used to get a wider range of energy including $J/\Psi \rightarrow e^+e^-$, which allows corrections down to 5 GeV.

3.4.2 Hadronic Calorimeter

The HCAL is designed to absorb the energy of particles that make it through the ECAL (except muons and neutrinos. The absorbing material is lead and the sampling material is plastic scintillators. The hadronic calorimeter is 9.7 interaction lengths thick (an interaction length is the length required to reduce the energy through hadronic interactions by a factor of 1/e). The large number of interaction lengths cause all of the particles, not including muons and neutrinos, to lose all their energy within the combined HCAL and ECAL.

3.4.3 Muon Detector

The last detector layer of ATLAS is the muon detector. Muons are long lived low ionizing particles which can travel all the way through the calorimter portion of the detector to reach the muon detector. Thus, any detectable particle that makes it through the calorimeter must be a muon. A toroidal magnet sits outside of the muon detector, allowing for momentum measurements to be performed on the muons. There are two different kinds of detectors used in the muon system: monitored drift tubes (MDT's) chambers and the cathode strip chambers. The two detectors are arranged in eight octants with an azimuthal symmetry. The MDT's provide a precise measurement of track coordinates. Cathode strip chambers are used for measuring transverse momentum in the endcap region of the muon detector.

3.5 Data Samples

The data being used for this analysis were collected in 2011 using the ATLAS detector with a trigger that detects photons that have a transverse energy greater

than 80 GeV. In this section the specifics on the amount and type of data are discussed, as well as the trigger details.

3.5.1 Collision Data

The measurement presented here is based on proton-proton collision data collected at a center-of-mass energy of $\sqrt{s}$ =7 TeV with the ATLAS detector at the LHC between March and October 2011. The total integrated luminosity of the sample used in this measurement is 4.64 ± 0.08 fb^{-1} [13], and includes a correction that accounts for beam-beam effects during the vdM scans. For this analysis, events are required to have at least one reconstructed primary vertex with at least three associated tracks consistent with the average beam-spot position. Only events where both the calorimeter and the inner detector are fully operational and which have good data quality are used.

3.5.2 Trigger System and Requirements

ATLAS has designed a three level triggering system to deal with the high rate of data. The triggering system is designed to collect only the interesting interactions. The three levels are called: level-1 (L1), level-2 (L2), and the high-level Trigger (HLT).

3.5.3 Level-1 and Level-2

The L1 trigger is completely electronics based. The time it takes the L1 trigger to make a decision is 2.5 μs. There are three systems that help to make the L1 trigger decision: the level-1 muon (L1 muon), level-1 calorimeter trigger (L1 calo), and the central trigger processor (CTP). The L1 muon trigger is used to identify high p_T muon candidates. The L1 calo identifies high E_T objects as well as the

sums of energies that are of interest. The CTP processes the information from both the L1 muon and the L1 calo. When a L1 decision is made, this information and information from the surrounding towers are used in the L2 trigger. The main purpose of the L2 trigger is to reduce the data to a manageable amount that the HLT can use to build events. This is done by having stricter criteria than the L1 trigger and combining subdetector information. For this analysis a L1 calo trigger above a 30 GeV threshold (`L1_EM30`) is used. The `L1_EM30` has a granularity of 0.1×0.1 in $\eta \times \phi$. The amount of time available to process the L2 trigger is approximately 10 ms.

3.5.4 High-Level Triggers

The high-level triggers (HLT) are the final step in the trigger chain. Information that pass the L2 trigger is sent to the HLT. Three separate trigger quality criteria are often defined as: "loose", "medium", "tight". As one moves from "loose" to "tight" the qualifications become more stringent. Events are triggered using the `g80_loose` high-level calorimeter trigger based on the energy deposits in the ECAL and HCAL. The high-level trigger exploits the full granularity and precision of the calorimeter to refine the level-1 trigger selection based on improved energy resolution and detailed information on energy deposition in the calorimeter. The nominal transverse energy threshold of the `g80_loose` trigger is 80 GeV. The trigger selection criteria that is applied by the trigger (on the fraction and profile of the energy detected in the various layers of the calorimeters) are looser than the photon identification criteria applied in the analysis to avoid any trigger bias. The `g80_loose` trigger is chosen for this analysis since it reaches a plateau of constant efficiency close to 100% with respect to the offline selection for true photons. For this analysis any photons with $E_T^\gamma > 100$ GeV which are used Ref. [2].

At $E_T^\gamma > 85$ GeV, the efficiency is $100(^{+0}_{-3})\%$ for the g80_loose trigger [2]. The efficiency for both the g60_loose and the g80_loose triggers are shown in Fig. **3.8**.

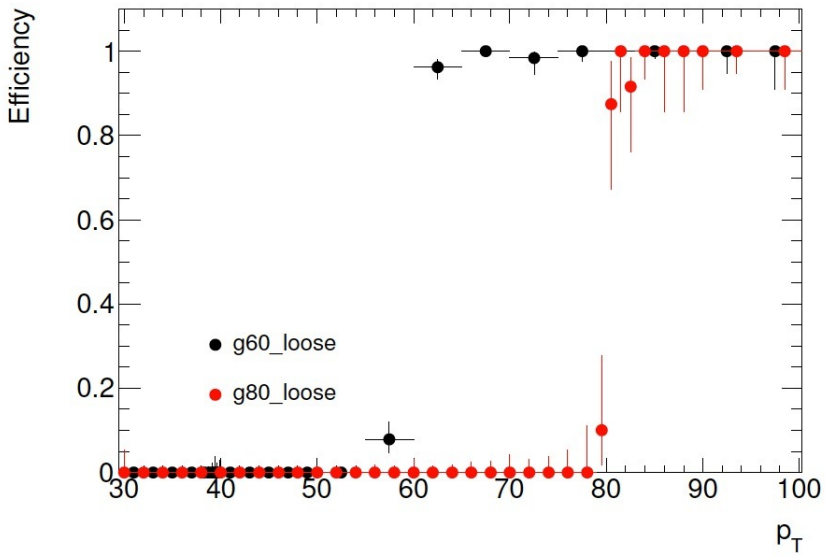

Figure 3.8: Efficiencies of g60_loose and g80_loose triggers with respect to offline tight photons. Uncertainties are statistical only.[2]

Chapter 4

Simulated events

Monte Carlo (MC) is used to simulate different physics processes. The simulated physics processes for this analysis are quantum chromodynamics (QCD) and quantum electrodynamics (QED) radiation. Full QCD is difficult to calculate exactly, so perturbative QCD (PQCD) must be used. For PQCD a series expansion in α_s is performed, where the most common orders used are leading-order (LO) and next-to-leading-order (NLO). This was discussed in more detail in Chapter 2.

MC generators typically simulate events in three separate steps: parton showering (PS), hadronization, and multiple interactions (MI). PS is done by simulating a successive generation of random gluon emissions ($g \rightarrow q\bar{q}$). Each successive process has lower energy than the previous one and will decay down to approximately 1 GeV of energy. After this is done, the processes are then ordered in some way depending on what MC generator is used. For example the `PYTHIA` generator orders the processes in momentum. Following the PS, hadronization is performed by converting partons into hadrons. The final step is to include MI. The reason that this is important is because in a proton proton (pp) collision underlying events (UE) can occur. These additional interactions need to be simulated because they are not included in the original PS. The UE comes from more than one quark or gluon interacting in the hard process. MI is included in the MC by taking the remaining particles and implementing additional $2 \rightarrow 2$ scatters.

The MC generators used in this analysis are `HERWIG` [14], `PYTHIA` [15], and `JETPHOX` [5, 16]. The LO processes are generated with `HERWIG` and `PYTHIA`, while the NLO processes are calculated with `JETPHOX`.

In order to compare MC to data, the effects of the detector either need to

be removed from the data or it must be included in the MC. A program called GEANT [17] simulates the amount of material and the detector response for particles. Once the MC is processed by GEANT, the effects of the detector have been implemented, so the events can be processed with the same reconstruction code as data. One important check that can be done to verify if GEANT is simulating the detector well is to compare the number of primary vertices (PV). Good agreement for the number of PV between PYTHIA and the data samples is shown in Fig. **4.1**. It is important that the ECAL distributions between data and MC agree. Figure **4.2** compares MC to data for two of the photon selection variables used in this analysis and reasonable agreement is found. Figure **4.3** compares the $Z \rightarrow e^{-}e^{+}$ mass distribution for both MC and data for both the electromagnetic energy scale and the resolution.

4.1 Leading Order Monte Carlo

PYTHIA and HERWIG can simulate a broad range of QCD processes as well as QED radiative processes. Both are LO generators but deal with hadronization different.

PYTHIA orders in momentum after the PS occurs. The hadronization is simulated with a Lund-String model [18]. Hadronization is performed by stretching a color "string" across quarks and gluons which leads to a breaking into hadrons.

HERWIG orders in angle after the PS occurs. Hadronization for this generator is done with cluster-hadronization. For cluster hadronization, each quark is grouped into quark anti-quark pairs ($q\bar{q}$). These pairs are grouped to give rise to colorless clusters which form hadrons.

Both HERWIG and PYTHIA implement MI identically. A program called ATLAS AUET2 [19] is used to simulate MI at ATLAS.

Process	σ [pb]	Filter thres. [GeV]	Filter efficiency	Events tuples	Equivalent luminosity [pb^{-1}]	Gen.
QCD	3.664E+03	70	1.780E-01	999948	8.180E+02	PYTHIA
QCD	6.970E+00	140	3.060E-01	997451	8.170E+03	PYTHIA
QCD	1.225E+02	240	3.060E-01	997346	3.430E+05	PYTHIA
QCD	8.204E-02	500	5.420E-01	99945	1.220E+07	PYTHIA
QCD	3.667E+03	70	4.720E-04	997426	6.690E+02	PYTHIA
QCD	1.224E+02	140	8.420E-04	996300	1.100E+04	PYTHIA
QCD	2.920E+00	280	1.340E-03	996711	2.830E+05	PYTHIA
QCD	8.183E-02	500	1.680E-03	999866	1.220E+07	PYTHIA
γ-jet	1.629E+03	70	6.639E-01	999943	9.250E+02	PYTHIA
γ-jet	8.923E+01	140	7.956E-01	999940	1.410E+04	PYTHIA
γ-jet	3.443E+00	280	8.526E-01	999327	3.400E+05	PYTHIA
γ-jet	1.321E-01	500	8.706E-01	99995	8.690E+05	PYTHIA
γ-jet	1.330E+00	70	5.920E-01	999996	7.510E+05	HERWIG
γ-jet	7.250E-02	140	7.000E-01	999697	1.380E+07	HERWIG
γ-jet	2.790E-03	280	7.460E-01	999990	3.580E+08	HERWIG
γ-jet	1.070E-04	500	7.500E-01	99997	9.350E+07	HERWIG
QCD	2.727E+03	70	1.586E-04	990700	2.289E+06	HERWIG
QCD	9.254E+01	140	2.333E-04	989500	4.581E+07	HERWIG
QCD	2.259E+00	280	3.010E-04	983000	1.445E+09	HERWIG
QCD	6.452E-02	500	3.398E-04	97600	4.450E+09	HERWIG

Table 4.1: Monte Carlo datasets used in the inclusive photon analysis. All samples contain all relevant signal processes, unless otherwise indicated. The QCD samples contain both prompt photon production events and the most significant sources of background as summarized in Table **4.2**.

To study background processes, MC samples enriched in photon candidates with reconstructed transverse energies $E_T^\gamma > 100$ GeV are used. In these samples, all relevant 2→2 QCD hard subprocesses (see Table **4.2**) are included. Events that are fully simulated are then selected by requiring that the transverse energy in a 0.18×0.18 region in $\eta \times \phi$ at the truth particle level be above a certain threshold, varying between 70 and 500 GeV. The full list of the MC samples with their equivalent luminosities is shown in Table **4.1**. All of the QCD background samples (which are labeled as background) contain "fake" photon candidates (typically from π^0 and $\eta \to \gamma\gamma$ decays), as well as prompt-photon signals produced by

QED radiation emitted off quarks. They also include direct LO gamma-jet hard-scattering contributions, either from $q_i\bar{q}_i \rightarrow g\gamma$ or $q_i g \rightarrow q_i\gamma$.

For the samples, we consider several backgrounds and signals the identifying names are:

- `PYTHIA` samples contain both hard-scattering photons and photons from QED radiation emitted from quarks. These samples are called "PYTHIA signal" samples. The events generated in these samples are similar to those generated for the study of the QCD backgrounds (the same elementary processes are activated), but the filter applied before the full simulation only retains events that contain generated photons with transverse momenta above a threshold (70-500 GeV for the current studies). These samples are used to study both the identification efficiency and the purity of the selected prompt photon signal.

- `PYTHIA` and `HERWIG` samples containing only leading-order photon-jet events (generated hard subprocesses $qg \rightarrow q\gamma$ and $q\bar{q} \rightarrow g\gamma$) and the event must contain hard-scattering photons with generated transverse momenta above a threshold (70-500 GeV for the current studies). These samples are used primarily in evaluating the effect of different generators (`HERWIG` vs. `PYTHIA`) in the estimated efficiency and purity of the prompt-photon signal. These samples are called `PYTHIA` fragmentation and `HERWIG` fragmentation respectively.

- `HERWIG` samples containing only dijet events where there is a photon radiated off a parton with transverse momentum above a certain threshold (70-500 GeV for the current studies). These samples are called "HERWIG signal" samples. They deal with the direct photon process. `HERWIG` does not allow for the simultaneous generation of direct photons in the same sample as the

hard-scattering photon-jet processes, unlike the "PYTHIA signal" samples. In order to compare PYTHIA signal to HERWIG, the HERWIG signal samples are combined with the HERWIG fragmentation samples. This provides an alternative estimate of the prompt (direct+fragmentation) photon efficiency.

Process	PYTHIA subcode
$q_i q_j \to q_i q_j$	11
$q_i \bar{q}_i \to q_k \bar{q}_k$	12
$q_i \bar{q}_i \to gg$	13
$q_i g \to q_i g$	28
$gg \to q_k \bar{q}_k$	53
$gg \to gg$	68
$q_i \bar{q}_i \to Q_k \bar{Q}_k$	81
$gg \to Q_k \bar{Q}_k$	82
$q_i \bar{q}_i \to g\gamma$	14
$q_i g \to q_i \gamma$	29

Table 4.2: Elementary QCD processes that are enabled in the QCD PYTHIA samples ($q = u, d, s, c, b$, $Q = t$).

4.2 JETPHOX

NLO calculations should provide a better description of the hard sub-processes. On ATLAS, JETPHOX is used to determine the direct photon cross section to NLO. The JETPHOX program has the capability to inputs various PDFs. This analysis inputs two PDFs: the nominal PDF is CT10 while MSTW2008 is used for comparison purposes. In JETPHOX the direct and fragmentation functions can be calculated separately. The fragmentation portion is difficult to calculate and was found to be a small contribution to high momentum calculations. When using PQCD, scales must be introduced to deal with unphysical results. These scales are the renormalization, factorization and fragmentation scales, which were discussed in more detail in Chapter 2. For this analysis the nominal renormalization (μ_R),

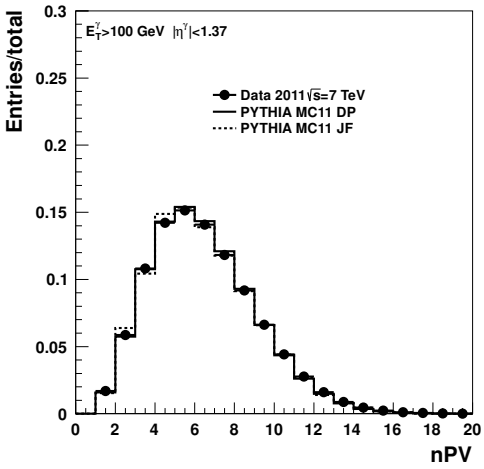

Figure 4.1: The number of primary vertices (nPV) for events with at least one (loose or tight) photon with $E_T^\gamma > 100$ GeV compared to the Monte Carlo simulations.

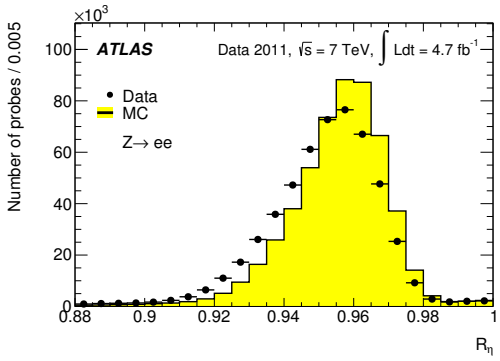

(a) R_{had}

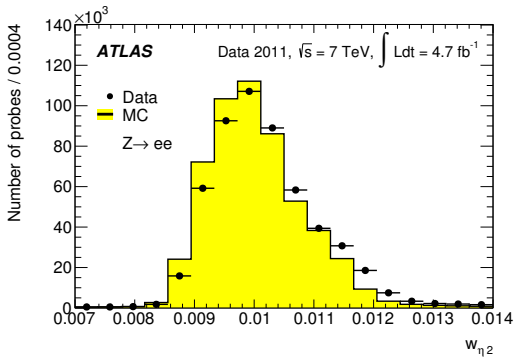

(b) $w_{\eta 2}$

Figure 4.2: Fig. shows a comparison of a variable used in the selection process for both data and MC [3].

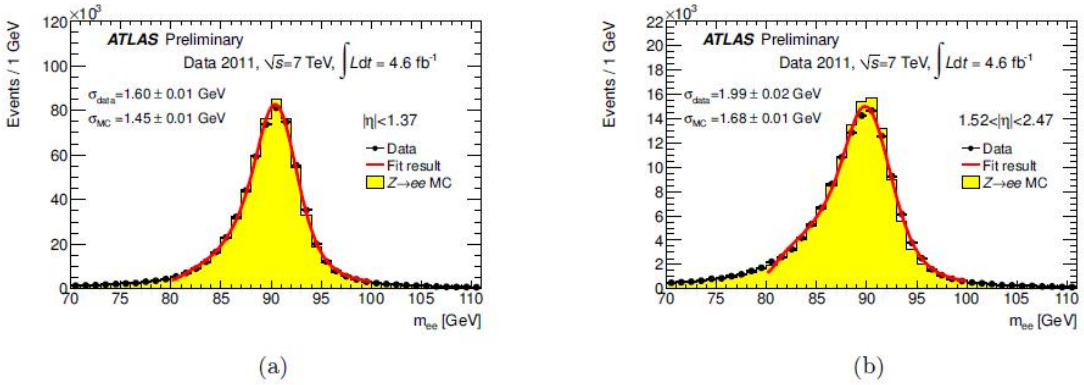

Figure 4.3: The invariant mass of $Z \to e^- e^+$ for both data (after full calibration) and MC. (a) Events with both electrons in $|\eta| < 1.37$ (b) Events with at least an electron in $1.52 < |\eta| < 1.37$ [4].

factorization (μ_F) and fragmentation (μ_f) scales have been set to the photon transverse energy E_{T}^{γ} ($\mu_R = \mu_F = \mu_f = p_{\mathrm{T}}$).

Chapter 5

Photon Reconstruction

There are two categories of photons that are reconstructed for this analysis: unconverted photons and converted photons. An unconverted photon is a photon that only has energy deposited in the ECAL portion of the detector. A converted photon is a photon that not only has energy in the ECAL portion of the detector but also has at least one track associated with the energy cluster. It is important to include converted photons since approximately 30% of photons will convert before reaching the ECAL. Since electrons are also reconstructed in the same manner as converted photons, there is a set of selection requirements that are used to distinguish electrons from converted photons. In this chapter the reconstruction of both unconverted and converted photons is discussed, the selection criteria used to distinguish electrons from photons, as well as the identification of these photons.

5.1 Reconstruction Algorithms

To reconstruct photons there are two different algorithms that are used: the sliding window and the topological cluster (topo cluster). A cluster is defined as a group of calorimeter cells in the ECAL portion of the calorimeter. For this analysis, the sliding window algorithm was chosen to reconstruct photons, and the topological cluster algorithm was used as a systematic cross check.

5.1.1 Sliding window algorithm

The sliding window algorithm uses a rectangular region that is fixed in size in $\eta \times \phi$ space and is positioned so the maximum amount of energy is contained within that fixed window. The size of the window used depends on the reconstructed particle. Unconverted photons use a smaller window than converted photons. Electrons and converted photons use a larger window because they are more likely to interact with material in the detector. There are three separate steps to making clusters with the sliding window algorithm: tower building, precluster finding, and cluster filling.

First the fixed window is moved over the ECAL towers in increments of $\eta \times \phi$ and a local energy maximum is found. This is called tower building. A group of cells that contain the local maximum is defined as a precluster. For preclustering a 5×5 window in $\eta \times \phi$ cells, where this is five cells in η and five cells in ϕ, is used, with a minimum energy threshold of 3 GeV. The position and energy of all preclusters are stored. Preclusters that are within a duplicate range in $\Delta\eta \times \Delta\phi$ cells are compared and the preclusters with the maximum energy is kept and the precluster with the smaller energy is removed from consideration.

Preclusters are then combined using a 3 x 5 window in $\eta \times \phi$ for unconverted photons in the barrel region. For converted photons (which are treated like electrons at this stage) and electrons in the barrel region, a 3×7 window in $\eta \times \phi$ is used. For the endcap region, a 5 x 5 window in $\eta \times \phi$ is used for both types of photons and electrons. After preclusters are found in the second ECAL layer, clusters which combine all of the layers of ECAL are formed.

5.1.2 Topological Clusters

For the topo cluster algorithm, clusters that have significantly more energy (approximately four times the noise threshold) compared to the noise are used to reconstruct photons. The clusters have a variable size compared to the sliding window algorithm. The topo cluster algorithm consists of two steps: cluster making and cluster splitting.

Cluster making is a three step process where the initial guesses for the cluster centers are defined, neighbors are compared and the finalizing of clusters is done. If the signal to noise ratio is greater than a threshold of approximately six, it is listed as a primary initial guess (the initial guesses are called seeds). Once all the seeds are found, they are listed in descending order in the signal to noise ratio. The seed is used to find neighboring cells. The neighboring cells are defined as the eight cells surrounding a seed within a calorimeter layer. If the neighboring cell is above a signal to noise ratio of three, it is combined with the seed in what is called a "proto-cluster". A new seed list that contains the neighboring cells is made and the process is repeated until no seeds are left.

When the cell is adjacent to more than one "proto-cluster" then the "proto-clusters" are combined. Once all of the cells are combined and all of the "proto-clusters" are merged, these grouping of cells become clusters. For the topocluster algorithm the "proto-clusters" and clusters can be formed from more than one layer of the ECAL. However when combining multiple layers in the ECAL the potential for introducing noise is high, so only the second layer of the ECAL is used for finding "proto-clusters". After all clusters have been found, the cluster splitting algorithm is run.

Cluster splitting is important because there can be overlapping reconstructed particles or showers, and in order to distinguish these, a cluster splitting algorithm

is used. To use this algorithm, local maximum within a cluster are found. The criteria for a local maximum is that the energy is greater than 500 MeV, the energy has to be greater than any neighboring cells and the number of neighboring cells in a cluster is greater than some threshold (usually greater than or equal to four). Once a cluster is found to pass these criteria, the cluster is split. When a cell is shared between two clusters, a new list of shared clusters is made to be handled separately.

With the shared list, the cells that share two clusters are added to the cluster with a weight. The weight is defined as:

$$w_1 = \frac{E_1}{E_1 + rE_2}, \quad w_2 = 1 - w_1, \quad r = exp(d_1 - d_2) \tag{5.1}$$

Where $E_{1,2}$ is the energy of each proto-cluster, and $d_{1,2}$ is the distance from the shared cell to the proto-cluster centroid. The weight gives the probability that the cell should be contained in one cluster or the other. The weight, which deals with the distance between the cells, is usually either nearly 0 or nearly 1. After all splitting is finished, all of cells are converted to clusters.

5.2 Converted Photons

Since converted photons are reconstructed similarly to electrons, an algorithm is required to separate them. The conversion vertices that are detected are mostly from $\gamma \rightarrow e^+e^-$ decays. This is because of the type and amount of material in the tracking portion of the detector where photon conversions occur. The algorithm used to separate out the secondary vertices that come from conversion photons can include cuts on: calculating the opening angle between the tracks (should be small), radial distances between the first hits (should be small), and the minimum

distance between tracks (should be small). If there is a double track the tracks should be close together to be converted photons. For a single track, which will happen if there is not a lot of separation between the electron positron pair, or one track is at a small momentum and not reconstructed this is reconstructed as a converted photon if there is no pixel B-layer hit.

5.3 Photon identification

Shape variables computed from the lateral and longitudinal energy profiles of the shower in the ECAL are used to discriminate the signal from the background, and an example of this is shown in Fig. **5.2**. These shape variables discriminate between "loose" and "tight" photons. The shower shape variables used are: R_{had1}, R_{had}, R_{η}, w_{η^2}, R_{ϕ}, w_{stot}, $w_{s\,3}$, $F_{\rm side}$, ΔE, and $E_{\rm ratio}$, and are described in Table **5.1**. Figure 5.3 shows a comparison for the signal and background for 2010 ATLAS data for some of the variables listed above.

The R_{had}, and R_{had1} variables deal with hadronic leakage. R_{had} is a ratio of the energy in the HCAL to the energy in the photon cluster. R_{had1} is a ratio of the transverse energy in the first sampling layer of the hadronic calorimeter to the EM cluster.

The R_{η}, w_{η^2}, and R_{ϕ}, all deal with the second layer (S2) of the ECAL. R_{η} measures the spread of energy in η by taking the ratio of the energy in η in cells of 3 x 7 which is defined as $E^{S2}_{3\times7}$ to cells of 7 x 7 which is defined as $E^{S2}_{7\times7}$. w_{η^2} characterizes the lateral width of a shower in η. R_{ϕ} is a similar ratio as R_{η}, but in the ϕ region of the cells, and the window size used is a 3×3 divided by 3×7.

The w_{stot}, $w_{s\,3}$, $F_{\rm side}$, ΔE, and $E_{\rm ratio}$ deal with the strip layers (S1) in the ECAL. w_{stot} measures the weighted lateral shower width in η over all of the strips. $w_{s\,3}$ is the same as w_{stot} but is only measured in three strip layers. $F_{\rm side}$ measures

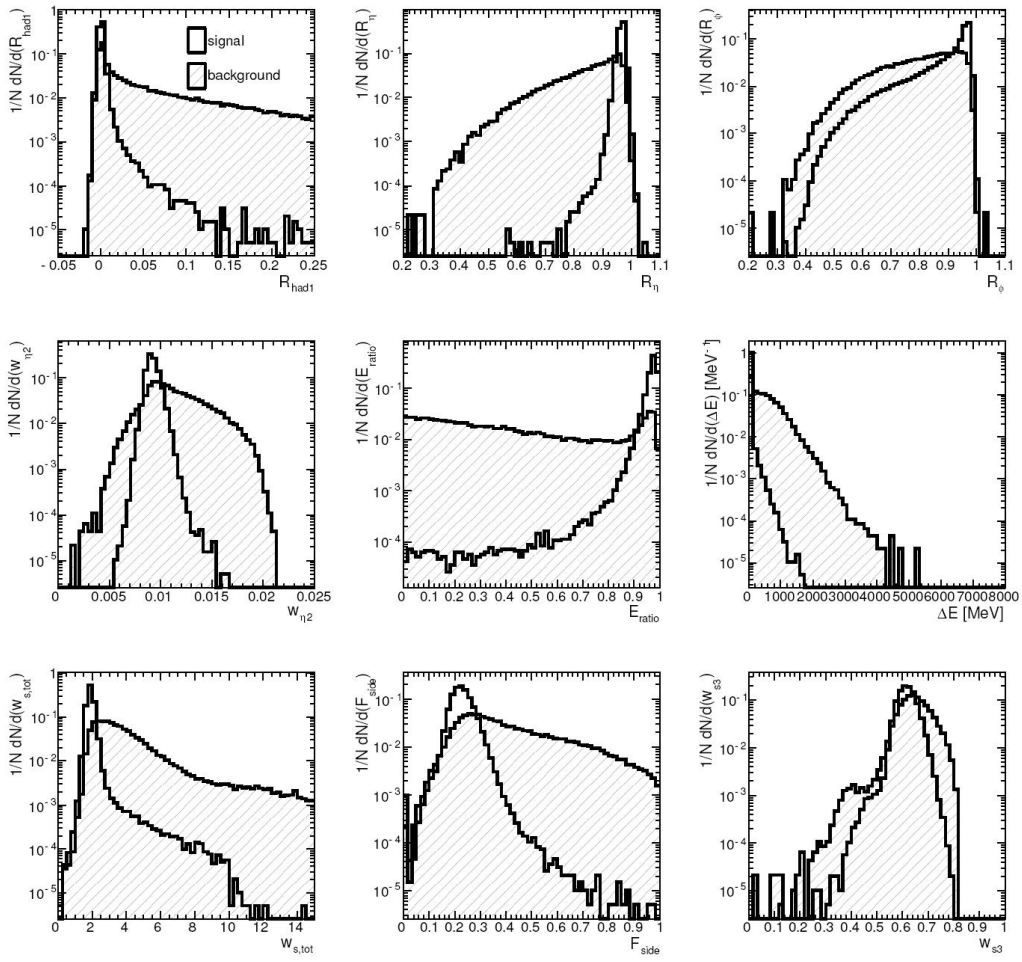

Figure 5.1: The signal and background for the inclusive photon analysis using 2010 ATLAS data. The same cuts were used for both the 2010 and 2011 analysis for the variables listed in this section.

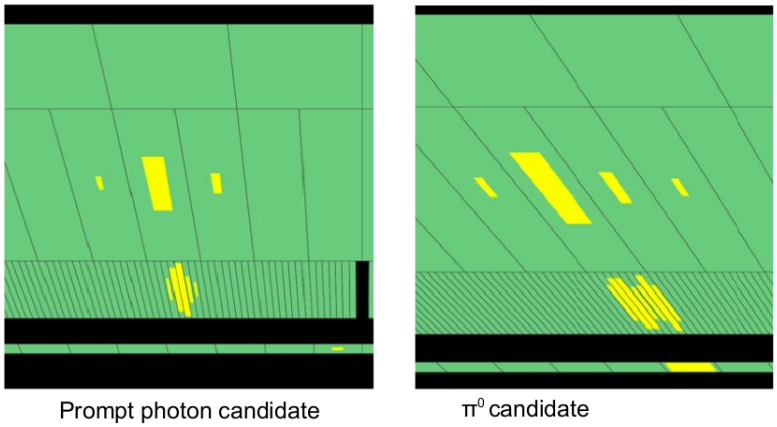

(a) γ (a) (b) π^0 (b)

Figure 5.2: Fig.(a) shows a clean signature for a photon candidate where in the strips there is one maximum in the strips and a narrow shower width in the second layer and is considered "tight". Fig.(b) is the signature for a π^0 where there are two maximum in the strip layer and a broader shape in layer two of the ECAL and is considered "loose" or "non-tight".

the lateral spread in η, by taking the fraction of energy outside of the core of three strips but within seven strips. ΔE tries to quantify the degree of which two peaks are present in the energy profile. This is done by finding the difference between the energy associated with the second maximum in the strip and the minimum energy between the maximum and the second maximum in the strip. E_{ratio} is the ratio between the difference in largest and second largest energy deposits over the combined energy of the largest and second largest energies.

The loose photon candidates are comprised of quantities based on shower shapes in the second sampling layer of the ECAL. The variables that define the loose photon candidates are: R_{had1}, R_{had}, R_{η}, and w_{η^2}. For the tight selection all of the shape variables are required to pass. The selection criteria does not depend on the photon candidate's E_T^{γ}, but do vary as a function of the photon reconstructed pseudorapidity. The η dependent selection takes into account the significant changes in the total thickness of the upstream material and variations

in the calorimeter geometry or granularity as a function of η.

Category	Name	Equation
Strip Variables	$w_{s\,3}$	$\sqrt{\frac{\Sigma E_i (i-i_{max})^2}{\Sigma E_i}}$
Strip Variables	$F_{\rm side}$	$\frac{E^{S1}_{7\times1} - E^{S1}_{3\times1}}{E^{S1}_{7\times1}}$
Strip Variables	ΔE	$[E^{S1}_{max2} - E^{S1}_{min}]$
Strip Variables	$E_{\rm ratio}$	$\frac{E^{S1}_{max1} - E^{S1}_{max2}}{E^{S1}_{max1} + E^{S1}_{max2}}$
Second ECAL layer	w_{η^2}	$\sqrt{\frac{\Sigma E_i \eta_i^2}{\Sigma E_i} - [\frac{\Sigma E_i \eta_i}{\Sigma E_i}]^2}$
Second ECAL layer	R_η	$\frac{E^{S2}_{3\times7}}{E^{S2}_{7\times7}}$
Second ECAL layer	R_ϕ	$\frac{E^{S2}_{3\times3}}{E^{S2}_{3\times7}}$

Table 5.1: A list of the variables that separate "tight" and "loose" selections. Where E is defined as the energy, $max1$ is defined as the maximum value, $max2$ is defined as the next maximum value, min is defined as the minimum, $S1$ is the first strip layer, $S2$ is the second layer of the ECAL, the subscript $x \times x$ is the window size that is used.

The "loose" selection criteria is the same for both converted and unconverted photons and is always tighter than the trigger requirements to avoid any trigger bias. The "tight" selection criteria differ for converted and unconverted photons. In addition to tightening the selection requirements on the quantities that the "loose" selection criteria are based on, they include additional quantities using primarily shower shapes in the first calorimeter sampling. The values of the selection requirements were optimized originally by using samples of simulated signal and background events prior to data taking. Once data was collected the selection requirements where reoptimized using data driven techniques. After the "tight" selection 1,219,045 photon candidates remain. Of these, 31728 photon candidates have reconstructed E_T^γ in the 800 GeV to 1 TeV bin. More details on

the discriminating variables used to define all of the selection criteria are provided in [20].

5.4 Photon preselection

Photon candidates with calibrated E_T^γ ([21]) above 100 GeV are retained for subsequent analysis. The energy resolution of the calorimeter is studied using $Z \to e^+e^-$ and $J/\psi \to e^+e^-$ decays [22]. It is found that the $Z \to e^+e^-$ mass peak is not well reproduced by the simulation, even after the application of energy scale corrections. The simulated mass distribution is well reproduced for $J/\psi \to e^+e^-$ decays with central electrons. The poor agreement for $Z \to e^+e^-$ mass resolution is attributed to the constant term in the resolution and corrections to the simulation are derived from data using $Z \to e^+e^-$ decays. This correction is then applied to the MC photons by rescaling their energy. In addition to the nominal corrected energy for each photon candidate, the rescaled energy also has an upper and lower correction that define the range of the corresponding systematic uncertainties on the prescribed energy scale.

To ensure a high purity and low fake rate, only photon candidates that satisfy the following quality criteria are used:

- The photon candidate has reconstructed $E_T^\gamma > 100$ GeV and pseudorapidity in the fiducial region of the first layer of the ECAL ($|\eta(\gamma)| < 1.37$ or $1.52 \leq |\eta(\gamma)| < 2.37$). The pseudorapidity region $1.37 < |\eta(\gamma)| < 1.52$ is excluded because it coincides with the barrel-endcap transition region for the electromagnetic calorimeter which makes its response less than optimal.

- The jet quality is defined as the fraction of LAr cells in the jet with a cell Q-factor greater than 4000. The cell Q-factor measures the difference between

the measured pulse shape (a_i^{meas}) and the predicted pulse shape (a_i^{pred}) that is used to reconstruct the cell energy. It is computed as $\sum_{samples}(a_i^{meas} - a_i^{pred})^2$. If the fraction of cells with Q-factor is greater than 4000, then the photon candidate is removed. If the photon candidate is not associated with a bad quality jet [23] inside a cone of $\Delta R = \sqrt{\Delta\phi^2 + \Delta\eta^2} = 0.4$ around the photon then that photon is retained.

- Photon Object Quality cuts are used to remove bad clusters that arise from detector problems such as dead high voltages in the ECAL cells that are non operational .

- Missing silicon B-layer hit (including a track that crosses a dead B-layer) is based on the absence of a hit in the B-layer when a hit was expected. This requirement has an efficiency for true photons of approximately 100%, while the fraction of electrons misidentified as a photon is reduced by about 1/3.

After the preselection, $\sim 5.1\%$ of photon candidates are rejected, while 2,666,325 candidates remain in the data sample. There are 133,316 fake photons.

5.5 Photon isolation energy

Isolation is an important observable for prompt photon studies and a depiction is shown in Fig. **5.3**. The prompt photon signal is expected to be more isolated from hadronic activity than the background. Also, because of the mixture of hard-scattering and fragmentation contributions in the prompt photon signal, it is important to have a well modeled isolation variable that can be linked to the parton level isolation cut used in NLO QCD computations. A robust isolation prescription [24] will help limit the non-perturbative fragmentation contribution,

which is poorly understood in theory while retaining the signal produced during the hard scatter.

For the study discussed here, the same isolation variable used in the previous ATLAS measurement [25] is used. Isolation is computed using calorimeter cells from both the ECAL and HCAL, in an annulus of radius 0.4 in the $\eta \times \phi$ space around the photon candidate, where the photon candidate is assumed to be in a 5×7 region in $\eta \times \phi$ space. The contributions from 5×7 ECAL cells in the $\eta \times \phi$ space around the photon barycenter are not included in the calculation. The small leakage from the photon outside this region, evaluated as a function of E_T^γ on simulated samples of single photons, is then subtracted from the isolation variable. The contribution to the E_T^γ from the underlying event (UE) and pileup is subtracted using active and passive jet areas described in more detail in [26] and [27]. The active area is defined as a dense area of overly soft particles, and the passive area is defined as a sparsely populated area with soft particles. To determine the average event-by-event correction, multiple active and passive jet areas are found for each event. This correction factor is then applied to remove UE events and pileup. For more details on the implementation see [28]. After these corrections, the $E_{\mathrm{T}}^{\mathrm{iso}}$ of simulated photons is independent of the photon E_T^γ. The signal is shown in Fig. **5.4** to be greater than background for a variety of E_T^γ. A residual mild dependence on in-time pileup is observed for this isolation variable. This is due to the inconsistent treatment of noise in the calculation of the uncorrected ("raw") isolation variable. This variable is computed from non-noise-subtracted calorimeter cells, and the pileup correction, is computed from the median "energy density" of soft jets created from (noise-suppressed) topological clusters. An alternative isolation variable ("topocluster isolation"), which uses topological clusters both in the calculation of the ("raw") isolation (using clusters within a annulus of radius 0.4) and for the pileup correction, was used in the

$H \rightarrow \gamma\gamma$ [29] search and in the measurement of the SM diphoton cross section [30]. The distributions of the standard cone isolation and of the topocluster isolation are compared in Fig. **5.5**. It can be seen that the topocluster isolation produces a narrower signal peak than the standard cone isolation. However, the isolation distributions of photon candidates failing the tight identification criteria, which are dominated by fake photons, are similar for the two isolation variables. As a consequence, the signal efficiencies and purities for an isolation selection at 7 GeV are expected to be similar when using the standard cone isolation variable or the topocluster isolation variable. In the following, the topocluster isolation is used only for verifying the nominal result (obtained with the standard cone isolation) and to assign a systematic uncertainty due to the isolation definition.

All photon candidates having reconstructed isolation transverse energies less than 7 GeV are considered experimentally "isolated". This definition has an efficiency which is identical to that of the parton-level isolation cut. The choice of 7 GeV for the value of the isolation requirement was chosen after optimizing the value that would provide the best compromise between good signal efficiency and high purity more details will be provided in Sect. 6.1.

After the photon identification requirements, 1,219,045 (616,807) photon candidates remain for the selection requirement $|\eta(\gamma)| < 1.37$ ($1.52 < |\eta(\gamma)| < 2.37$). After the final selection based on the isolation requirement and the background subtraction discussed in the next section, 1,044,611 ($|\eta(\gamma)| < 1.37$) and 481,581 ($1.52 < |\eta(\gamma)| < 2.37$) photon candidates were accepted for the cross section calculation. The fraction of converted photons is 32% (45%) in the central (forward) $\eta(\gamma)$ region. The total number of events with two photon candidates after the photon identification requirements is 1240.

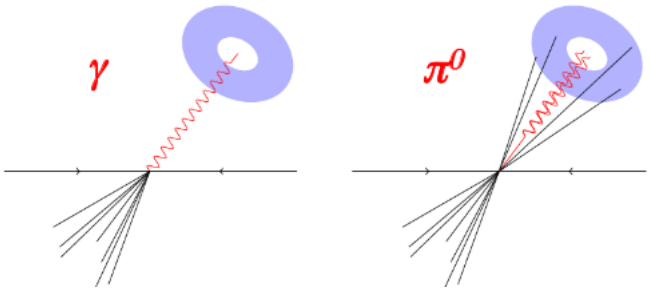

Figure 5.3: The isolation energy in the calorimeter. All of the calorimeter energy is summed in an annulus around the photon, where the central core is removed. This summed energy is defined as the isolation energy.

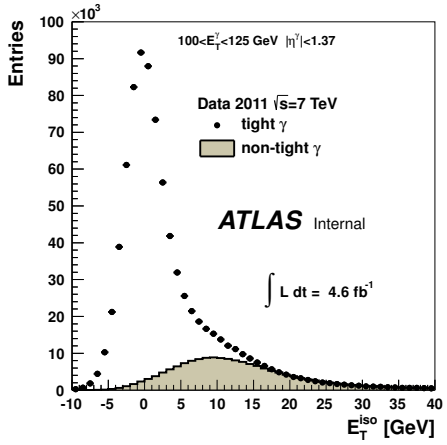

(a) $100 < E_T^\gamma < 125$ GeV

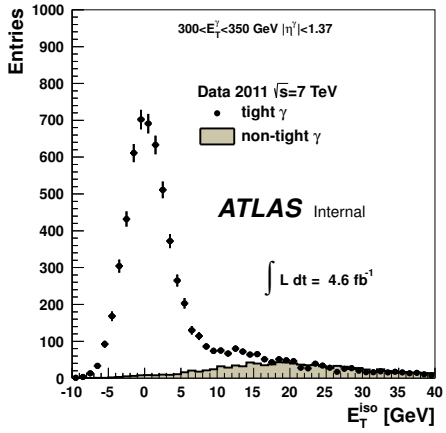

(b) $300 < E_T^\gamma < 350$ GeV

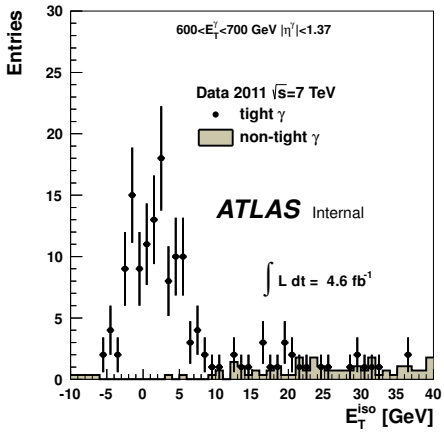

(c) $600 < E_T^\gamma < 700$ GeV

Figure 5.4: The distributions for the calorimetric isolation variable $E_{\mathrm{T}}^{(R<0.4)}$ in the central η region, after the leakage and density corrections, for tight (solid dots) and loose (shaded gray region) candidates. The latter is normalized to the former for $E_{\mathrm{T}}^{(R<0.4)} > 15$ GeV ("non-isolated region"). The excess of tight candidates over the normalized non-tight candidates for $E_{\mathrm{T}}^{(R<0.4)} < 15$ GeV ("isolated region") shows a clear peak for signal prompt photons.

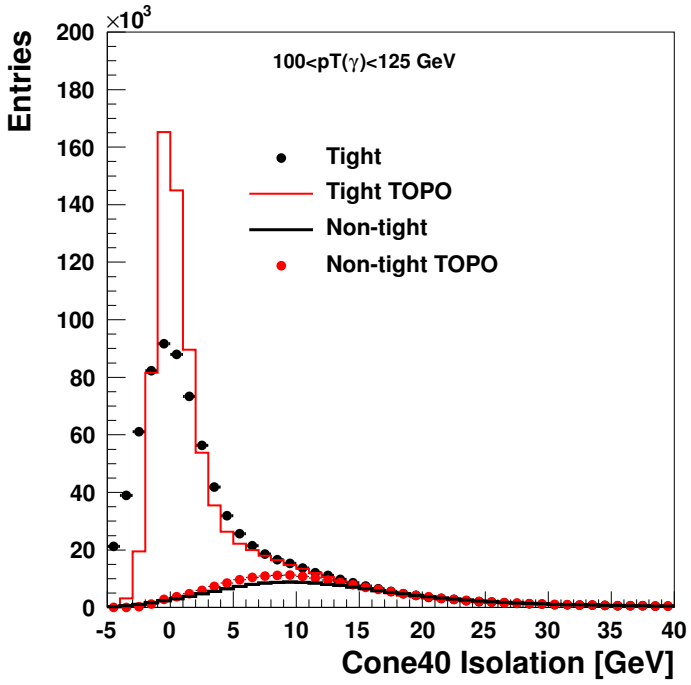

Figure 5.5: The distributions for the topocluster isolation variable $E_{\mathrm{T}}^{(R<0.4)}$ versus the standard (cluster) isolation, after the leakage and density corrections, for tight and non-tight candidates. The latter is normalized to the former for $E_{\mathrm{T}}^{(R<0.4)} > 15$ GeV ("non-isolated region"). The red color is used to show the topocluster isolation, while black shows the standard (cluster) isolation. Despite the differences seen the amount of data under the curves is similar.

Chapter 6

Background Estimation and Signal Extraction

In order to model the energy flow inside jets and the fragmentation to π^0's, data-driven techniques are used to extract the background isolation distribution because the simulation does not model well the background isolation. This requires the selection of an unbiased background-enhanced sample of photon candidates. In this chapter the 2D-sideband method will be discussed.

6.1 Background Estimation

A study was performed to understand the distribution of photons in the azimuthal angle and to search for possible reconstruction problems. Fig. **6.1** shows the ϕ^γ distributions of the photon candidates in the signal region for the barrel and endcap regions separately, before any luminosity corrections are applied. The distributions are for $E_T^\gamma > 100$ GeV and are flat as expected. The number of signal events is less than data because the data contains contamination from background, which is not corrected at this point. The ϕ distribution was also studied in the region between $500 < E_T^\gamma < 600$ GeV; see Fig. **6.2**. No statistically significant deviation from a flat distribution was observed, indicating the good quality of the photon reconstruction at high energies.

The reconstructed photons contain background that must be removed. Two methods were used to remove background; one method uses isolation variables, and the other method subtracts the background.

The main background to prompt photons is due to QCD jets containing π^0s that carry most of the jet energy. These π^0s then decay to photon pairs that

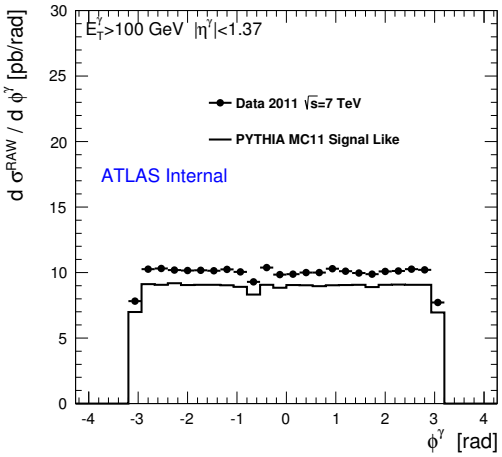

(a) ϕ distribution in barrel region

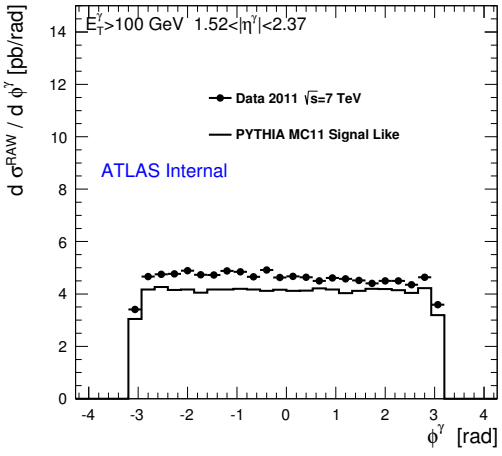

(b) ϕ in end cap region

Figure 6.1: ϕ distributions for photon candidates before efficiency corrections for both the barrel (a) and endcap (b) regions. The uncorrected data are compared to the signal MC in the signal region.

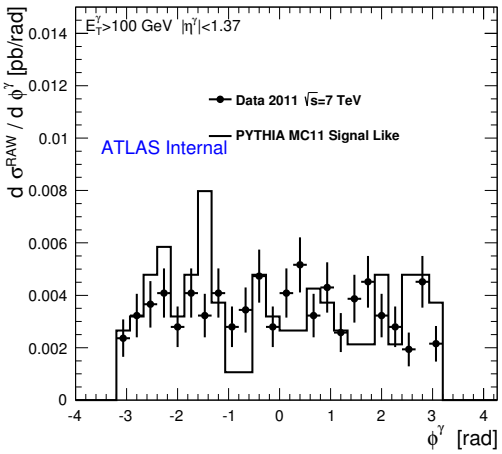

Figure 6.2: ϕ distribution for $500 < E_T^\gamma < 600$ GeV for photon candidates before data corrections. The uncorrected data are compared to the signal MC in the signal region.

deposit energy in the ECAL. Background photons (fake photons) from jets are expected to be less isolated than prompt photons due to the nearby activity from the other particles in the jet. The isolation energy $E_{\mathrm{T}}^{(R<0.4)}$ therefore provides discrimination between prompt photons and fake photons from jets. Isolation requirements are designed to be highly efficient for signal events and to reject fake photons such as $\pi^0 \to \gamma\gamma$ and fragmentation photons. The isolation requirements are applied using the isolation energy.

The choice for the optimal isolation parameter is found by determining the isolation energy value which provides the best signal purity, reconstruction and identification purity and efficiency. The signal purity is calculated using both data and MC and is defined as:

$$\text{signal purity} = \frac{N - N(\text{subtracted})}{N} \qquad (\mathbf{6.1})$$

where N is the number of signal reconstructed events in data, and N(subtracted) is the number of subtracted photons using the background subtraction method (which includes a correction from the MC simulation), which will be discussed later in this section. The efficiency is defined as the ratio of the number of reconstructed signal photons, to the number of true photons (see Chapter 7). The purity and efficiency as a function of p_T are shown in Fig. **6.3**.

There are two isolation variables that where explored: one was the cone size that is used in defining the isolation, and the other was the isolation energy. The most common cone size used in ATLAS is R=0.4, so this is what is used in this analysis. Using a constant cone size of R= 0.4, different transverse isolation energies are chosen to allow the purities and efficiencies to be directly compared. In Fig. **6.3**, the different isolation energies that were studied are plotted for both purity and efficiency. For a transverse isolation energy of $E_{\mathrm{T}}^{(R<0.4)} < 5$ GeV, the

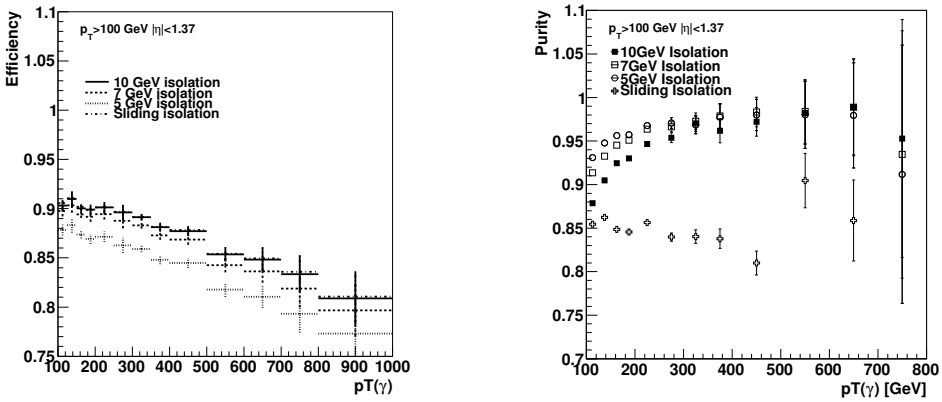

(a) Efficiency for $p_T(\gamma)$

(b) Purity for $p_T(\gamma)$

Figure 6.3: (a) The efficiency and (b) the purity as a function of the photon p_T for all of the isolation energies studied.

purity is on average 0.95 with an efficiency is 0.88. The purity is 0.94 and the efficiency is 0.90 for a transverse isolation energy of $E_{\mathrm{T}}^{(R<0.4)} < 7$ GeV. For a transverse isolation energy of $E_{\mathrm{T}}^{(R<0.4)} < 10$ GeV, the purity on average is 0.92 and the efficiency is 0.91. For the last isolation parameter, instead of using a fixed transverse energy requirement, a sliding isolation parameter is used. The sliding isolation requires that at least 90% of the photon energy is isolated. This means that as the photon p_T increases, a larger isolation energy is allowed, i.e $\frac{p_T}{(p_T+iso)} \leq 90\%$, where iso is defined as the isolated p_T. From the plots, it can be seen that the optimal choice for both high efficiency and purity occurs for a transverse isolation energy of $E_{\mathrm{T}}^{(R<0.4)} < 7$ GeV.

The uncertainties on the purity and efficiency are added in quadrature, taking into account the correlation between variables. As can be seen in Fig. **6.3**, as the photon p_T increases, the purity value within the uncertainty can become larger

than one. Typically for purity measurements binomial errors are used. For this analysis binomial errors were not used at high p_T because the data samples were statistically limited. At high p_T the MC is needed in order to make a purity measurement. Since the two sets of data are independent, binomial errors could not be used. The purity as a function of E_{T}^{γ} is shown in Fig. **6.4(a)** and plateaus at approximately 0.96. The purity as a function of $|\eta|$ is shown in Fig. **6.4(b)**, and is approximately 0.93.

6.2 Signal Extraction

A second method to remove background is to use a subtraction technique, the technique used in this analysis is the"two-dimensional sidebands" method [24], shown in Fig. **6.5**. This method does not require precise knowledge of the signal. The background properties are deduced from the observed data. It is based on the definition of a "tight-isolated" signal region A and three background control regions B, C, D: "tight-non isolated", "non tight-isolated" and "non tight-non isolated", respectively. The basic method assumes that the control regions have negligible signal contamination and that the background shape is uncorrelated across the three regions: the method can be easily extended in case the previous assumptions are not completely satisfied. The isolation definition uses $E_{\mathrm{T}}^{(R<0.4)}$ which was discussed previously.

The "loose" and "tight" photons are defined using the shower shape variables. The shower shape variables used are: w_{stot}, $w_{s\,3}$, F_{side}, ΔE, and E_{ratio}, described in chapter 5.

A background-enhanced sample is provided by requiring that some of the

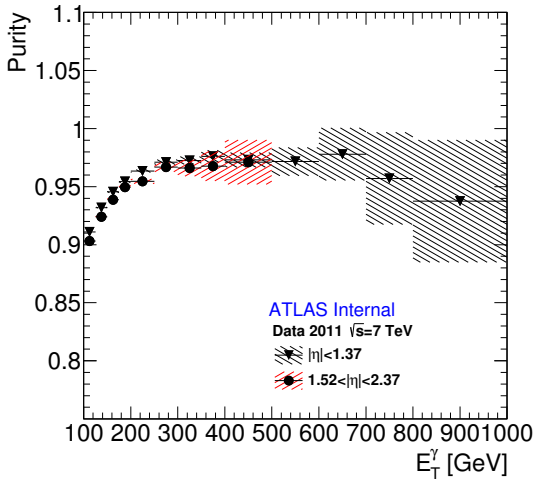

(a) Purity for E_{T}^{γ}

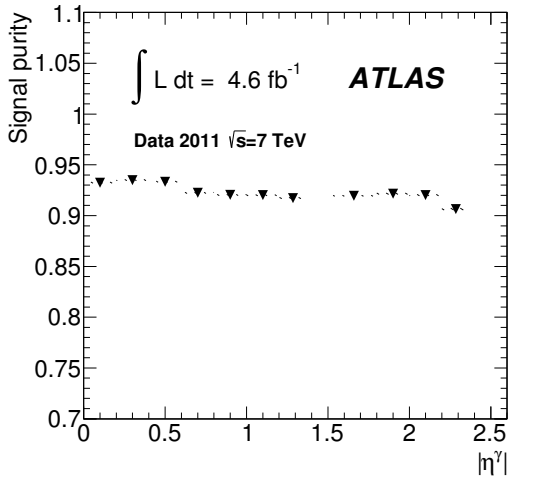

(b) Purity for $|\eta(\gamma)|$

Figure 6.4: The prompt photon ("signal") purity as a function of E_{T}^{γ} and $|\eta(\gamma)|$ determined from the data using the the two-dimensional sidebands method (which also includes a correction from the MC). The uncertainties on the $|\eta(\gamma)|$ plot (b) are too small to be seen because of the large statistics.

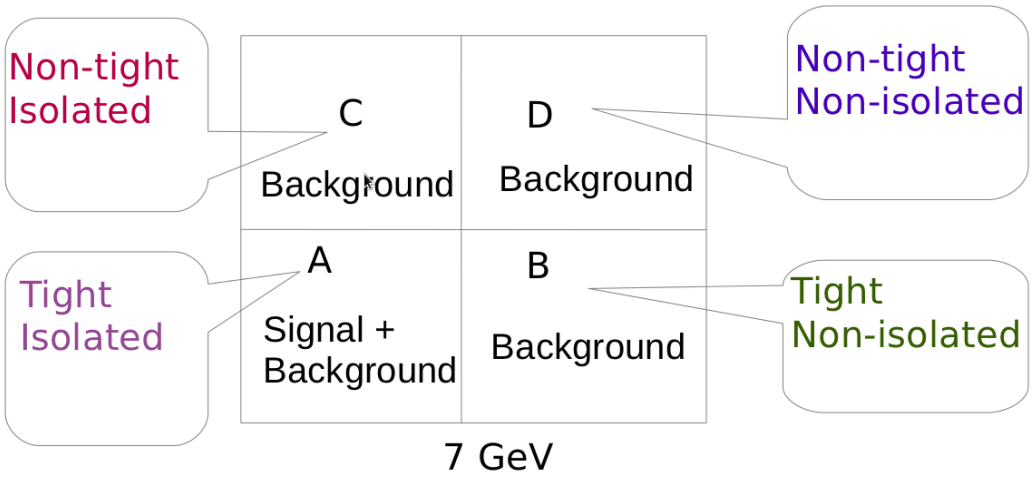

Figure 6.5: An illustration of the 2D-sideband method. The isolation is defined on the horizontal axis. The "tightness" is defined on the vertical axis. Where the signal region is in region A and is the isolated tight region.

shower shape variables pass but not all of them. The variable choice is slightly arbitrary, but not being correlated to the isolation variable and providing large statistics are good choices to provide a good background-enhanced sample. Of all the shower shape variables, four variables where chosen to produce background enhanced samples: $w_{s\,3}$, F_{side}, ΔE, and E_{ratio}. Such photons will be called "non-tight candidates" or "loose candidates", while the photon candidates satisfying the full "tight" selection will be called "tight candidates".

Fig. **6.6** shows the distribution of $E_{\text{T}}^{(R<0.4)}$ for tight and non-tight candidates. The latter is normalized to the former in the "non-isolated" region $E_{\text{T}}^{(R<0.4)} >$ 15 GeV. The agreement between the two shapes in the non-isolated region reinforces the two assumptions: that a good background estimation can be obtained from the non-tight sample, and that the non-isolated region is fairly free of signal. The excess of tight candidates over the normalized non-tight candidates in the "isolated" region $E_{\text{T}}^{(R<0.4)} < 15$ GeV shows a clear peak for signal prompt photons. Fig. **6.7** shows the same distribution but in a few bins of E_{T}^{γ}. This figure

also shows the $E_{\mathrm{T}}^{(R<0.4)}$ distributions after the subtraction of the normalized non tight candidates from the tight candidates. It compares two different E_T regions for the end cap region. No E_T dependence on the shapes is observed.

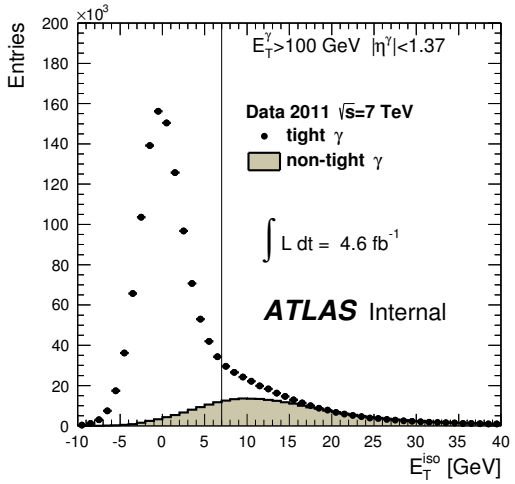

Figure 6.6: The distributions for the calorimetric isolation variable $E_{\mathrm{T}}^{(R<0.4)}$, for tight (solid dots) and non-tight (shaded region) candidates. The latter is normalized to the former for $E_{\mathrm{T}}^{(R<0.4)} > 15$ GeV ("non-isolated region"). The vertical line indicates the final selection cut (7 GeV) used for the final cross sections. The excess of tight candidates over the normalized non-tight candidates for $E_{\mathrm{T}}^{(R<0.4)} < 7$ GeV ("isolated region") proves the evidence of a signal.

Fig. **6.8** shows the E_{T}^{γ} distributions of photon candidates with an isolation energy of $E_{\mathrm{T}}^{(R<0.4)} < 7$ GeV in the signal region A and photons in the background control region D with an isolation energy of $E_{\mathrm{T}}^{(R<0.4)} > 7$ GeV, for signal and background PYTHIA MC events. The distributions are normalized to the expected luminosity and each bin is divided by the bin width. This figure shows that the signal region A is indeed dominated by signal, whereas the background control region D is dominated by background.

Fig. **6.9(a)** shows the data in region A for the barrel region and before the corrections and background subtraction are applied, compared to the signal MC. This comparison indicates that the MC is below the data at low E_T^{γ} which can

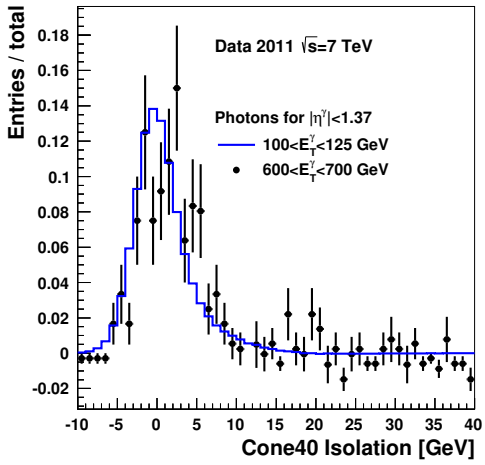

Figure 6.7: $E_{\mathrm{T}}^{(R<0.4)}$ distributions of tight photons in the forward region, after subtracting the normalized non-tight distribution, for two different E_{T}^{γ} bins.

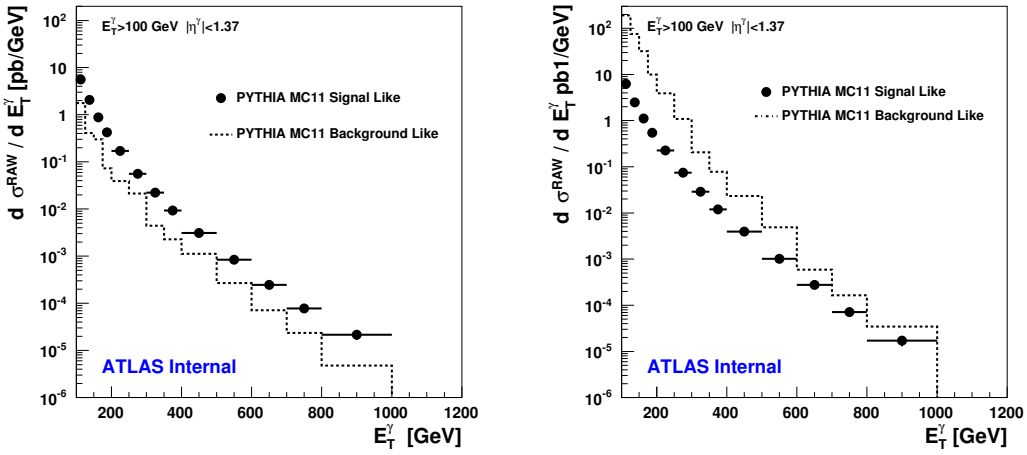

(a) E_T^{γ} in region A

(b) E_T^{γ} in region D

Figure 6.8: E_{T}^{γ} event distributions for signal MC and background MC before the detector corrections are applied. Figure (a) is for the signal like region, region A. Figure (b) is for the background region, region D.

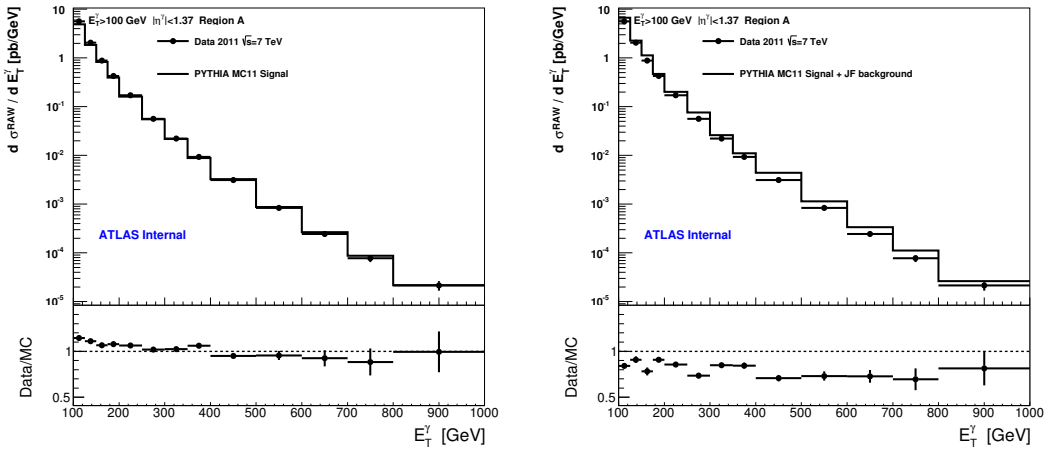

(a) E_T^γ in region A (b) E_T^γ in region A ALL MC

Figure 6.9: E_{T}^{γ} event distributions for data before the detector correction applied. The uncorrected data are compared to the signal MC in the region A for (a), (b) compares the same data as (a) but the MC combines signal+background MC.

be explained by the presence of background in the data. Fig. **6.9(b)** compares the data, with no correction or subtraction applied, to the signal MC plus the background MC. One can see that such MC overestimates uncorrected data. Note that this effect can correspond to different background fractions in data than in MC, which has to be subtracted using the data-driven sidebands method.

We investigate three different techniques to estimate the residual background in the signal region A, based on the number N^k of events observed in each of the four regions $k = A$, B, C, and D of the two-dimensional plane. In some of the techniques, the number of N_{SIG}^k signal events and N_{BKG}^k background events expected from the simulation are also used.

The "uncorrelated" method assumes that there is no signal contamination in the background control regions $k = B$, C, and D, and that the isolation and identification variables are uncorrelated for background events, i.e. the isolation distribution for background events is the same for tight and non tight candidates.

This leads to the relation:

$$N_S^A = N^A - N^C \frac{N^B}{N^D} \tag{6.2}$$

The "correlated" method takes the signal contamination into account by subtracting the signal contribution in each background region, therefore replacing N^k (where $k = B$, C, and D) with $N^k - C_k N_{SIG}^A$, where $C_K = \frac{N_{SIG}^k}{N_{SIG}^A}$ is calculated from the MC.

$$N_S^A = N^A - \frac{(N^B - C_B N_{SIG}^A)(N^C - C_C N_{SIG}^A)}{(N^D - C_D N_{SIG}^A)} \tag{6.3}$$

The "modified correlated" method takes into account that there is signal in the background control regions, and in addition takes into account possible correlations between the isolation and identification variables for background events:

$$N_S^A = N^A - \left(\frac{N^B N^C}{N^D}\right)\left(\frac{N_{BKG}^B N_{BKG}^C}{N_{BKG}^D}\right)\frac{N_{BKG}^D + C_D N_{SIG}^A}{(N_{BKG}^B + C_B N_{SIG}^A)(N_{BKG}^C + C_C N_{SIG}^A)} \tag{6.4}$$

Fig. **6.10** shows the ratio of the modified correlated method to the correlated method, and the ratio of the uncorrelated method to the correlated method. This shows that the subtraction methods are within approximately 1% of each other. The correlated method was chosen to obtain the nominal results, while the alternative results obtained with the uncorrelated and modified correlated methods contribute to the systematic uncertainties.

Fig. **6.4(a)** shows the prompt photon purity in the signal region A, as a function of E_T^γ using the uncorrelated approach. Fig. **6.11** shows the purity for the correlated approach. The measured purity is always larger than 90% and increases to over 95% for $E_T^\gamma > 200$ GeV. Fig. **6.4(b)** shows the prompt photon purity in

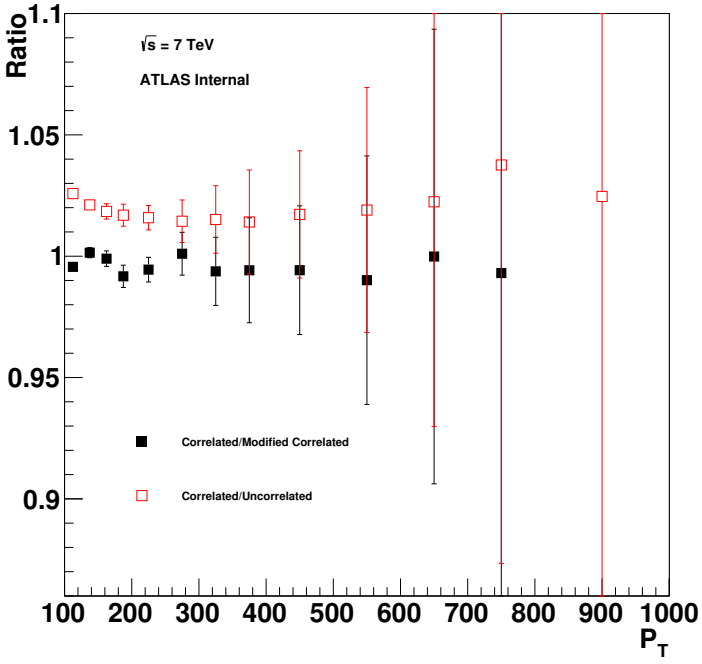

Figure 6.10: The comparisons of the signal purities using several subtraction methods as a function of p_T: the uncorrelated method divided by the correlated method, and the modified correlated method divided by the correlated method. The purities where calculated using data and the sideband subtraction method.

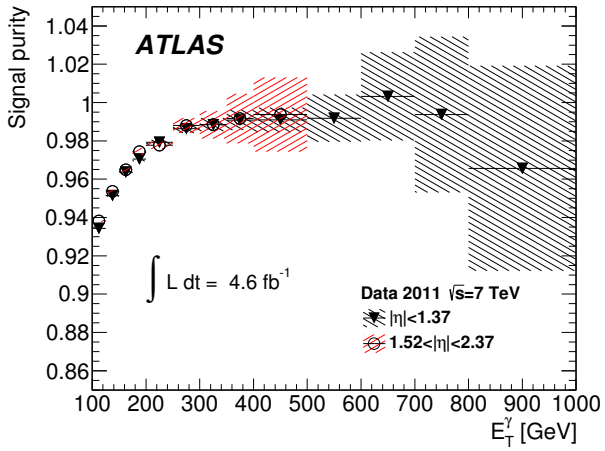

Figure 6.11: The signal purity for the barrel and endcap η^γ regions estimated from the data using the two-dimensional side band approach shown in Eq. (**6.3**). The shaded bands indicate statistical uncertainty.

the signal region A as a function of $|\eta|$, and it is always greater then 90%. The purity values are largely determined by the photon identification since the bin size is a factor 6-7 larger than the photon resolution; therefore bin-by-bin migration effects are negligible. In Fig. **6.4(a)** the purity in the 500-600 GeV bin is identical to the purity in the 400-500 GeV bin. Due to limited statistics, it was impossible to determine the purity in the 500-600 GeV bin accurately. Therefore the purity for the 500-600 GeV bin was assumed to be identical to the 400-500 GeV bin.

6.3 Previous Results

The present measurement extends the previous ATLAS publication [25], that used 35 pb^{-1} of integrated luminosity, to a larger transverse energy (E_{T}^{γ}). The previous ATLAS results measured the cross section to 400 GeV in four different η regions. The measurement found good agreement between the NLO results for the barrel region for all p_T bins. In the forward region, there is good agreement at the lower p_T bins, however as the p_T increases the agreement between the NLO and data deviate. CMS [31] has extended the inclusive photon cross section to 400 GeV in E_T in four η regions. CMS found better agreement for $|\eta| < 0.9$ and $1.57 < |\eta| < 2.1$ to the NLO results than in the other η regions. A similar measurement has been performed by the D0 Collaboration [32], and the CDF Collaboration [33]. Measurements of the inclusive isolated prompt-photon cross section at the Tevatron, in $p\bar{p}$ collision at a centre-of-mass energy $\sqrt{s} = 1.96$ TeV, are reported in Refs. [32, 33]. The measurement by the D0 Collaboration [32] is based on 326 pb^{-1} and covers a pseudorapidity range of $|\eta(\gamma)| < 0.9$ and a transverse energy range of $23 < E_{\mathrm{T}}^{\gamma} < 300$ GeV, while the measurement by the CDF Collaboration [33] is based on 2.5 fb^{-1} and covers a pseudorapidity range of $|\eta^{\gamma}| < 1.0$ and a transverse energy range of $30 < E_{\mathrm{T}}^{\gamma} < 400$ GeV. Both D0

and CDF measure an isolated prompt-photon cross section in agreement with next-to-leading order (NLO) perturbative QCD calculations. The analysis that is presented in this dissertation extends the cross section to 1 TeV in two η regions. It also compares data with two LO MCs and a NLO calculation by comparing the differential cross sections $\frac{d\sigma}{E_T^\gamma}$ and $\frac{d\sigma}{\eta^\gamma}$.

Chapter 7

Efficiency and Systematic Uncertainty

7.1 Introduction

In this chapter the efficiency as well as the systematic uncertainties are discussed. The efficiencies that are described below include the photon reconstruction and selection efficiency, trigger efficiency, and identification efficiency. The correction factor variable takes into account all systematic uncertainties as well as the efficiencies and acceptances. The correction factors also take into account the photon resolution and are used to unfold the cross section. The systematic uncertainties that are listed for photons include: energy scale, reconstruction efficiency, identification efficiency, choice of MC generator, different background subtraction techniques, isolation selection definition and energy resolution.

7.2 Efficiency

The differential cross section for the production of isolated prompt photons in a given phase space bin i is

$$\frac{N_i}{C_i(\gamma) \cdot \Delta_i \cdot \int L\mathrm{dt}}, \tag{7.1}$$

where N_i is the number of photons in bin i after background subtraction, $C_i(\gamma)$ is a correction factor to be discussed below, Δ_i is the width of bin i and $\int L\mathrm{dt}$ is the integrated luminosity. The correction factor, $C_i(\gamma)$, is evaluated from the bin-by-bin ratio of the reconstructed and the generated particle-level prompt photons in the signal simulation.

$$C_i(\gamma) = \frac{N_i(reco)}{N_i(gen)}. \quad (\mathbf{7.2})$$

The correction factor $C_i(\gamma)$ accounts for the photon reconstruction and selection efficiency as well as the event selection efficiency and identification efficiency as well as resolution. These efficiencies are discussed in more detail below:

- **Photon reconstruction and selection efficiency.** This is the efficiency for a simulated photon, within the acceptance of the differential cross section measurement, to be reconstructed as a photon passing all the selection criteria outlined in Section 7.3. The largest contributing factor to this efficiency is the selection isolation requirement $E_{\mathrm{T}}^{\mathrm{iso}} < 7$ GeV. This efficiency was determined by using MC simulated signal events after correcting the simulated calorimeter shower-shapes to match those observed in data [34]. The shower-shape corrections for the MC simulation were determined from a comparison of data with the simulation in the control samples of photons selected in the same kinematic regions as used in this measurement. The average value of this efficiency was found to be 95%.

- **Trigger efficiency.** This efficiency deals with the trigger efficiency which is defined as the efficiency for an event to pass through a photon trigger with a transverse energy threshold of 80 GeV. The trigger efficiency is determined using a data-driven technique based on low-E_{T}^{γ} threshold high-level triggers, and is measured to be 100^{+0}_{-3}% for $E_T^{\gamma} > 100$ GeV [2]. The trigger efficiency as a function of photon p_T is shown in Fig. **3.8**.

- **Identification efficiency.** This efficiency deals with the "tight" definition of the signal prompt photon as well as the amount of material upstream of the calorimeter. It was calculated by taking simulated MC events and cor-

recting the shape variables to match those in data. The amount of material that is in the simulated model of the detector is varied as well.

Unlike the correction factor shown in Eq (**7.2**), the photon selection and reconstruction efficiency is calculated using the simulated signal samples as the ratio of events passing all selection criteria to the number of generated ("truth") events, after matching reconstructed photons with the truth photons:

$$e_{p_T BIN} = \frac{N(reco \oplus gen)}{N(gen)}, \tag{7.3}$$

where $N(gen)$ is the number of generated truth particles in the same p_T bin where $N(reco \oplus gen)$ is reconstructed. $N(reco \oplus gen)$ is all of the reconstructed photons that are matched to generated photons. Both numbers, $N(reco \oplus gen)$ and $N(gen)$, are computed from the PYTHIA signal samples: $N(reco \oplus gen)$ is the number of events in region "A", defined in Chapter 6, after the selection and $N(gen)$ is the number of events passing the truth-level E_{T}, η, and the photon isolation selections.

The choice of the truth-level $N(gen)$ is important because it describes the same efficiency correction factor that corrects for pileup contributions, discussed in Chapter 6. Ideally the final comparison would be with the theory prediction which does not account for pileup. However, for simplicity pileup effects were not removed from data, they were applied to the theory predictions. The isolation selection also contributes to the value of $N(gen)$ which is constructed with all truth particles (excluding muons and neutrinos) with jet area corrections applied [35]. Thus it has a reduced sensitivity to pileup. The effects of pileup and hadronization are discussed in the Sect. 3.1. Bin by bin migrations are handled by a migration purity factor, $p = N(reco \oplus gen)/N(rec)$ and the correction factor, which is $e_{p_T BIN}/p = N(rec)/N(gen)$.

In addition to the efficiencies quoted above, the correction factor includes the reconstruction and identification purity of photons, as well as the possible migration purity originating from bin-by-bin migration due to the finite bin sizes. The migration purity should not be confused with the signal direct-photon purity discussed in 6. The MC simulations indicate that the energy resolution of photons in the range $100 < E_{\mathrm{T}}^{\gamma} < 600$ GeV is approximately 3% in the central region and approximately 4% in the end-cap region. The widths of the bins in E_T, for the differential cross section measurement are chosen to keep the migration between neighboring E_{T}^{γ} bins below 0.5%. The signal direct-photon purity discussed in Sect. 6 does not contribute to the correction factor calculated from the signal MC samples.

Typical corrections from the PYTHIA, and HERWIG MC signal events are shown in Figure **7.1**. The corrections determined using HERWIG agree with the corrections determined from PYTHIA to within 10%.

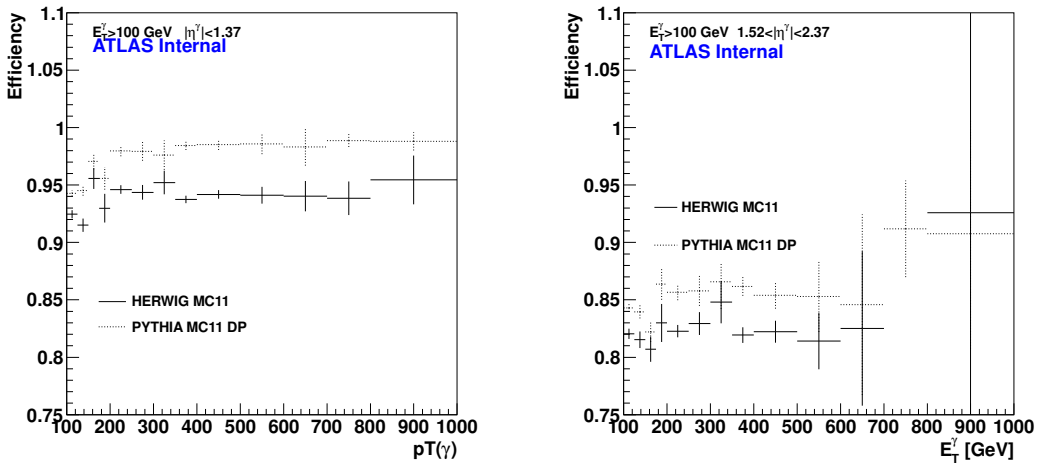

(a) $|\eta(\gamma)| < 1.37$ (b) $1.52 < |\eta(\gamma)| < 2.37$

Figure 7.1: The efficiency from the PYTHIA MC signal sample and the HERWIG MC signal sample for different $\eta(\gamma)$ regions (left: barrel; right: end-cap).

Figure **7.2** shows the bin-by-bin correction factors as a function of photon p_T for $|\eta| < 1.37$ and $1.52 < |\eta| < 2.37$ regions. The shaded band represents both statistical and systematic uncertainties which will be discussed in Sect. 7.4. Figure **7.3** shows the correction factors as a function of $|\eta^\gamma|$.

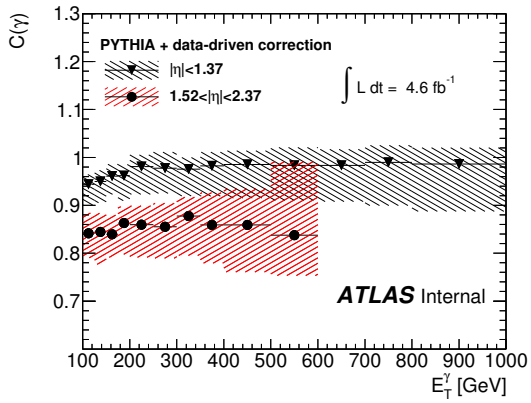

Figure 7.2: The correction factors as a function of E_T^γ used in this analysis. The shaded bands indicate the systematic uncertainties discussed in Sect. 7.4.

7.3 Cross Section

The average differential cross section for the production of isolated prompt photons in a certain bin i of (true) $E_{\rm T}$ (integrated over one true $|\eta|$ bin k) is:

$$\left\langle \frac{d\sigma_i^{\rm isol,k}}{dE_{\rm T}^{\rm true}} \right\rangle = \frac{1}{\int Ldt} \frac{N_i^{\gamma,{\rm sel,isol},k}}{C_i(\gamma)\Delta E_{{\rm T},i}^{\rm reco}} \qquad (7.4)$$

$N_i^{\gamma,{\rm sel,isol},k}$ is the number of prompt photons in the selected sample after correcting for the signal direct-purity measurement described in Chapter 6, whose width is $\Delta E_{{\rm T},i}^{\rm reco}$. $\int Ldt = (4.64 \pm 0.085)$ fb^{-1} is the integrated luminosity of the sample under study. $C_i(\gamma)$ is the correction factor given in Eq. **7.2**. As previously mentioned the correction factors also takes into account possible bin-by-bin migration

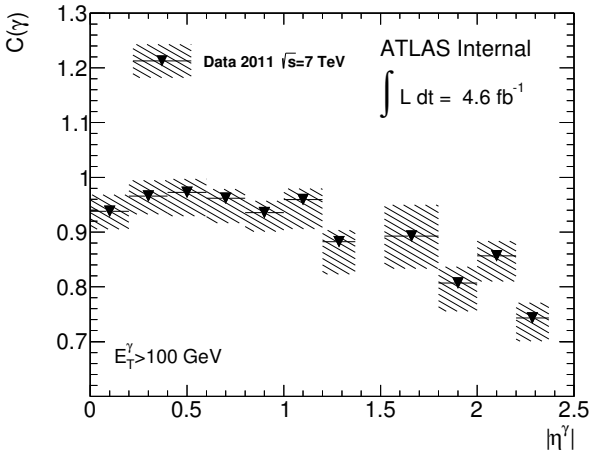

Figure 7.3: The correction factors for $E_{\mathrm{T}}^{\gamma} > 100$ GeV as a function of $|\eta^{\gamma}|$. The shaded area shows the statistical and systematic uncertainties. The low-efficiency region $1.37 < |\eta^{\gamma}| < 1.52$ is excluded from the measurement.

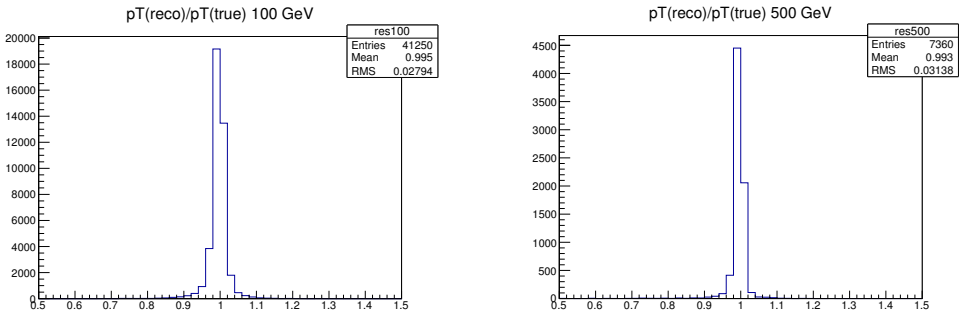

(a) $E_T^{\gamma} > 100$ GeV for barrel region (b) $E_T^{\gamma} > 500$ GeV for the barrel region

Figure 7.4: Resolution for $E_T^{\gamma} > 100$ GeV (a) and 500 GeV (b)

effects.

The photon resolution was studied in order to optimize the bin size. To estimate the resolution, tight reconstructed photons were matched with the truth-level photons (after the isolation requirement) in the MC simulation. The resolutions for the barrel and forward regions were found to be small and behaved as expected. The resolution of the barrel region for two p_T bins is shown in Fig. **7.4**.

This analysis uses a bin size which are a factor 5-6 larger than the resolution in each bin, thus the effect of the migration is below 0.1%. The migration effects

are automatically included in the bin-by-bin correction factor used in this study.

The systematic uncertainties originating from the estimation of the number of signal events from the two-dimensional sideband subtraction, described in Chapter 6 and the event selection and trigger efficiency are described in Sect. 7.4. In this analysis, migration effects are negligible since the bin sizes for the cross section measurements are typically a factor 7-8 larger than the photon resolution.

7.4 Systematic Uncertainties

The systematic uncertainties on the measured differential cross sections are determined by varying the selection criteria or the analysis procedure and repeating the analysis. The systematic variations affect both the $C_i(\gamma)$ and signal purity, thus leading to the overall change in the cross section. The largest uncertainties are described below:

- **Uncertainty on the photon reconstruction efficiency due to the isolation selection.** (`PYTHIA` **MC11 Iso**$\pm\delta$) A typical shift between the true and reconstructed isolation in the MC simulation was found to be less than 700 MeV. This difference does not depend on E_{T}^{γ}, is similar between `PYTHIA` and `HERWIG` signal and background MC samples, and does not depend on MC samples with alternative detector geometry. This means that the amount of material in `GEANT` can be varied. This difference is also similar to that observed between data and the MC simulation (see Fig. **6.6** and the discussion in Sect. 6), and is consistent with the previous publication [25] estimated using electrons. We use a $\pm$700 MeV variation for the isolation selection which covers the differences discussed above.

  The systematic uncertainty on the cross section due to the choice of isolation

requirement was determined by changing the selection by ±700 MeV in the simulation and recalculating the correction factors $C_i(\gamma)$. This systematic variation leads to a typical uncertainty below 2% for all E_{T}^{γ} explored in this measurement.

- **Uncertainty on the cross section due to insufficient knowledge of the photon identification efficiency. (Identification)** This uncertainty is calculated by using different techniques for the photon identification as described in Ref. [34]. Such uncertainties include a number of systematic effects, including sources of uncertainty on the amount of material upstream of the calorimeter and on the definition of "tightness". An effect of 3% or less for all E_{T}^{γ} explored in this measurement is observed.

- **Uncertainty due to photon energy measurement. (Energy Scale)** This is calculated by varying the photon energy scale within the expected uncertainty in the MC simulation. This uncertainty mostly affects the $C_i(\gamma)$. The effect of such a variation leads to an uncertainty between 2% at low E_{T}^{γ} and 6% at large E_T^{γ}.

- **Uncertainty on the $C_i(\gamma)$ due to the choice of the MC generator. (`HERWIG MC11`)** This is computed by considering `HERWIG` for the bin-by-bin correction instead of `PYTHIA`. This uncertainty affects both the photon reconstruction and identification. It also probes the uncertainty on the signal reconstruction due to alternative fragmentation mechanism. This uncertainty ranges from 2% at low E_T^{γ} to 5% at $E_T^{\gamma} > 800$ GeV.

- **Uncertainty on the background subtraction. (Background Subtraction)** It is assessed using alternate background subtraction techniques discussed in Chapter 6. Eq. (**6.3**) is modified to neglect signal leakage. The

background is subtracted by either neglecting correlations between the signal and background regions, or by using the central values of the correlations calculated from simulated background events. This uncertainty on the cross section varies between 3% and 4% for all E_{T}^{γ} explored in this measurement.

- **Uncertainty arising from the definition of the isolation selection [36]. (Isolation Selection)** This uncertainty was determined by repeating the measurement using an alternative definition of the non-isolated region by increasing the isolation requirement from 7 to 10 GeV. This change affects both the signal purity and the correction factor $C_i(\gamma)$. An effect of 1% or less for all E_{T}^{γ} explored in this measurement is observed, which is compatible with the statistical uncertainty.

- **The systematic uncertainty on the cross section due to the photon energy resolution. (Energy Resolution)** This is determined by calculating the nominal resolution and its uncertainty using a known decay such as $Z \rightarrow e^{+}e^{-}$. Unfolding the cross section within the resolution's uncertainty provides the systematic uncertainty on the cross section due to the photon energy resolution. This uncertainty effects both the reconstructed energy in the MC simulations, which is used for the background subtraction and $C_i(\gamma)$. This uncertainty is typically 1% for all E_{T}^{γ} explored in this measurement.

- The correction factor was recalculated using PYTHIA signal samples with 50% less photons coming from fragmentation. This uncertainty was assumed to be symmetrical and has a small effect ($< 0.5\%$).(Fragmentation)

- The integrated luminosity is calculated during runs by measuring interaction rates using several ATLAS devices at small angles to the beam direction,

with the absolute calibration obtained from Van der Meer scans. The relative systematic uncertainty on the luminosity measurement was determined to be 1.8% [37] and translates directly into a 1.8% relative uncertainty on the cross-section. It is fully correlated among all E_{T} and η bins of the differential cross sections.

The sources of systematic uncertainty are considered uncorrelated and thus the total systematic uncertainty is calculated by summing in quadrature all the contributions.

Figures **7.5** and **7.6** show the bin-by-bin correction factors for $0 < |\eta(\gamma)| < 1.37$ and $1.52 < |\eta(\gamma)| < 2.37$ together with the factors calculated by varying the selection criteria or the experimental procedure. Fig. **7.7** shows the correction factors for $E_T^{\gamma} > 600$ GeV.

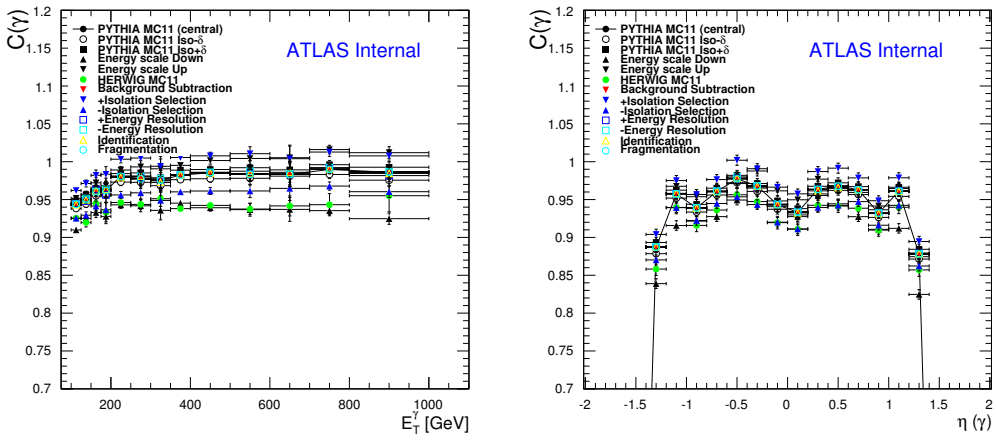

(a) $c(\gamma)$vs E_T^{γ} (b) $c(\gamma)$vs $\eta(\gamma)$, for $|\eta(\gamma)| < 1.37$

Figure 7.5: Bin-by-bin correction factors in $|\eta(\gamma)| < 1.37$, together with systematic uncertainties. Figure (a) is the correction factor as a function of E_T^{γ} for $|\eta(\gamma)| < 1.37$. Figure (b) is a function of $\eta(\gamma)$ for $|\eta(\gamma)| < 1.37$ for an $E_T^{\gamma} > 100$ GeV.

Tables **7.1**, **7.2** and **7.3** show the relative contributions of each systematic variation with respect to the central selection criteria (in percentage to the central

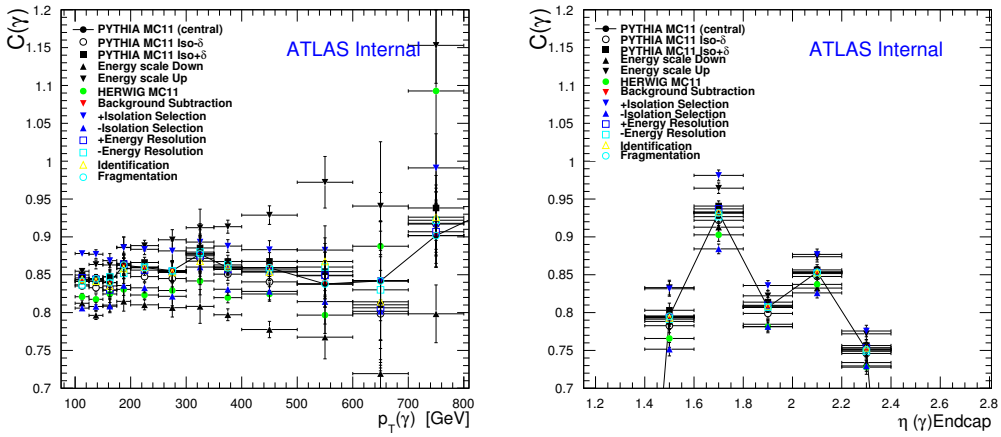

(a) $c(\gamma)$vs E_T^{γ} (b) $c(\gamma)$vs $\eta(\gamma)$ in $1.52 < |\eta(\gamma)| < 2.37$

Figure 7.6: Bin-by-bin correction factors in the endcap ($1.52 < |\eta(\gamma)| < 2.37$) together with systematic uncertainties. Figure (a) is the correction factor as a function of E_T^{γ} for $1.52 < |\eta(\gamma)| < 2.37$. Figure (b) is a function of $\eta(\gamma)$ for $1.52 < |\eta(\gamma)| < 2.37$ for an $E_T^{\gamma} > 100$ GeV.

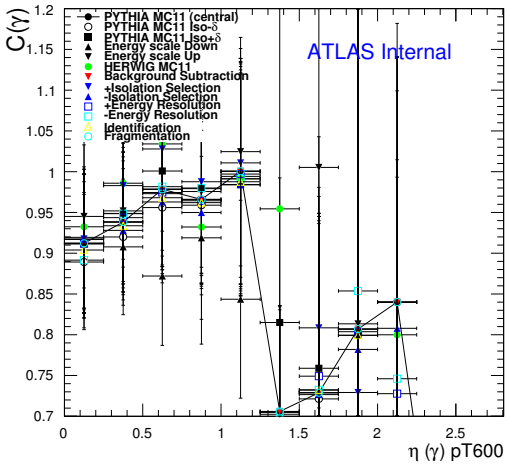

Figure 7.7: Bin-by-bin correction factors for as a function of $|\eta(\gamma)|$ $E_T^{\gamma} > 600$ GeV. The statistical uncertainties in the endcap are too large to reliably calculate the correction factors.

cross sections). The tables show contributions for each phase-space bin i (shown as a separate row) used for the differential cross-section calculations. The columns of the tables are numerated according to the following convention:

- Columns 0,1: Changing the isolating selection by -700 and +700 MeV, respectively, for the reconstructed-level MC;
- Columns 2,3: Scaling the transverse energies (low and upper variation, respectively);
- Column 4: Using HERWIG to evaluate the bin-by-bin correction factors
- Column 5: Using an alternative background subtraction techniques (i.e. the uncorrelated side-band subtraction);
- Column 6: Systematic uncertainties associated to the different isolation selection;
- Columns 7,8: Systematics on the cross section due to the photon resolution;
- Columns 9,10: Systematics for the correction factor with +50% or −50% change to the number of photons from fragmentation respectively
- Columns 11,12: Systematics on the efficiency curves accounting for the differences between the corrected MC efficiencies and the data-driven value (upper and lower variation), see Ref.[34] ;

The result of this thesis was checked against a variation in the description of the z-vertex by the simulation as shown in Fig. **4.1**(a). This was done by reweighting the MC z-vertex distribution to match the data. The effect of such a change was found to be negligible (less than 0.1% contribution on the final cross section).

Range(GeV)	0	1	2	3	4	5	6	7	8	9	10	11	12
100-125	0.73%	-0.59%	3.63%	-0.81%	1.78%	-2.49%	0.06%	2.33%	0.02%	-0.15%	-0.08%	-1.86%	1.97%
125-150	0.73%	-0.68%	2.63%	-0.69%	3.25%	-2.05%	0.04%	2.64%	-0.04%	0.02%	0.18%	-2.16%	2.18%
150-175	0.71%	-0.46%	2.95%	-1.13%	1.54%	-1.88%	-0.08%	2.43%	-0.35%	-0.02%	-0.26%	-2.11%	2.04%
175-200	0.63%	-0.30%	3.62%	-0.64%	2.95%	-1.66%	-0.14%	2.43%	0.37%	0.34%	0.60%	-2.16%	2.69%
200-250	0.84%	-0.38%	3.95%	-0.83%	3.48%	-1.62%	0.16%	-0.43%	0.17%	0.44%	0.08%	-2.21%	2.54%
250-300	0.49%	-0.81%	3.71%	-1.58%	3.38%	-1.54%	-0.38%	-0.68%	-0.35%	0.17%	-0.25%	-2.72%	1.88%
300-350	0.73%	-0.34%	4.20%	-1.48%	2.22%	-1.61%	0.28%	-0.37%	-0.14%	1.23%	0.31%	-1.82%	2.80%
350-400	0.61%	-0.66%	3.87%	-1.28%	4.51%	-1.49%	-0.05%	0.97%	-0.18%	1.10%	-0.02%	-2.30%	2.27%
400-500	0.80%	-0.42%	4.86%	-1.58%	4.27%	-1.82%	0.05%	2.10%	0.06%	1.84%	0.03%	-2.18%	2.47%
500-600	0.49%	-0.87%	4.87%	-2.04%	4.59%	-2.04%	-0.11%	2.78%	-0.24%	2.38%	-0.08%	-2.68%	2.24%
600-700	0.19%	-0.51%	4.87%	-2.08%	3.83%	-2.52%	-0.32%	4.18%	-0.18%	4.01%	-0.04%	-1.99%	1.81%
700-800	0.60%	-0.52%	5.68%	-2.45%	4.52%	-3.69%	-0.05%	-0.34%	0.05%	5.11%	-0.15%	-2.15%	2.20%
800-1000	1.15%	-0.78%	6.44%	-2.53%	2.97%	-2.92%	0.10%	0.38%	-0.04%	6.77%	0.43%	-2.12%	2.56%

Table 7.1: Relative systematic uncertainty on the E_T^γ differential cross section for photons in the barrel. Each column shows a systematic check, while each row shows the bin index. The luminosity uncertainty (1.8%) is not listed in the table, but included into the final cross sections.

As a cross check, the measurement is repeated using an alternative definition of the photon transverse isolation energy, based on three-dimensional topological clusters of energy deposits in the calorimeters, described in more detail in Chapter 5. This affects mostly the photon reconstruction efficiency and isolation efficiencies which are already taken into account. The same calorimeter cells are used for both the calculation of the photon isolation and for the subtraction of the contribution from the underlying event and pileup, thus providing a quantity which is less pileup dependent. A difference smaller than 3% is found between the alternative and the nominal results.

In addition, in order to verify the reliability of the pileup removal technique, differential cross sections were calculated separately for low pileup and high-pileup runs. These two cross sections were found to be consistent, so no systematic uncertainty was assigned.

A possible residual background could arise from electrons that fake photons. High-p_T isolated electrons from W/Z-boson decays tend to be misidentified as converted photons. This is particularly the case when the electron track has either missed the pixel B-layer or no pixel B-layer hit was recorded (the main

Range(GeV)	0	1	2	3	4	5	6	7	8	9	10	11	12
100-125	0.92%	-1.08%	3.43%	-1.91%	2.51%	-3.73%	-0.27%	0.58%	-0.18%	-0.46%	-0.52%	-4.04%	4.25%
125-150	1.57%	-0.03%	5.94%	-2.60%	3.42%	-3.11%	0.41%	1.36%	0.24%	0.25%	0.11%	-3.60%	4.43%
150-175	1.28%	-1.00%	3.53%	-2.62%	1.84%	-2.72%	0.52%	1.29%	0.24%	-0.22%	1.17%	-3.29%	3.73%
175-200	0.57%	-0.26%	5.72%	-2.65%	3.84%	-2.54%	0.57%	1.57%	0.15%	0.48%	-0.15%	-2.56%	3.17%
200-250	1.46%	-0.79%	5.95%	-3.20%	4.23%	-2.37%	-0.04%	-1.14%	0.38%	0.31%	0.39%	-2.66%	3.16%
250-300	1.24%	0.06%	5.92%	-4.50%	2.98%	-2.15%	0.25%	-0.85%	-0.34%	-0.05%	0.13%	-2.94%	4.04%
300-350	0.70%	-0.94%	8.45%	-3.64%	4.11%	-2.26%	1.10%	-1.04%	0.92%	1.59%	0.21%	-1.77%	1.95%
350-400	0.97%	-0.95%	7.60%	-5.85%	4.28%	-2.42%	-0.19%	-1.28%	-0.20%	1.23%	0.26%	-3.19%	3.34%
400-500	2.25%	-0.92%	8.37%	-7.33%	3.88%	-2.28%	0.71%	0.52%	1.22%	2.19%	0.62%	-2.62%	3.73%
500-600	-1.59%	-1.77%	8.78%	-13.82%	4.79%	-2.21%	-3.34%	-1.31%	-2.12%	-0.93%	-1.41%	-4.99%	2.81%
600-700	8.08%	1.34%	13.62%	-8.64%	-13.56%	-17.81%	3.23%	17.69%	3.98%	5.44%	0.96%	-1.50%	2.52%

Table 7.2: Relative systematic uncertainty on the E_T^γ differential cross section for photons in the endcap. Each column shows a systematic check, while each row shows the bin index.

Bin range	0	1	2	3	4	5	6	7	8	9	10	11	12
0.00-0.20	0.65%	-0.64%	0.42%	-1.78%	2.21%	-3.39%	0.02%	2.22%	0.00%	-0.18%	-0.07%	-2.42%	2.40%
0.20-0.40	0.87%	-0.49%	0.56%	-1.64%	2.01%	-2.84%	0.13%	2.28%	-0.04%	-0.09%	0.09%	-2.28%	2.53%
0.40-0.60	0.74%	-0.59%	2.66%	0.48%	2.41%	-2.58%	0.06%	2.00%	-0.04%	-0.12%	0.06%	-2.38%	2.56%
0.60-0.80	0.72%	-0.56%	3.61%	0.20%	2.55%	-2.39%	-0.02%	2.43%	-0.04%	-0.04%	-0.03%	-1.61%	1.65%
0.80-1.00	0.73%	-0.62%	2.07%	-1.25%	2.48%	-2.53%	0.04%	3.16%	0.06%	0.08%	-0.00%	-1.77%	1.76%
1.00-1.20	0.78%	-0.61%	4.87%	-0.67%	2.00%	-2.21%	-0.01%	2.71%	0.07%	0.06%	-0.03%	-1.78%	1.95%
1.20-1.37	1.04%	-0.80%	5.95%	0.19%	2.87%	-2.34%	-0.06%	1.33%	-0.08%	-0.01%	-0.08%	-1.83%	1.85%
1.52-1.80	1.28%	-1.03%	2.65%	-2.82%	2.91%	-3.28%	0.04%	0.35%	0.08%	-0.07%	-0.33%	-4.74%	5.40%
1.80-2.00	1.28%	-0.85%	4.24%	-0.42%	3.65%	-4.34%	-0.08%	0.76%	-0.14%	-0.33%	-0.16%	-3.22%	3.30%
2.00-2.20	0.97%	-0.54%	3.98%	-0.80%	2.11%	-3.22%	0.05%	1.47%	0.02%	-0.25%	0.02%	-2.73%	3.19%
2.20-2.37	0.84%	-0.62%	3.86%	-1.26%	2.80%	-5.09%	-0.14%	1.11%	-0.12%	-0.32%	-0.06%	-3.00%	3.03%

Table 7.3: Relative systematic uncertainty on the $|\eta^\gamma|$ differential cross section. Each column shows a systematic check, while each row shows the bin index.

criteria is used to separate prompt electrons from W/Z-boson decays from electrons originating from converted photons) and is then mistakenly assigned to a converted photon vertex. The corresponding misidentification probability is measured by studying the invariant mass spectrum of $e^{\pm}\gamma$ combination in the Z mass range [38]. This study is described in [25], and found that at high E_{T} the electron misidentification in the full η range is $\approx 0.5\%$. It was found that the fake rate was close to 0.5% even for $E_{\mathrm{T}} > 500$ GeV, indicating a relative independence of the fake rate on E_{T}. In this analysis we neglect the E_{T} dependence and add a constant 0.5% systematic uncertainty to the differential cross sections.

7.5 JETPHOX Uncertainties

For JETPHOX a study was performed to see how the UE, pileup, and hadronization are affected by isolation. This was done to calculate whether this needed to be included in the systematic uncertainties. Isolation is directly sensitive to these effects.

The hadronization was studied by running PYTHIA8 with $E_T^{\gamma} > 100$ GeV using the same cuts as in the paper ($\Delta R = 0.4$, $E_{\mathrm{T}}^{(R<0.4)} < 7$ GeV). In order to see the effect of hadronization, three ratios were calculated: the E_T^{γ} after the parton isolation requirement divided by E_T^{γ} from the truth-level partons after the final and initial state radiation, the E_T^{γ} after isolation using the final state hadrons divided by E_T^{γ} from the truth record, and the E_T^{γ} after the hadron isolation divided by E_T^{γ} using the parton isolation. These ratios can be seen in Figure **7.8**.

The differences are at the level of 2%, and the difference between the hadron and parton isolations is 1% for low-E_T^{γ}. For HERWIG, it is about 3%. Therefore, the correction for JETPHOX is roughly a few %. The statistics in the high-E_T^{γ} region (where the hadronization effects are expected to be negligible) was insufficient to

draw a final conclusion.

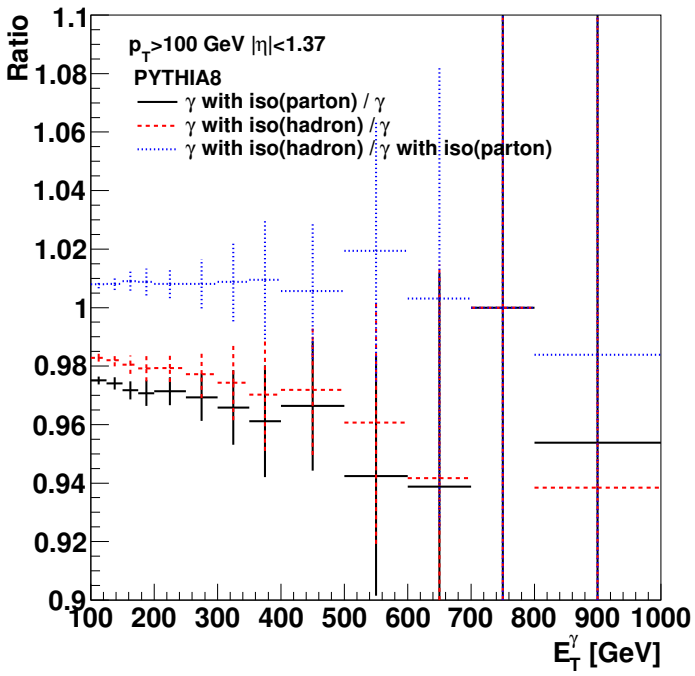

Figure 7.8: A ratio of E_T^γ for various configurations of the isolation with partons and hadrons. This shows that the effect of hadronization is on the order of a few percent at low E_T^γ.

A similar study was performed using the `PYTHIA MC11` and `HERWIG` signal generators (see Chapter 4) which provide a high-statistics sample of events sliced in E_T^γ. The E_T^γ distribution was calculated using a cone of $\Delta R = 0.4$ and $E_{\rm T}^{(R<0.4)} <$ 7 GeV at the parton level with (a) no contributions from pileup and the UE and (b) with the contribution from pileup and the UE. Both (a) and (b) are used to form ratios which are taken into account in the E_T^γ distribution after the standard isolation for the calculations of the efficiencies (i.e. at the particle level and with the jet-area correction applied, see Sect. 7). Figure **7.9** shows these ratios. This figure illustrates that the combined effects from hadronization, extra soft events due to the UE is at the level of $\pm 2\%$.

To understand the contribution from the UE, 10 million `PYTHIA8` events were

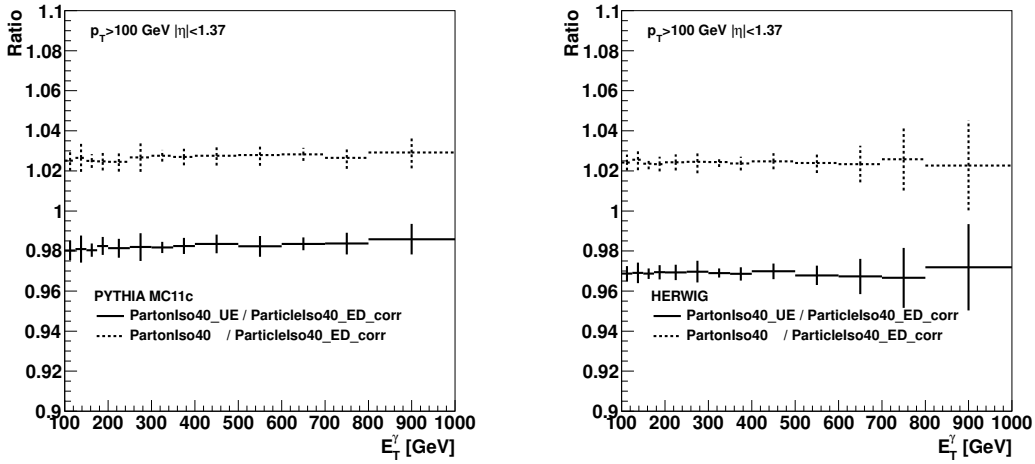

(a) E_T^γ for $|\eta(\gamma)| < 1.37$ in PYTHIA MC11

(b) E_T^γ for $|\eta(\gamma)| < 1.37$ in HERWIG

Figure 7.9: E_T^γ at the parton level with (PartonIso40_UE) and without (PartonIso40) pileup and the UE included, divided by the standard isolation at the particle level used for the efficiency calculations. Where the left plot is PYTHIA MC11 and the right plot is HERWIG DP. The contribution from UE is on the order of less than 2%.

generated using several different UE parameter sets tuned to ATLAS data. The E_T^γ distributions after the isolation requirement $\Delta R = 0.4$ and $E_{\mathrm{T}}^{(R<0.4)} < 7$ GeV use different UE tunes to calculate the ratio with respect to the default PYTHIA8 parameter set. Figure **7.10** shows the UE contribution is $< 2\%$ at the lowest E_T^γ where the statistics were sufficient enough to draw conclusions about the soft nature of the UE so this systematic is not include in the overall systematics.

Thus, the studies presented in this section indicate that effects from soft-QCD, such as hadronization and the UE can be neglected in the comparison with JETPHOX which has a theoretical uncertainty of 15-18%. At this stage, it is arguable to include an additional 1-2% hadronization correction to JETPHOX with the "fragmentation" component, which is suppose to include hadronization soft effects (but not the UE contribution). The inclusion of such small "hadronization" effects will have a small effect on the overall size of the uncertainty (in most cases,

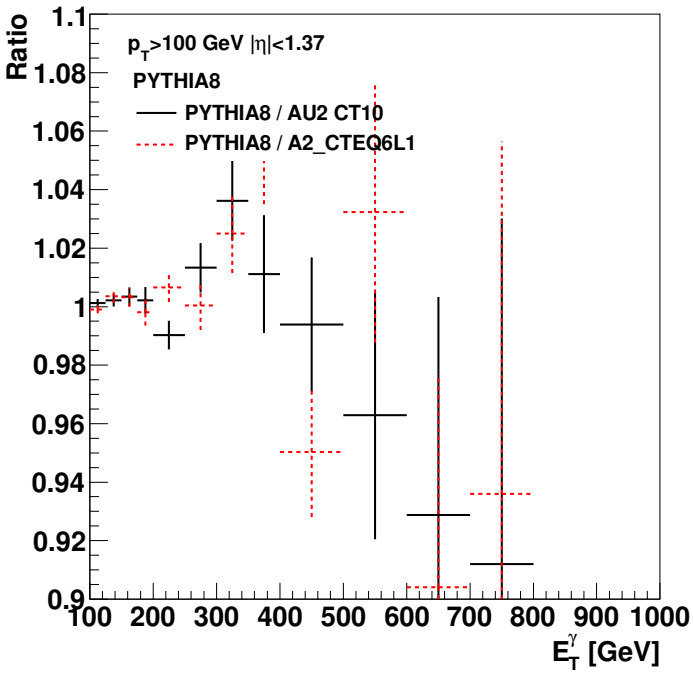

Figure 7.10: The ratio of the E_T^γ using different UE tunes to `PYTHIA8`. The difference is small, on the order of a few percent.

it will be within rounding errors).

The systematic uncertainties on the QCD cross sections are determined in the following way:

- The scale uncertainty has been evaluated by varying the three scales following the constraints:
  - $\mu_R = \mu_F = \mu_f \in [0.5p_{\mathrm{T}}, 2.0p_{\mathrm{T}}]$;
  - $\mu_R \in [0.5p_{\mathrm{T}}, 2.0p_{\mathrm{T}}], \mu_F = \mu_f = p_{\mathrm{T}}$;
  - $\mu_F \in [0.5p_{\mathrm{T}}, 2.0p_{\mathrm{T}}], \mu_R = \mu_f = p_{\mathrm{T}}$;
  - $\mu_f \in [0.5p_{\mathrm{T}}, 2.0p_{\mathrm{T}}], \mu_R = \mu_F = p_{\mathrm{T}}$;

  This leads to a change of the predicted cross section between 15% and 20%.

- The uncertainty on the differential cross section due to insufficient knowledge of the PDFs was obtained by repeating the `JETPHOX` calculation for 52 eigenvector sets of the CT10 PDF and applying a scaling factor in order to obtain the uncertainty for the 68% C.L. interval [39]. The corresponding uncertainty on the cross section increases with E_{T}^{γ} and varies between a few % at $E_{\mathrm{T}}^{\gamma} \simeq 100$ GeV and 15% at $E_{\mathrm{T}}^{\gamma} \simeq 900$ GeV.

- The effect of the uncertainty on the value of the strong coupling constant is evaluated following the recommendation of the CT10 [40] group. This was done using different PDF sets with α_s values varied by ± 0.002 around the central value 0.118. Then a scaling factor was applied in order to obtain the uncertainty for the 68% C.L. interval. A typical uncertainty from such variations is 4.5%, with a small dependence on E_{T}^{γ}.

In the following, the total uncertainty will include the three sources above added in quadrature. The uncertainty due to the scale variation will be shown as

a separate band, since it is the largest among these three uncertainties. Further details on the JETPHOX calculation can be found in Ref. [39].

It should be pointed out that the "fragmentation" contribution in the JETPHOX calculations decreases with the increase of E_T^γ and becomes negligible for $E_T^\gamma >$ 500 GeV. Thus the cross sections at large E_T^γ are almost completely determined by the "direct" process in JETPHOX.

Both MSTW2008NLO and CT10 have similar distributions so it was predicted that the comparison would be similar.

In addition to the NLO calculation, the data were compared to the PYTHIA 6.4 [15] and HERWIG 6.5 [14] MC generators. Both samples are leading-order (LO) parton-shower MC generators, but include a contribution of photons from parton shower and fragmentation. In this analysis PYTHIA utilized the modified leading order MRST2007 [41] PDFs. The event generator parameters were set according to the ATLAS AMBT1 [42] tune. HERWIG 6.5 [14] is based on the cluster fragmentation and the ATLAS AUET1 [43] tune. Full details can be found in Sect. 4.

In order to perform a correct comparison with the JETPHOX calculation, the effects of hadronization, pileup and underlying events have to be understood because the isolation energy is directly sensitive to these effects. The ambient-energy-density correction used for the $E_{\mathrm{T}}^{\mathrm{iso}}$ reconstruction reduces the effects from underlying events and pileup, but this effect may not be completely taken into account. Using PYTHIA and HERWIG with different tunes, the combined effects from hadronization and the underlying events is estimated to be at the level of $\pm 1 - 2\%$. This correction is small compared to the full uncertainty from other sources and is not included in the total theoretical uncertainty.

Chapter 8

Results of the Measurement of the Isolated Cross Section and Comparison with Predictions

The final results are shown in Figure **8.1** for different $|\eta(\gamma)|$ regions. The data are compared to NLO CT10, NLO MSTW2008NLO calculations, as well as with `PYTHIA` and `HERWIG`. The error bars on the data points represent the combination of statistical and systematic uncertainties. The uncertainties are dominated by systematic uncertainties in all regions. The systematic uncertainty on the luminosity measurement (1.8%) is included. The width of the uncertainty bands show the uncertainties in the theoretical predictions due to the choice of the factorization and renormalization scales and the PDF uncertainty. The uncertainties shown are from the CT10 PDF where the MSTW2008NLO PDF uncertainties fall within the CT10 PDF uncertainties. Only the central value of the MSTW2008NLO are shown in the final cross section figures.

The measured E_T^γ-differential cross sections are listed in Tables **8.1**- **8.3**.

The data agree with the NLO CT10 calculations up to the highest $E_T^\gamma \simeq 1$ TeV considered. The data are somewhat higher than the central NLO calculation for low E_T^γ, but agree within the theoretical uncertainty. The central values of the NLO MSTW2008NLO parton density function are above the NLO CT10, and are closer to the data. The agreement is good for both the shape and normalization. `PYTHIA` describes the data well but, `HERWIG` falls short by 10%-20%. `PYTHIA` describes the shape of the E_T^γ cross section better than the `JETPHOX` NLO calculations.

Figure **8.2** shows the differential $\eta(\gamma)$ cross section for $E_T^\gamma > 100$ GeV. The

$\frac{d\eta(\gamma)}{d\sigma}$ cross section is dominated by photons near the low p_T threshold. At this low p_T threshold, PYTHIA has the closest agreement. The data sits above the MC predictions. HERWIG gives the worst prediction for this process.

The NLO prediction for the cross sections, are listed in the Tables **8.4**–**8.6**.

The data were also compared to the MC generators where photons originate from the leading-order γ-jet events which contain only hard-scattering photons (hard subprocesses $qg \rightarrow q\gamma$ and $q\bar{q} \rightarrow g\gamma$), shown in Fig. **8.3**. It can be seen that the MC generators predict lower cross sections than seen in the data by 20% at lower E_T^{γ}. Data includes all the higher-order fragmentation processes which the MC shown in Fig. **8.3** does not. The MC only includes the hard-scattering photons, no fragmentation is included. In Fig. **8.4** it shows a comparison of PYTHIA and HERWIG MC for the hard-scatter photons to the ones that include everything. As the p_T is increased between the LO PYTHIA MC and data, the agreement becomes better. This shows that there is a contribution from the higher order processes such as fragmentation at low p_T. At higher p_T the need for fragmentation is not as great as at lower p_T.

The total inclusive cross section of direct photons calculated in the kinematic region $E_{\mathrm{T}}^{\gamma} > 100$ GeV, barrel η^{γ} region and an isolation of $E_{\mathrm{T}}^{\mathrm{iso}} < 7$ GeV is

$$\sigma(\gamma + X) = 236 \pm 2\ (\mathrm{stat})^{+13}_{-9}(\mathrm{syst}) \pm 4\ (\mathrm{lumi})\ \mathrm{pb}.$$

PYTHIA predicts 224 pb while the cross section HERWIG predicts is 187 pb. The NLO calculations with the CT10 and MSTW2008NLO parton density functions predict 203 ± 28 (theory) pb and 212 ± 27 (theory) pb, respectively, where the theory uncertainty is symmetrised and includes the scale, PDF and α_s uncertainties.

The total cross section for $E_{\mathrm{T}}^{\gamma} > 100$ GeV, end-cap η^{γ} region and an isolation

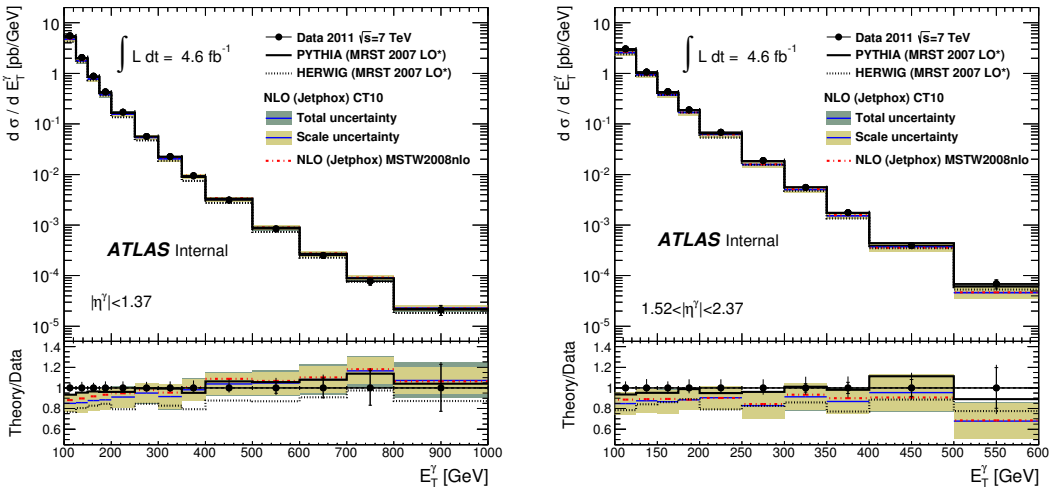

(a) $\frac{d\sigma}{dE_T^\gamma}$ (b) $\frac{d\sigma}{d\eta^\gamma}$

Figure 8.1: Measured vs expected inclusive prompt photon production cross section, for photons with transverse energies above 100 GeV and in the pseudorapidity range $|\eta(\gamma)| < 1.37$ (a) and $1.52 \leq |\eta(\gamma)| < 2.37$ (b). The inner error bars show statistical uncertainties, while the full error bars show statistical and systematic uncertainties added in quadrature. The CT10 and MSTW2008NL PDFs are used in the theoretical computation. The experimental values are placed at the center of each bin. The width of the horizontal bars indicates the size of the bin.

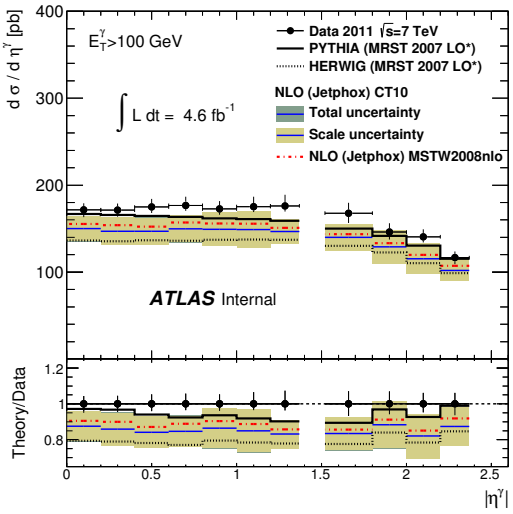

Figure 8.2: Measured vs predicted inclusive prompt photon production cross section as a function of $|\eta(\gamma)|$ for photons with transverse energies above 100 GeV. The inner error bars show statistical uncertainties, while the full error bars show statistical and systematic uncertainties added in quadrature. For this cross section, statistical uncertainties are negligible. The CT10 and MSTW2008NL PDFs are used in the theoretical computation. The experimental values are placed at the center of each energy bin. The width of the horizontal bars indicates the size of the bin.

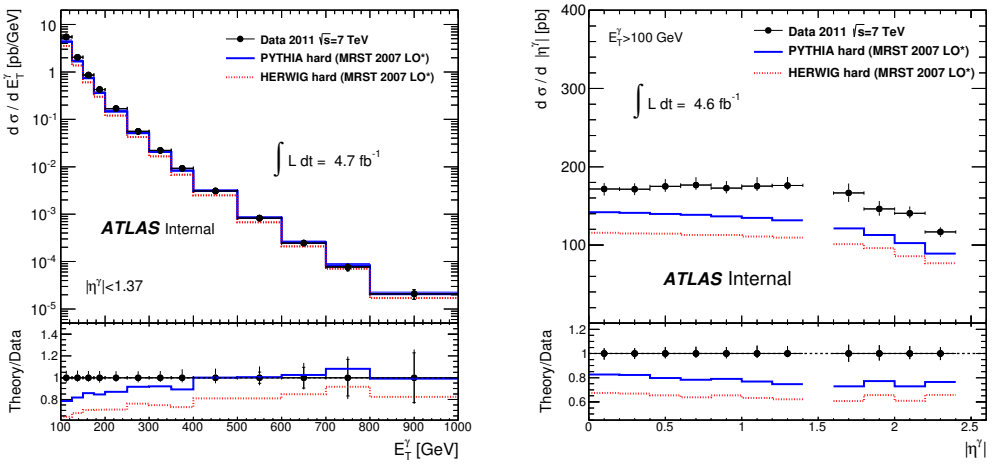

(a) E_T^γ (b) $|\eta(\gamma)|$

Figure 8.3: Same data and NLO as in Fig. **8.1** and **8.2**, but the MC generators were used for direct photons from the hard process.

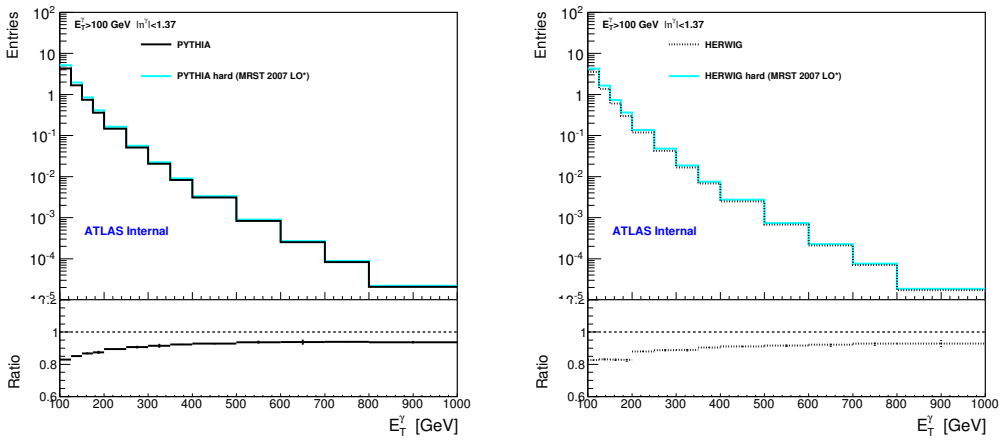

(a) PYTHIA (b) HERWIG

Figure 8.4: Same LO MC as in Fig. **8.1** and **8.2** compared with the MC generators that were used for direct photons from the hard process seen in Fig. **8.3**.

of $E_{\mathrm{T}}^{\mathrm{iso}} < 7$ GeV is

$$\sigma(\gamma + X) = 123 \pm 2\ (\mathrm{stat})^{+9}_{-7}(\mathrm{syst}) \pm 2\ (\mathrm{lumi})\ \mathrm{pb}$$

which can be compared to 118 pb (PYTHIA) and 99 pb (HERWIG). The NLO calculations based on CT10 and MSTW2008NLO predict 105 ± 17 (theory) pb and 109 ± 17 (theory) pb, respectively.

8.0.1 Pileup Comparison

An additional check was performed by re-calculating the cross section using runs before June 30, 2011. These early runs were taken with low instantaneous luminosity, providing a data sample with small pileup. The integrated luminosity for this low-pileup sample is 1.14 fb^{-1}.

Figure **8.5** shows the isolation energies for the low-pileup runs. The shape of the isolation energy agrees with the results from the full data set. Figure **8.6** and Figure **8.7** show the differential cross sections for the low-pileup runs.

E_{T}^{γ} bin [GeV]	$d\sigma^{\gamma}/dE_{\mathrm{T}}^{\gamma}$	$\pm$ (stat.)	$\pm$ (syst.)	[pb/GeV]
$100-125$	5.55	± 0.02	$^{+0.30}_{-0.21}$	
$125-150$	2.06	± 0.01	$^{+0.12}_{-0.07}$	
$150-175$	8.82	± 0.07	$^{+0.44}_{-0.32}$	$\cdot 10^{-01}$
$175-200$	4.28	± 0.05	$^{+0.27}_{-0.14}$	$\cdot 10^{-01}$
$200-250$	1.71	± 0.01	$^{+0.11}_{-0.06}$	$\cdot 10^{-01}$
$250-300$	5.65	± 0.07	$^{+0.32}_{-0.23}$	$\cdot 10^{-02}$
$300-350$	2.25	± 0.04	$^{+0.13}_{-0.08}$	$\cdot 10^{-02}$
$350-400$	9.43	± 0.21	$^{+0.64}_{-0.34}$	$\cdot 10^{-03}$
$400-500$	3.12	± 0.08	$^{+0.24}_{-0.12}$	$\cdot 10^{-03}$
$500-600$	8.44	± 0.44	$^{+0.69}_{-0.38}$	$\cdot 10^{-04}$
$600-700$	2.50	± 0.24	$^{+0.22}_{-0.11}$	$\cdot 10^{-04}$
$700-800$	7.77	± 1.30	$^{+0.73}_{-0.41}$	$\cdot 10^{-05}$
$800-1000$	2.11	± 0.48	$^{+0.22}_{-0.10}$	$\cdot 10^{-05}$

Table 8.1: Measured inclusive prompt photon production cross section in the pseudorapidity range $|\eta^{\gamma}| < 1.37$ as a function of E_{T}^{γ} with statistical and systematic uncertainties. The bin ranges are defined as $[xmin, xmax)$.

The cross sections for the low-pileup runs are:

$$\sigma(\gamma + X) = 232 \pm 3 \text{ (stat)}.$$

The total cross section for $E_{\mathrm{T}}^{\gamma} > 100$ GeV, end-cap η^{γ} region and an isolation of $E_{\mathrm{T}}^{\mathrm{iso}} < 7$ GeV is

$$\sigma(\gamma + X) = 122 \pm 4 \text{ (stat)}.$$

These can be compared to the cross sections for the full data set:

$$\sigma(\gamma + X) = 236 \pm 2 \text{ (stat)}$$

and $\sigma(\gamma + X) = 123 \pm 2$ (stat), and consistent results are found.

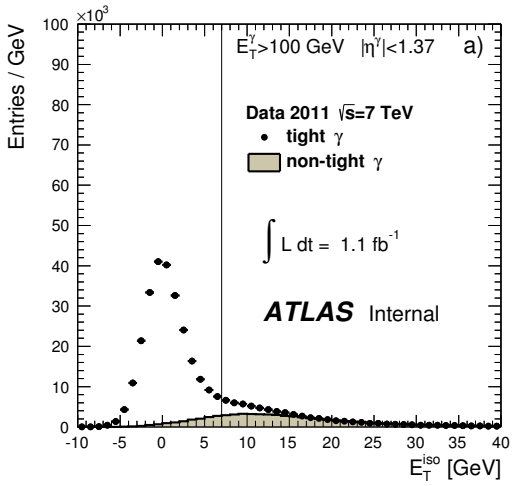

Figure 8.5: $E_{\mathrm{T}}^{(R<0.4)}$ distributions of tight photons after subtracting the normalized non-tight distribution for low-pileup runs before the run 184328.

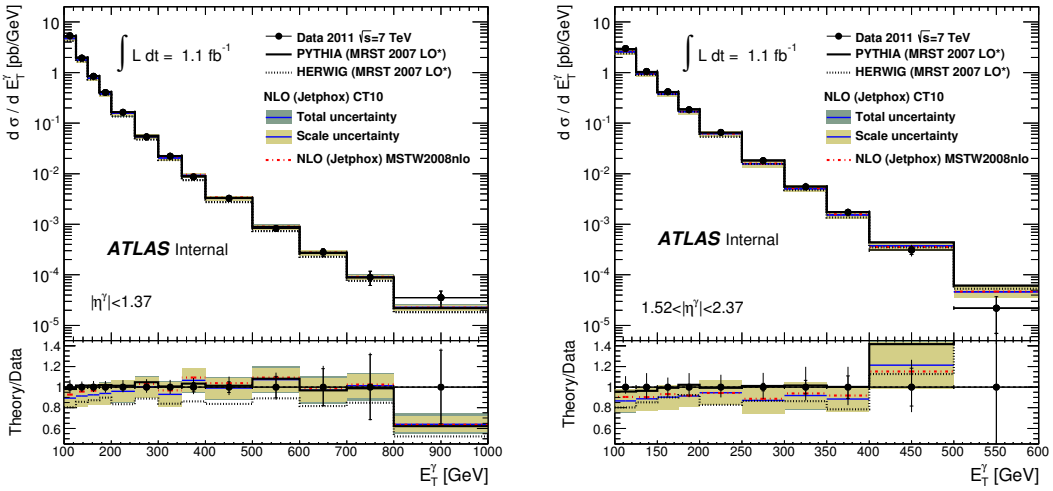

(a) $\frac{d\sigma}{dE_T^\gamma}$ (b) $\frac{d\sigma}{d\eta^\gamma}$

Figure 8.6: Measured vs expected inclusive prompt photon production cross section, for photons with transverse energies above 100 GeV and in the pseudorapidity range $|\eta(\gamma)| < 1.37$ (a) and $1.52 \leq |\eta(\gamma)| < 2.37$ (b) for low pileup runs before the run 184328. The inner error bars show statistical uncertainties, while the full error bars show statistical and systematic uncertainties added in quadrature. The CT10 and MSTW2008NL PDFs are used in the theoretical computation. The experimental values are placed at the center of each bin. The width of the horizontal bars indicates the size of the bin.

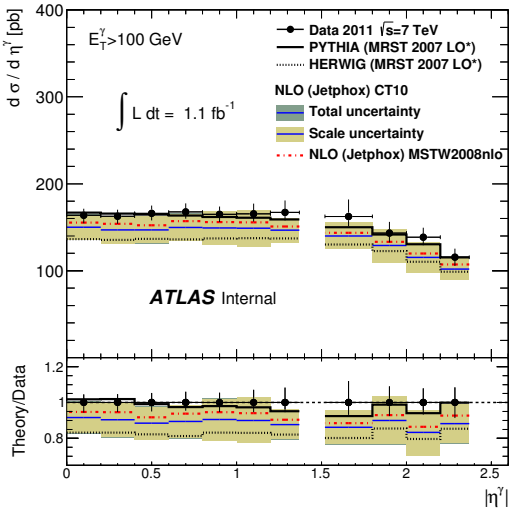

Figure 8.7: Measured vs predicted inclusive prompt photon production cross section as a function of $|\eta(\gamma)|$ for photons with transverse energies above 100 GeV for low pileup runs before the run 184328. The inner error bars show statistical uncertainties, while the full error bars show statistical and systematic uncertainties added in quadrature. For this cross section, statistical uncertainties are negligible. The CT10 and MSTW2008NL PDFs are used in the theoretical computation. The experimental values are placed at the center of each energy bin. The width of the horizontal bars indicates the size of the bin.

E_{T}^{γ} bin [GeV]	$d\sigma^{\gamma}/dE_{\mathrm{T}}^{\gamma}$	$\pm$ (stat.)	$\pm$ (syst.)	[pb/GeV]
$100-125$	3.03	± 0.01	$^{+0.19}_{-0.19}$	
$125-150$	1.06	± 0.01	$^{+0.09}_{-0.06}$	
$150-175$	4.34	± 0.05	$^{+0.27}_{-0.24}$	$\cdot 10^{-01}$
$175-200$	1.90	± 0.03	$^{+0.15}_{-0.09}$	$\cdot 10^{-01}$
$200-250$	6.84	± 0.08	$^{+0.57}_{-0.36}$	$\cdot 10^{-02}$
$250-300$	1.89	± 0.04	$^{+0.15}_{-0.12}$	$\cdot 10^{-02}$
$300-350$	5.52	± 0.22	$^{+0.55}_{-0.29}$	$\cdot 10^{-03}$
$350-400$	1.76	± 0.10	$^{+0.17}_{-0.13}$	$\cdot 10^{-03}$
$400-500$	3.93	± 0.32	$^{+0.49}_{-0.33}$	$\cdot 10^{-04}$
$500-600$	6.83	± 1.35	$^{+0.72}_{-1.10}$	$\cdot 10^{-05}$

Table 8.2: Measured inclusive prompt photon production cross section in the pseudorapidity range $1.52 \leq |\eta^{\gamma}| < 2.37$ as a function of E_{T}^{γ} with statistical and systematic uncertainties. The bin ranges are defined as $[xmin, xmax)$.

8.1 Conclusion

A measurement of the differential cross sections for the inclusive production of isolated prompt photons in pp collisions at a center-of-mass energy of $\sqrt{s} = 7$ TeV is presented using 4.64 fb^{-1} of collision data collected with the ATLAS detector. The E_{T}^{γ} kinematic range of this measurement spans from 100 GeV to 1 TeV, thus significantly extending the measured kinematic range published in the previous ATLAS study [25]. The measured E_{T}^{γ} cross section falls by more than five orders of magnitude in this kinematic range. The data agree with the NLO predictions based on the CT10 and MSTW2008 PDF up to the highest measured $E_{\mathrm{T}}^{\gamma} \simeq 1$ TeV. In this kinematic regime, theoretical uncertainties due to the parton distribution function of the proton become significant. The cross section is also presented as a function of $|\eta^{\gamma}|$, which is dominated by the $E_{\mathrm{T}}^{\gamma} = 100$ GeV region.

Both `PYTHIA` and `HERWIG` describe the shapes of the differential cross sections. The `HERWIG` generator predicts a smaller normalization compared to `PYTHIA`. The MC studies presented in this paper indicate that the direct photon cross section

$\|\eta^\gamma\|$ bin	$d\sigma^\gamma/d\|\eta^\gamma\|$	$\pm$ (stat.)	$\pm$ (syst.)	[pb]
$0.0-0.2$	1.72	± 0.01	$^{+0.08}_{-0.08}$	$\cdot 10^{+02}$
$0.2-0.4$	1.71	± 0.01	$^{+0.08}_{-0.08}$	$\cdot 10^{+02}$
$0.4-0.6$	1.75	± 0.01	$^{+0.09}_{-0.07}$	$\cdot 10^{+02}$
$0.6-0.8$	1.77	± 0.01	$^{+0.10}_{-0.06}$	$\cdot 10^{+02}$
$0.8-1.0$	1.73	± 0.01	$^{+0.09}_{-0.07}$	$\cdot 10^{+02}$
$1.0-1.2$	1.75	± 0.01	$^{+0.11}_{-0.06}$	$\cdot 10^{+02}$
$1.2-1.4$	1.76	± 0.01	$^{+0.13}_{-0.06}$	$\cdot 10^{+02}$
$1.5-1.8$	1.68	± 0.01	$^{+0.12}_{-0.11}$	$\cdot 10^{+02}$
$1.8-2.0$	1.46	± 0.01	$^{+0.10}_{-0.08}$	$\cdot 10^{+02}$
$2.0-2.2$	1.41	± 0.01	$^{+0.09}_{-0.07}$	$\cdot 10^{+02}$
$2.2-2.4$	1.17	± 0.01	$^{+0.07}_{-0.07}$	$\cdot 10^{+02}$

Table 8.3: Measured inclusive prompt photon production cross section for $E_{\mathrm{T}}^{\gamma} > 100$ GeV as a function of $|\eta^\gamma|$ with statistical and systematic uncertainties. The bin ranges are defined as $[xmin, xmax)$.

for the region $E_{\mathrm{T}}^{\gamma} > 500$ GeV is adequately described by the hard sub-processes.

The data agree with the NLO predictions based on the CT10 and MSTW 2008NLO PDFs up to the highest measured energy. In this kinematic regime, the theoretical uncertainties due to the PDFs of the proton become significant. Thus the presented cross sections have the potential to provide additional constraints on the proton PDFs.

At the higher transverse energy regions ($E_T^{\gamma} > 600$ GeV) the available statistics becomes rather limited and the resulting uncertainties are higher. This is expected to be remedied with the new LHC runs during the 2012-2013 data taking.

E_{T}^{γ} bin [GeV]	$d\sigma_{NLO}^{\gamma}/dE_{\mathrm{T}}^{\gamma}$	± Scale Unc.	± Total Unc.	[pb/GeV]
$100-125$	4.72	± 0.48	± 0.58	
$125-150$	1.76	± 0.19	± 0.23	
$150-175$	7.74	± 0.82	± 0.99	$\cdot 10^{-01}$
$175-200$	3.78	± 0.42	± 0.51	$\cdot 10^{-01}$
$200-250$	1.56	± 0.17	± 0.21	$\cdot 10^{-01}$
$250-300$	5.38	± 0.53	± 0.68	$\cdot 10^{-02}$
$300-350$	2.06	± 0.27	± 0.33	$\cdot 10^{-02}$
$350-400$	9.26	± 0.97	± 1.30	$\cdot 10^{-03}$
$400-500$	3.24	± 0.33	± 0.47	$\cdot 10^{-03}$
$500-600$	8.84	± 0.94	± 1.42	$\cdot 10^{-04}$
$600-700$	2.71	± 0.32	± 0.51	$\cdot 10^{-04}$
$700-800$	9.06	± 1.00	± 1.80	$\cdot 10^{-05}$
$800-1000$	2.26	± 0.27	± 0.53	$\cdot 10^{-05}$

Table 8.4: The NLO CT10 inclusive prompt photon production cross section in the pseudorapidity range $|\eta^{\gamma}| < 1.37$ as a function of E_{T}^{γ} with statistical and systematic uncertainties. Small differences in the upper and lower uncertainties were symmeterized. The bin ranges are defined as $[xmin, xmax)$.

E_{T}^{γ} bin [GeV]	$d\sigma_{NLO}^{\gamma}/dE_{\mathrm{T}}^{\gamma}$	± Scale Unc.	± Total Unc.	[pb/GeV]
$100-125$	2.57	±0.33	±0.38	
$125-150$	9.30	±1.19	±1.35	$\cdot 10^{-01}$
$150-175$	3.75	±0.50	±0.56	$\cdot 10^{-01}$
$175-200$	1.68	±0.19	±0.22	$\cdot 10^{-01}$
$200-250$	6.18	±0.77	±0.88	$\cdot 10^{-02}$
$250-300$	1.57	±0.24	±0.27	$\cdot 10^{-02}$
$300-350$	5.04	±0.71	±0.86	$\cdot 10^{-03}$
$350-400$	1.53	±0.21	±0.27	$\cdot 10^{-03}$
$400-500$	3.75	±0.69	±0.88	$\cdot 10^{-04}$
$500-600$	4.63	±1.17	±1.50	$\cdot 10^{-05}$
$600-700$	8.63	±1.54	±2.58	$\cdot 10^{-06}$
$700-800$	1.49	±0.50	±0.74	$\cdot 10^{-06}$
$800-1000$	8.03	±2.20	±4.53	$\cdot 10^{-08}$

Table 8.5: The NLO CT10 inclusive prompt photon production cross section in the pseudorapidity range $1.52 \leq |\eta^{\gamma}| < 2.37$ as a function of E_{T}^{γ} with statistical and systematic uncertainties. Small differences in the upper and lower uncertainties were symmetrized.

$\lvert\eta^{\gamma}\rvert$ bin	$d\sigma_{NLO}^{\gamma}/d\lvert\eta^{\gamma}\rvert$	± Scale Unc.	± Total Unc.	[pb]
$0.0-0.2$	1.50	±0.14	±0.15	$\cdot 10^{+02}$
$0.2-0.4$	1.47	±0.16	±0.16	$\cdot 10^{+02}$
$0.4-0.6$	1.47	±0.15	±0.16	$\cdot 10^{+02}$
$0.6-0.8$	1.50	±0.15	±0.16	$\cdot 10^{+02}$
$0.8-1.0$	1.49	±0.19	±0.19	$\cdot 10^{+02}$
$1.0-1.2$	1.49	±0.21	±0.21	$\cdot 10^{+02}$
$1.2-1.37$	1.47	±0.14	±0.14	$\cdot 10^{+02}$
$1.52-1.8$	1.40	±0.15	±0.15	$\cdot 10^{+02}$
$1.8-2.0$	1.29	±0.19	±0.19	$\cdot 10^{+02}$
$2.0-2.2$	1.15	±0.17	±0.18	$\cdot 10^{+02}$
$2.2-2.37$	1.02	±0.13	±0.13	$\cdot 10^{+02}$

Table 8.6: The NLO CT10 inclusive prompt photon production cross section for $E_{\mathrm{T}}^{\gamma} > 100$ GeV as a function of $|\eta^{\gamma}|$ with statistical and systematic uncertainties. Small differences in the upper and lower uncertainties were symmetrized.

References

[1] T. Chech L.L. Jenkovsky and I. Karpenko. Nuclear science and safety in europe nato security through science series: Physics and biophysics. *Springer*, 2006.

[2] F Monticelli, J M Lorenz, A Tricoli, and Kohno T. Performance of the electron and photon trigger in p-p collisions at $\sqrt{s}$=7 tev with the atlas detector at the lhc in 2011. *ATL-DAQ-INT-2012-001*, 2011.

[3] Georges Aad et al. Electron reconstruction and identification efficiency measurements with the ATLAS detector using the 2011 LHC proton-proton collision data. *Eur.Phys.J.*, C74:2941, 2014.

[4] Olivier Davignon. Recherche du boson de higgs du modle standard produit par fusion de bosons vecteurs et se dsintgrant en deux photons dans lexprience atlas auprs du lhc. *ATLAS Dissertation*, 2013.

[5] S. Catani et al. Cross section of isolated prompt photons in hadron-hadron collisions. *JHEP*, 05:028, 2002.

[6] P. Aurenche et al. Recent critical study of photon production in hadronic collisions. *Phys. Rev. D*, 73:094007, 2006.

[7] P. Aurenche, R. Baier, M. Fontannaz, and D. Schiff. Prompt photon production at large p_t. scheme invariant qcd predictions and comparison with experiment. *Nucl. Phys. B*, 297:661, 1988.

[8] P. Aurenche, R. Baier, M. Fontannaz, J. F. Owens, and M. Werlen. Quantitative constraints on the gluon distribution function in the proton from collider isolated-photon data. 2012.

[9] David d'Enterria and Juan Rojo. Quantitative constraints on the gluon distribution function in the proton from collider isolated-photon data. *Nucl.Phys.*, B 860:311–338, 2012.

[10] Vladislav Balagura. Notes on van der Meer Scan for Absolute Luminosity Measurement. *Nucl.Instrum.Meth.*, A654:634–638, 2011.

[11] G. Aad et al. The atlas experiment at the cern large hadron collider. *JINST*, 3:S08003, 2008.

[12] Electron and photon reconstruction and identification in atlas: expected performance at high energy and results at 900 gev. *ATLAS-CONF-2010-005*, 2010.

[13] Georges Aad et al. Improved luminosity determination in pp collisions at sqrt(s) = 7 TeV using the ATLAS detector at the LHC. 2013.

[14] G. Corcella et al. `Herwig` 6.5. *JHEP*, 01:010, 2001.

[15] Torbjorn Sjöstrand, Stephen Mrenna, and Peter Z. Skands. PYTHIA 6.4 Physics and Manual. *JHEP*, 05:026, 2006.

[16] Patrick Aurenche, Michel Fontannaz, Jean-Philippe Guillet, Eric Pilon, and Monique Werlen. A New critical study of photon production in hadronic collisions. *Phys. Rev.*, D73:094007, 2006.

[17] S. Agostinelli et al. `GEANT4` - a simulation toolkit. *Nucl. Instrum. Methods A*, 506:250, 2003.

[18] B. R. Webber Ellis R. K., W. J. Stirling. *QCD and Collider Physics*. Cambridge University Press, 1996.

[19] G. Aad et al. New atlas event generator tunes to 2010 data. *ATL-PHYS-PUB-2011-008*, 2011.

[20] H Abreu, B Brelier, V Dao, M Delmastro, M Fanti, J Hartert, G Marchiori, T Koffas, JF Marchand, F Martin, V Perez Reale, K Tackmann, N Trinh, H Wang, M Wielers, SL Wu, and L Yuan. Photon performance in the atlas experiment. Technical Report ATL-COM-PHYS-2010-240, CERN, Geneva, May 2010.

[21] Calibrated $z \to ee$ invariant mass. *ATL-COM-PHYS-2010-734*, 2010.

[22] Measurements of the photon identification efficiency with the atlas detector using 4.9 fb$^-$1 of pp collision data collected in 2011. 2012.

[23] Data-quality requirements and event cleaning for jets and missing transverse energy reconstruction with the atlas detector in proton-proton collisions at a center-of-mass energy of $\sqrt{s} = 7$ tev. Technical Report ATLAS-CONF-2010-038, CERN, Geneva, June 2010.

[24] Purity estimates for the inclusive isolated photons. *ATL-PHYS-INT-2011-015*, 2011.

[25] Georges Aad et al. Measurement of the inclusive isolated prompt photon cross- section in pp collisions at sqrt(s)= 7 TeV using 35 pb-1 of ATLAS data. *Phys. Lett. B*, 706:150–167, 2011.

[26] Matteo Cacciari, Gavin P. Salam, and Gregory Soyez. The catchment area of jets. *JHEP*, 04:042, 2008.

[27] Matteo Cacciari, Gavin P. Salam, and Sebastian Sapeta. On the characterisation of the underlying event. *JHEP*, 04:065, 2010.

[28] ATLAS Collaboration. Measurement of the inclusive isolated prompt photon cross section in pp collisions at $\sqrt{s} = 7$ TeV with the ATLAS detector. *Phys. Rev.*, D 83:052005, 2011.

[29] ATLAS Collaboration. Search for the standard model higgs boson in the diphoton decay channel with 4.9 fb^{-1} of pp collision data at $\sqrt{s} = 7$ TeV with atlas. *Phys. Rev. Lett.*, 108:111803, Mar 2012.

[30] Georges Aad et al. Measurement of isolated-photon pair production in pp collisions at $\sqrt{s} = 7$ TeV with the ATLAS detector. *JHEP*, 1301:086, 2013.

[31] CMS Collaboration. Measurement of the Differential Cross Section for Isolated Prompt Photon Production in pp Collisions at 7 TeV. *Phys. Rev. D*, 84:052011, 2011.

[32] V. M. Abazov et al. Measurement of the isolated cross section in $p\bar{p}$ collisions at $\sqrt{s} = 1.96$ tev. *Phys. Lett. B*, 639:151, 2006.

[33] T. Aaltonen et al. Measurement of the inclusive isolated prompt photon cross section in $p\bar{p}$ collisions at $\sqrt{s} = 1.96$ tev using the cdf detector. *Phys. Rev. D*, 80:111106(R), 2009.

[34] ATLAS Collaboration. Measurements of the photon identification efficiency with the ATLAS detector using 4.9 fb^{-1} of pp collision data collected in 2011. *ATLAS-CONF-2012-123*, 2012.

[35] Georges Aad et al. In-situ jet energy scale and jet shape corrections for multiple interactions in the first ATLAS data at the LHC. (ATLAS-CONF-2011-030), March 2011.

[36] Atlas egamma recommendation for 2011 analysis. available from the web page: https://twiki.cern.ch/twiki/bin/viewauth/AtlasProtected/PhotonID2011.

[37] Updated luminosity determination in pp collisions at $\sqrt{s} = 7$ TeV using the atlas detector. *ATLAS-CONF-2011-011*, 2011.

[38] Measurement of electron background to prompt photon sample on $35.8\,\text{pb}^{-1}$ collision data using the atlas detector. 2011.

[39] B. Blair et al. Nlo theoretical predictions for photon measurements using the phox generators. Technical report, 2011.

[40] Hung-Liang Lai, Marco Guzzi, Joey Huston, Zhao Li, Pavel M. Nadolsky, et al. New parton distributions for collider physics. *Phys.Rev.*, D82:074024, 2010.

[41] A. Sherstnev and R. S. Thorne. Parton distributions for lo generators. *Eur. Phys. J.*, C55:553, 2008.

[42] G. Aad et al. Charged-particle multiplicities in pp interactions measured with the atlas detector at the lhc. 2010. Submitted to New J. Phys.

[43] First tuning of herwig/jimmy to atlas data. *ATL-PHYS-PUB-2010-014*, 2010.